DISCLAIMER:

This document does not meet the
current format guidelines of
the Graduate School at
The University of Texas at Austin.

It has been published for
informational use only.

The Thesis Committee for Saurabh Tandon

Certifies that this is the approved version of the following thesis:

Identification of Productive Zones in Unconventional Reservoirs

APPROVED BY
SUPERVISING COMMITTEE:

Supervisor:

Mark McClure

Carlos Torres-Verdin

Identification of productive zones in unconventional reservoirs

by

Saurabh Tandon, B. Tech.

Thesis

Presented to the Faculty of the Graduate School of
The University of Texas at Austin
in Partial Fulfillment
of the Requirements
for the Degree of

Master of Science in Engineering

The University of Texas at Austin
August 2015

Dedication

I dedicate this thesis to my family and friends.

Acknowledgements

I would like to thank Dr. Mark McClure for his all his help and guidance during the course of my project. I also thank Dr. Carlos Torres-Verdin and for his valuable insights and for accepting to by my second reader. I would like to thank Dr. Hugh Daigle and for sharing his insight about our research.

I thank my fellow students of my research group for their support and their technical expertise. My thanks also go to all the faculty of the Petroleum and Geosystems Engineering, The University of Texas at Austin for their guidance and assistance. I am also grateful to Frankie Hart for all her help. I thank my family for their love and support. The work reported in this paper was funded by The University of Texas at Austin's Research Consortium on Formation Evaluation, jointly sponsored by Afren, Anadarko, Apache, Aramco, Baker-Hughes, BG, BHP Billiton, BP, Chevron, ConocoPhillips, COSL, ENI, ExxonMobil, Halliburton, Hess, Maersk, Mexican Institute for Petroleum, ONGC, OXY, Petrobras, PTT Exploration and Production, Repsol, RWE, Schlumberger, Shell, Statoil, TOTAL, Weatherford, Wintershall, Woodside Petroleum Limited

Abstract

IDENTIFICATION OF PRODUCTIVE ZONES IN UNCONVENTIONAL RESERVOIRS

Saurabh Tandon, M.S.E

The University of Texas at Austin, 2015

Supervisor: Mark McClure

Large-scale multi-stage fracture treatments in long horizontal wells have enabled economic hydrocarbon production from source mudrocks. A productive zone in mudrocks is defined as a region with high production or high productive potential. Rock fracability is an important parameter used in evaluating the productive potential in a source mudrocks. The fracability of the rock is the degree to which hydraulic fracturing can create a dense and conductive fracture network upon fracturing in the formation. However, there is no agreement on the formation geomechanical properties that result in a source rock having good fracability. The objective of this thesis to identify formation properties that may be related to fracability and to identify how these properties may be assessed from well logs. Once the properties have been identified, data from 15 wells in the Barnett shale are used to assess the effect of the properties on long-term production.

We performed a sensitivity study on the effect of formation properties on the size of the stimulated rock volume. Field-scale simulations of a single fracturing stage were performed with CFRAC (Complex Fracturing ReseArch Code), a fracture simulator that couples fluid flow and stresses induced by fracture deformation (sliding and opening) in large, discrete fracture networks.

Two-hundred simulations were performed with a uniform space filling design: a low discrepancy quasi-random sequence uniformly filling the hyper-parameter space. Each simulation used a different stochastically generated natural fracture network even though each was statistically similar in terms of fracture orientation, density, and length.

Simulation results were post-processed to estimate a measure of the stimulated reservoir volume in each simulation. Parameters affecting tendency for shear stimulation fracture conductivity had the biggest effect on the stimulated reservoir volume. Unfortunately, these parameters are not easy to estimate in-situ.

A review of the literature was carried out to understand the relationship between unpropped fracture conductivity (which cannot easily be measured in-situ) and other formation properties that could be quantified with available techniques. We used the concept of shear dilation angle to describe increase in conductivity in response to sliding. The dilation angle can be correlated to the joint compressive strength of the rock which is equal to the unconfined compressive strength for an unaltered rock. Unconfined compressive strength can be estimated from sonic logs.

This hypothesis was tested on 15 wells in the Barnett Shale. Hydrocarbon-bearing zones were identified in the wells using the gamma ray log and the cumulative

mechanical properties of the zones were compared to the long-term production of the wells. Results show that including the unconfined compressive strength in finding productive zones will improve the effectiveness of prediction models. Such a behavior alludes to the possibility that properties affecting unpropped fracture conductivity should be given consideration while planning and implementing fracture treatments in unconventional plays.

Table of Contents

List of Tables

List of Figures

Chapter 1: Productive Zone Analysis

1.1 INTRODUCTION

Production of oil and gas from shale has revolutionized the oil and gas sector of the US. In the US, the production shale plays has accounted most of oil and gas production growth (Sieminski, 2014). The EIA estimates that, worldwide, there are 35782 Tcf of gas with 7795 Tcf technically recoverable and 6753 billion barrels of oil with 335 billion technically recoverable (EIA/ARI, 2014). Horizontal drilling and large scale multi-stage fracturing enable economic production of hydrocarbons from these tight formations (King, 2012).

There are many ways of defining productive zones in unconventional formations in the literature. At the basin scale, productive zones refer to regions that have high production or potential for high production (McGlade et al., 2012). At the wellbore scale, productive zones are used to describe zones that are suitable for hydraulic fracturing (Hashmy et al., 2012). Shale formations show heterogeneous properties at small and at large scale (Pilcher et al., 2012). Understanding what geological properties makes rock more conducive to effective fracturing is a critical step in identifying the economic potential of a shale resource.

1.2 BACKGROUND WORK

Productive zones in unconventional plays have been found to depend on geomechanical and petro-physical rock properties such as thickness, thermal maturity,

lithology, porosity, presence of natural fractures, rock fracability, and kerogen content (Liu, 2013; Hashmy et al., 2012; Giles and Tennant, 2014, Gale et al., 2007). A lot of work has been carried out in trying to understand how each of these properties affects the production in unconventional formation.

The total hydrocarbon in a formation depends on its thickness (EIA/ARI, 2014). The thickness of the formation can be estimated from seismic data and can be confirmed with log data (Ellis and Singer, 2007). Measurements from well logs can be used to identify boundaries of zones, and total height can be evaluated (Ellis and Singer, 2007).

Shale formations may act both as the reservoir and the seal for hydrocarbons (EIA/ARI, 2014). Total organic content or kerogen content is important for determining its hydrocarbon generating potential. Determination of organic content of rock can be carried out using gamma ray and spectral gamma ray logs (Ellis and Singer, 2007). These logs measure the concentration of naturally occurring radioactive elements, which can be correlated to total organic content (Ellis and Singer, 2007). Passey et al. (1990) proposed the Δlog R method that uses sonic porosity and resistivity logs to estimate organic content of rocks. Core studies are needed to calibrate this data and determine the type of organic in shale (Kinley et al., 2008).

Vitrinite reflectance studies ascertain thermal maturity of kerogen (Kinley et al., 2008). They help in determining what type of hydrocarbon (gas or oil) that will be produced by the rock (Kinley et al., 2008). The presence of kerogen also affects mechanical properties of rocks as well as measurements from other logs (Kinley et al.,

2008). The effect of kerogen on these properties also needs to be understood to determine shale productivity.

Rock porosity can be determined from logs but corrections are needed for clay content and kerogen present in rocks (Ellis and Singer, 2007). It is difficult to measure the effective porosity in unconventional formations (Kale et al., 2010). Dual porosity and triple porosity models have been used for determining the effective rock porosity because of presence of gas in fractures and micropores present in unconventional formations (Alahamadi, 2010).

There are many methods of assessing a productive formation in the unconventional plays and combining it with overall reservoir characterization. The EIA (Energy Information Association) used the following properties to perform reservoir characterization in shale (EIA/ ARI, 2014):

- TOC content in the rock (>2%)
- Formation Depth
- Thermal maturity
- Shale lithology (content of quartz in the formation)
- Other factors

According to EIA/ ARI (2014), this methodology provides conservative estimates of variables for productivity assessment of shale. The assessed volume is then multiplied by a recovery factor to get estimated ultimate recovery (EUR) of hydrocarbon. In the EIA methodology, rock fracability is related only to the content of quartz in the formation.

Rock fracability is defined as the ability of rock to create a dense, well-connected network of fractures conducive to fluid flow (Cipolla et al., 2008). Fracability of rock can be correlated to its brittleness (Yang et al., 2013). There are different definitions of brittleness, but it usually defines a rock property that enhances its ability to fracture (Yang et al., 2013; Jin et al., 2014). Rock brittleness is usually correlated to elastic properties and other geomechanical properties of the rock such as Young's modulus, Poison's ratio, coefficient of friction (Yang et al., 2013). This has resulted in many different correlations for describing rock brittleness. For instance, Hucka and Das (2008) correlated brittleness to compressive, tensile strength and coefficient of friction of the rock while Rickman et al. (2008) correlated brittleness to rock elastic properties.

Rock properties measured from logs and seismic data can be used for estimating brittleness indices. Seismic data inversion techniques can give layer properties from seismic data (Pendrel et al., 2000). Layer properties can be correlated to rock elastic properties that can be used for calculating brittleness indices (Yang et al., 2013). Jarvie et al. (2007) define rock fracability as the fraction of quartz present in shale which is derived from the observation that regions in the Barnett with high quartz content are more productive. This definition is expanded in the work of Hashmy et al. (2012) to include the fraction of all minerals other than clays. A summary of brittleness correlations is presented in Yang et al. (2013). Yang et al. (2013) compares the relative performance of these correlations. It can be observed from works of Yang et al. (2013) that there is very little consensus on what correlation works best for defining brittleness of rocks. Lack of understanding of rock brittleness makes determination of rock fracability difficult.

The role of natural fractures in fracturing and during production in unconventional plays also needs to be understood. Natural fractures play an important role in determining the effectiveness of fracture treatment and the overall productivity in unconventional formations (Gale et al., 2007). Hydraulic fractures can interact with geologic features in the formation to produce a complex network of fractures (Cipolla et al., 2008). Injection of fluid might also cause slip and dilation of natural fractures that might increase their conductivity (Barton and Choubey, 1977; Zhang et al., 2012).

1.3 OBJECTIVES

The objective of this thesis is to identify geomechanical properties that influence fracture treatments in unconventional reservoirs. A sensitivity analysis was conducted using a design of experiments approach to determine the effect of each parameter on the productivity of fracture treatment.

The second objective of this thesis is to develop hypotheses about how formation properties related to productivity can be estimated from measurements taken in the field. The final objective of this thesis is to test our hypotheses using field data from a shale reservoir.

1.4 OUTLINE OF THE THESIS

Chapter 2 describes the sensitivity study that was conducted to understand the effect of geomechanical parameters on fracture treatments using a complex fracture simulator. The sensitivity study in Chapter 2 reveals that properties related to shear stimulation of natural fractures and unpropped fracture conductivity play a critical role in

defining the success of a fracture treatment in unconventional reservoirs. It is hypothesized that wells that have a greater tendency for shear stimulation will be more conducive to fracturing and will be more productive in the long term.

Chapter 3 discusses hydromechanical coupling behavior in rocks and how the results of Chapter 2 can be applied to well log analysis for productive zone prediction. Chapter 3 then describes a field study conducted in Barnett Shale to corroborate the hypothesis developed in Chapter 2. Appendix A and Appendix B provides details of formation properties varied in all the simulations. Appendix C presents the *SRV* values obtained by post processing the results of CFRAC. Appendix D gives trends of production data observed in the wells in the Barnett Shale. Appendix E presents logs for the wells used in the study.

Chapter 2: Sensitivity Study

This chapter explains the sensitivity study that was performed to understand the effect that mechanical properties of rocks have on fracturing. Design parameters such as fluid injection rate, and fluid viscosity were kept constant to isolate the effects of geological properties. The geomechanical properties chosen for the study (described below) are shear modulus, Poisson's ratio, anisotropy in principal stresses, hydraulic aperture shear dilation angle, fracture toughness, reference fracture hydraulic aperture, the hydraulic aperture 90% closure stress, and coefficient of friction. The size of the stimulated reservoir volume was used to quantify the effective of the fracture treatment. The results were analyzed using scatter plots, multivariate linear regression, variance based sensitivity analysis, and a statistical goodness-of-fit test for estimating how the variables affect the extreme values of the results. The results of the study of the study suggest that factors related to generating and maintaining unpropped fracture conductivity play a critical role in success of fracture treatment in unconventional reservoirs.

2.1 INTRODUCTION

Evidence of fracture network complexity can be seen in results from mine-back experiments and from microseismic observations (Cipolla et al., 2008; Warpinski and Teufel, 1987). Figure 2.1 shows a fracture mine-back (taken from Cipolla et al., 2008), and Figure 2.2 shows the microseismic observations in a field study that demonstrate complexity in the fracturing treatment (taken from Cipolla et al., 2011).

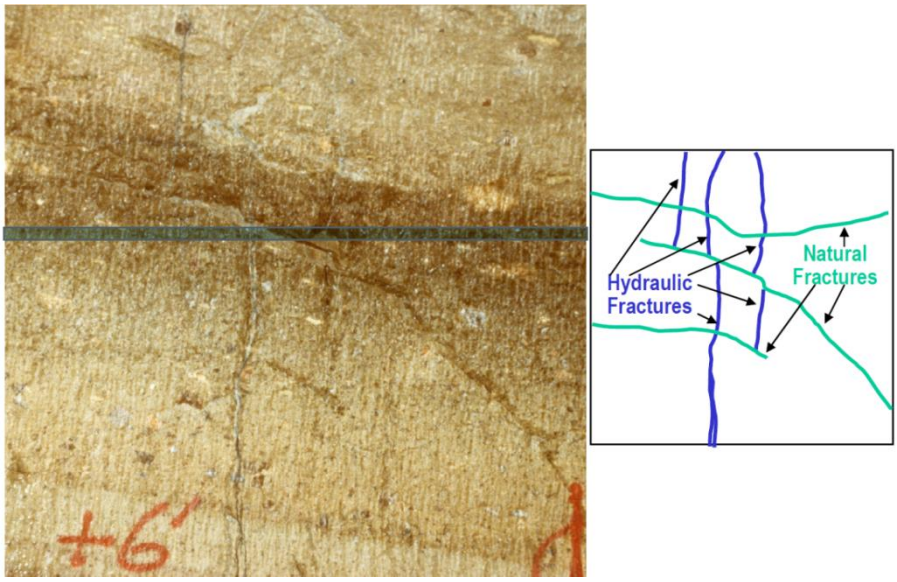

Figure 2.1: Section of the mine-back experiment with hydraulic fracture interacting with natural fractures (taken from Cipolla et al., 2008).

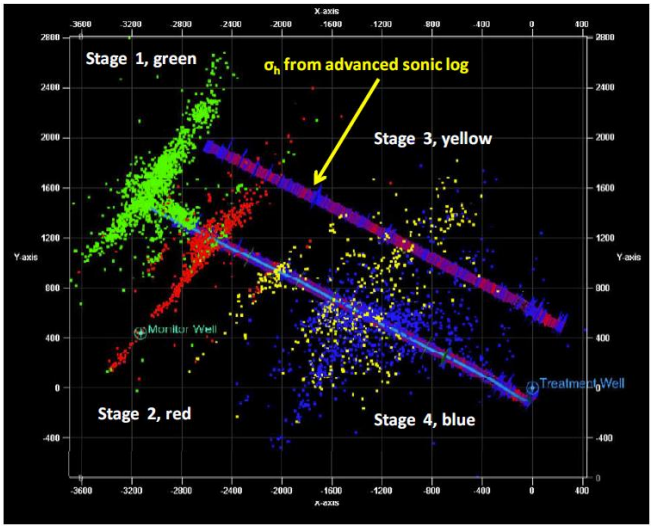

Figure 2.2: Microseismic cloud burst from field treatment carried out in Barnett Shale (taken from Cipolla et al., 2011).

It is suspected that complexity in fracture networks is generated by the interaction of hydraulic fractures with already existing natural fractures, bedding planes, and other geologic features (Cipolla et al., 2008; Warpinski and Teufel, 1987).

2.1.1 DESIGN OF EXPERIMENTS

Design of experiments is the area of applied statistics that deals with conducting tests. In our study, our goal was to identify the first order effect and the interaction effects that each parameter have on fracturing. The total effects index, a combination of first order effect of the variable and the interaction of effect of the variable with other variables is computed in our study (Saltelli et al., 2008, p. 199).

The algorithm of Saltelli et al. (2008) was implemented to find the total effects index for each variable. The algorithm involves using a design of experiments approach to initialize variable settings and then use sequential replacement to find the total effects index. The implementation of this algorithm is explained in section 2.2.3. Sobol sequence design is used for initializing the inputs for Saltelli et al. (2008) algorithm for calculation of total effects index because Sobol sequences completely outperform other random sampling in the estimation of multi-dimensional space (Sobol, 1967, Saltelli et al., 2008).

2.2 METHODOLOGY

2.2.1 CFRAC SIMULATOR

The sensitivity study was carried out using the CFRAC simulator. CFRAC stands for Complex Fracture ReseArch Code (McClure, 2012). The simulator solves the following equations:

(1) The unsteady state mass balance for an isothermal incompressible fluid

$$\frac{\partial(\rho E)}{\partial t} = -\nabla \cdot (q_f\, e) + s, \tag{2.1}$$

where t is time, s is the source, E is void aperture, ρ is fluid density, q_f is mass flux, and e is the hydraulic aperture. Darcy flow is assumed for calculating mass flux in fractures,

$$q_f = -\frac{k\rho}{\mu_l}\frac{\partial P}{\partial x}, \tag{2.2}$$

where k is fracture permeability, $\partial P / \partial x$ pressure gradient in x direction of flow and μ_l is viscosity of the fluid.

(2) Boundary condition for normal stress (Jaeger et al., 2007):

$$\nabla^T \boldsymbol{T_s} = 0, \tag{2.3}$$

where $\boldsymbol{T_s}$ is the stress tensor. Hooke's law is used for calculating the change in stresses

$$\boldsymbol{T_s} = \frac{2G\nu}{1-\nu} trace(\varepsilon) I + 2G\varepsilon\ , \tag{2.4}$$

where G is the shear modulus and ν is Poisson' s ratio, $\boldsymbol{\varepsilon}$ is the strain tensor and I is the identity matrix. The formation is assumed to be homogeneous, isotropic and linearly elastic.

(3) Coulomb's equations is used for modeling shear on fractures

$$\tau = \sigma'_n \mu + S_0, \tag{2.5}$$

where τ is the shear stress, μ is the coefficient of friction, S_0 is cohesion of the fractures, and σ'_n is the effective normal stress.

$$\sigma'_n = \sigma_n - P, \tag{2.6}$$

where σ_n is the normal stress. Fracture transmissivity is approximated using the cubic law:

$$T = \frac{e^3}{12}, \tag{2.7}$$

where T is fracture transmissivity. The propagation of hydraulic fractures is modelled with liner elastic fracture mechanics. A fracture is assumed to propagate when its stress intensity factor, K_I, reaches its fracture toughness, K_{Ic}, so that:

$$K_I \leq K_{IC}. \tag{2.8}$$

The stress intensity factor is evaluated numerically. The simulator uses the Willis-Richards et al. (1996) equation to model change in fracture hydraulic aperture due to shear displacement:

$$e = \frac{e_0}{\left(1 + 9\sigma'_n/\sigma_{eref}\right)} + D_{e,eff} * tan\left(\frac{\phi_{edil}}{1 + \frac{9\sigma'_n}{\sigma_{eref}}}\right), \tag{2.9}$$

where e_0 is the initial reference hydraulic aperture, σ_{eref} is the hydraulic aperture 90% closure stress, ϕ_{edil} is the hydraulic aperture dilation angle, and $D_{e,eff}$ is the effective cumulative sliding displacement, which is equal to the cumulative sliding displacement,

$D_{e,eff}$, but with a maximum value of 5 mm. A similar equation is used to model changes in void aperture using different constants: E_0 and σ_{Eref}, and with ϕ_{Edil} set to zero. The simulator uses iterative coupling (Kim et al., 2011) to couple the fluid flow and opening equations with the equations for fracture sliding.

A stochastically generated complex fracture network is used for each simulation. The networks are generated using specified statistics about the number of natural fractures, fracture lengths, and fracture orientations.

The locations of potentially forming hydraulic fractures must be specified in advance.The formation and propagation of hydraulic fractures is simplified in the model. The newly formed fractures propagate orthogonal to the direction of least principal stress. This is a simplification because in reality, the stresses can be rotated due to stress interaction with neighboring fractures, especially in formations with low stress anisotropy.

When the treatment begins, newly forming fractures initiate at random locations along the well bore and propagate perpendicular to the direction of minimum principal stress. Fractures are assumed to terminate when they meet existing natural fractures and new fractures propagate from the ends of the natural fractures.

Figure 2.3 shows an example of a fracture network used in a simulation. The figure shows map view of fracture network with all fractures assumed to be vertical going into the plane. The blue lines represent preexisting natural fractures. The red lines show the locations of potentially forming fractures (which may or may not form during the simulation). The black line represents the wellbore.

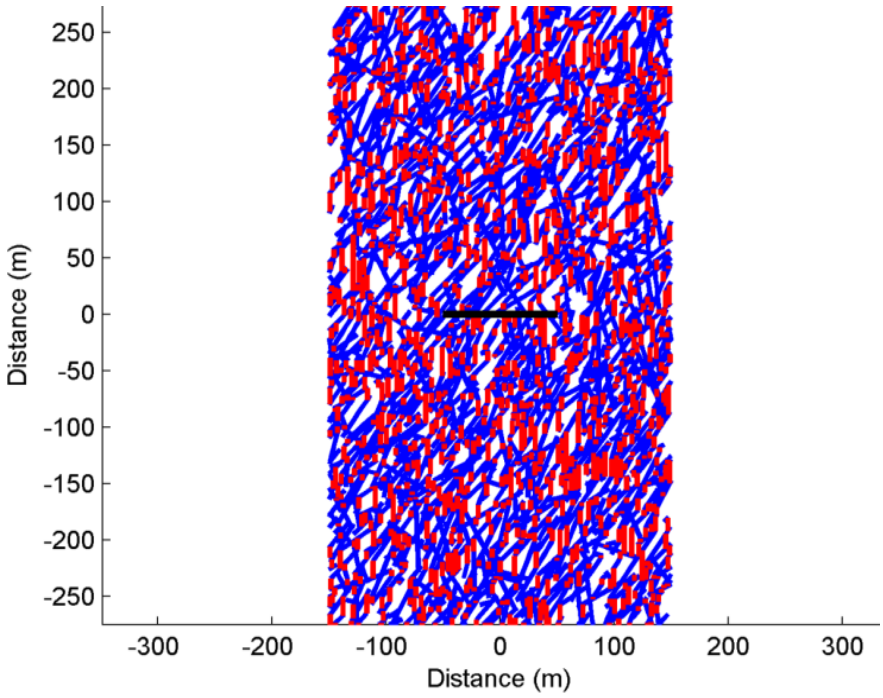

Figure 2.3: Fracture network used in the simulations. The black line in the middle shows the wellbore. Blue lines represent natural fractures. Red lines show the locations of potentially forming hydraulic fractures.

2.2.2 Variables for the Sensitivity Study

The properties that were varied for the sensitivity analysis were shear modulus (G), Poisson's ratio (υ), the coefficient of friction (μ, Equation 2.7), the hydraulic aperture 90% closure stress (σ_{eref}, Equation 2.9), the fracture toughness (K_{Ic}), the hydraulic aperture shear dilation angle (ϕ_{edil}, Equation 2.9), and the reference hydraulic aperture (e_0, Equation 2.9). Table 2.1 shows the maximum and the minimum values of the all the geomechanical properties that were varied in the study. Other properties were kept constant in all the simulations. Table 2.2 shows the values of other simulation parameters and geomechanical properties that were kept constant in the study.

Table 2.1: Summary of geomechanical properties varied in the simulations and their ranges.

Parameter	Maximum value	Minimum value	Units	Scaling
G	25000	5000	MPa	Cartesian
υ	0.35	0.15	Unitless	Cartesian
μ	0.6	0.4	Unitless	Cartesian
σ_{yy}	Critically stressed faults	23.86	MPa	Cartesian
K_{Ic}	9.0	1.5	$MPa.m^{0.5}$	Cartesian
σ_{eref}	90	10	MPa	Cartesian
φ_{edil}	5	0	Degrees	Cartesian
$e_0^3/12$	10^{-14}	10^{-17}	m^3	Logarithmic

Table 2.2: Summary of simulation parameters and geomechanical properties that were constant in all simulations.

Parameter		Parameter	
ρ_i	1000 kg/ m^3	μ_l	1 cp
Size of reservoir	300x550 m^2	*h*	100 m
No. of fractures	3046	σ_{xx} *(initial stress in x direction, minimum principal stress)*	23.86 MPa
E_0	0.001m	*Initial fluid pressure*	17.2 MPa
S_0	0.5 MPa	σ_{Eref}	20 MPa
$T_{hf,res}$	10^{-9} m^2	η	3 MPa/(m/s)
Itertol (error tolerance used in solving iterative coupling scheme, Section 2.3.9 of McClure and Horne, 2013)	0.01 MPa	η_{targ} *(for time stepping, Section 2.3.1 of McClure and Horne, 2013)*	0.4 MPa
mechtol (error tolerance used in solving shear stress equations, Section 2.3.5 in McClure and Horne, 2013)	.003 MPa		

The well was located from (-50, 0) to (50, 0) m. The well was not cased and so is hydraulically connected to all natural fractures intersecting the well. The fracturing fluid

was liquid water with no proppant. Injection was performed at 150 kg/s for 1800 s, and then the well was shut-in. The simulation was allowed to continue for 86400 s (one day) after shut-in.

2.2.3 SAMPLING METHODOLOGY

Sobol sequences were used to select the combinations of settings used in each simulation. 100 levels were chosen for design to efficiently cover the sample space. All values were scaled between the values 0 and 1. 200 quasi-randomly distributed points were generated in the hypercube. This gave a 200x8 matrix, where the rows denote twice the number of levels of design and the columns denote the number of variables in the sensitivity study. For implementation of the total effects algorithm, this matrix was then distributed into two to generate parent matrices A and B, each with 100 rows and 8 columns. Simulations were run on the settings generated from the parent matrices first. Appendix A and Appendix B give the scaled values obtained from the normalized values that were used in simulations.

Sister matrices need to be created from these parent matrices to calculate the total effects index for each variable, according to the algorithm of Saltelli et al. (2008). The sister matrices were created by sequentially replacing the columns of matrix B by the corresponding columns of matrix A. Replacing the first column of matrix B by the first column of matrix A creates sister matrix C1. Then replacing the second column of matrix B by second column of matrix A creates sister matrix C2. This procedure is repeated six more times and 8 sister matrices, C1-C8, are created. These give more the settings to run simulations. The settings are then scaled to give values for input in the model.

Shear modulus, Poisson's ratio, the coefficient of friction, fracture toughness, hydraulic aperture dilation angle, and the hydraulic aperture 90% closure stress were uniformly scaled between maximum and minimum values given in Table 2.1. The magnitude of the maximum horizontal stress was uniformly distributed from 23.86 (isotropic) to the value that would be required for the fractures to be initially critically stressed. The value of e_0 was scaled so that the value of $\log(e_0^3/12)$ were uniformly distributed.

2.2.4 SIMULATIONS OF CFRAC

A different stochastically generated fracture network was used in each simulation. However, they were statistically identical, with the same density, length, and orientation statistics. The fractures were preferentially oriented at a 30 degree angle with the y-axis.

Figure 2.4 shows the orientation statistics for two of the fracture networks used in the simulations. The fracture orientations are statistically similar even though they are stochastically generated.

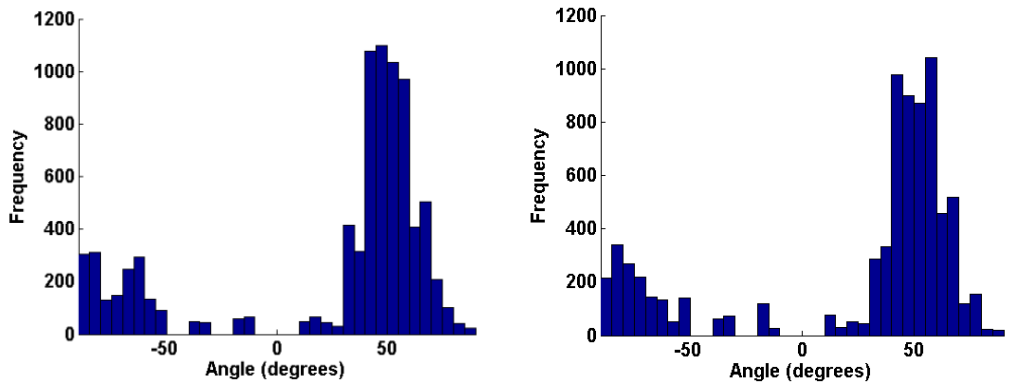

Figure 2.4: Fracture orientation statistics for two separate simulations.

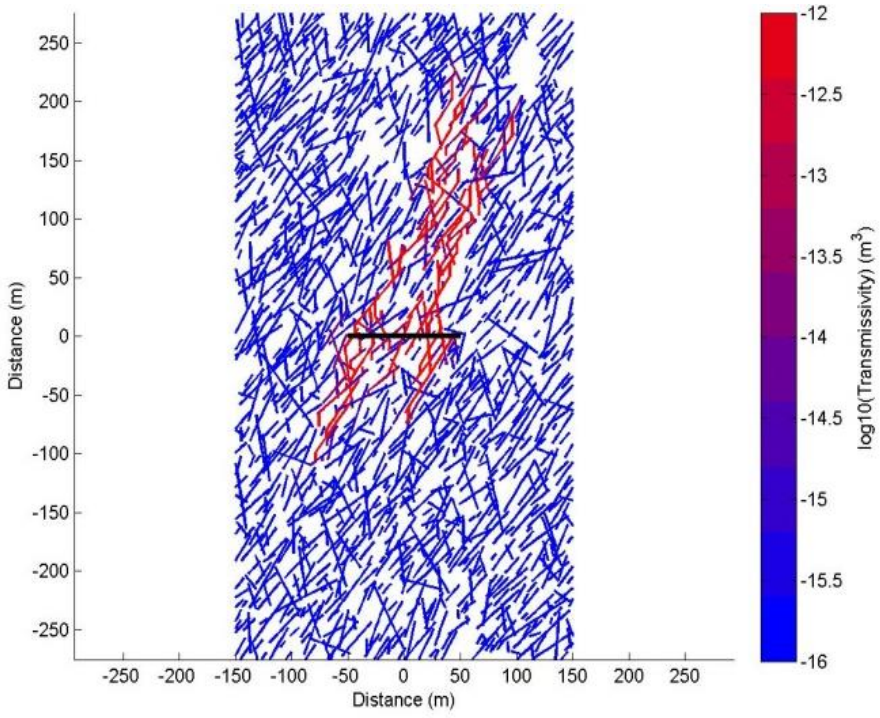

Figure 2.5: Example of the stimulated fracture network at the end of a simulation. The formation is viewed from above. The wellbore is the black line. The fracture color is proportional to transmissivity.

Figure 2.5 shows the distribution of transmissivity at the end of one of the simulations. In total, 1000 simulations were performed. In this particular simulation, the simulations settings were: shear modulus of 14,512.85 MPa, Poisson's ratio of 0.191, maximum principal stress of 36.27 MPa, initial reference hydraulic aperture of $6.66*10^{-5}$ m, dilation angle of 2.56°, coefficient of friction of 0.5521, fracture toughness of 7.28 MPa.$m^{0.5}$, and σ_{eref} of 27.70 MPa. The Texas Advanced Computer Cluster at The University of Texas at Austin was used for running the simulations.

2.2.5 CALCULATION OF STIMULATED RESERVOIR VOLUME

The output from CFRAC was post-processed to calculate the size of the stimulated reservoir volume (*SRV*). The concept of *SRV* was developed to analyze the microseismic observations acquired during fracturing and correlate microseismic data to well production after fracturing (Cipolla and Wallace, 2014; Mayerhofer et al., 2008). The *SRV* is used to understand the size of the region in the reservoir affected by the fracture treatment (Cipolla and Wallace, 2014). *SRV* is usually computed using microseismic data (Cipolla et al., 2008; Mayerhofer et al., 2008). It is now being used to examine the productivity of fracture treatment. *SRV* has also been used to see how fracturing affects well performance and ultimate recovery of hydrocarbons (Cipolla and Wallace, 2014).

In our post-processing algorithm for calculating *SRV*, an element was considered "stimulated" if its transmissivity at the end of the simulation was greater than 10^{-14} m^3. The size of the *SRV* was determined by dividing the reservoir into square blocks 1 m on each side. For each block, a calculation was performed to determine if it was within 10 m

of a stimulated fracture network. Then the area of the blocks was summed and multiplied by the formation thickness to derive *SRV*. Figure 2.6 shows an example simulation result with the stimulated fractures and the *SRV* generated by post-processing. Appendix C gives the values of *SRV* for all the 1000 simulation conducted in the study.

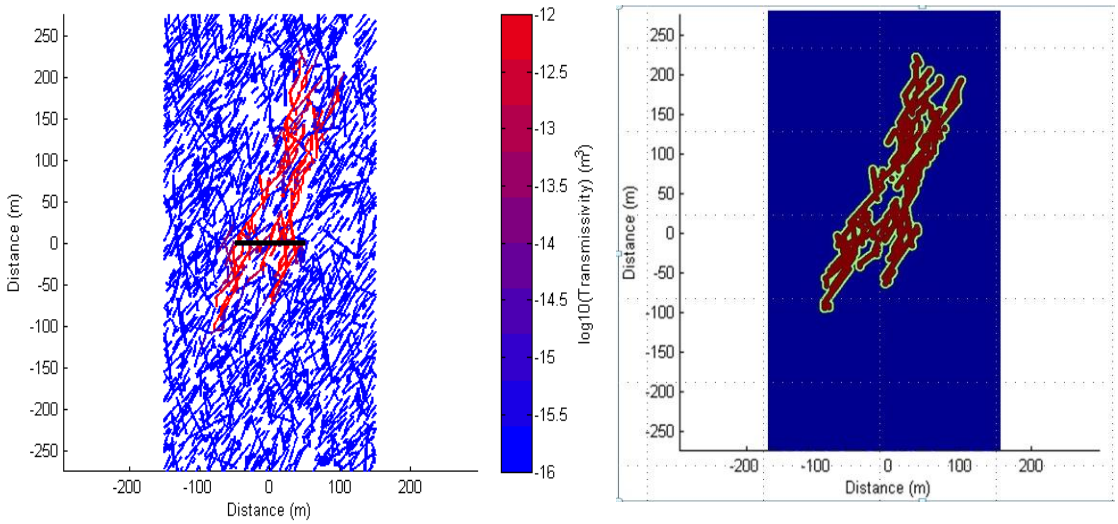

Figure 2.6: Fracture network after the treatment in simulation (left). The stimulatedreservoir volume (*SRV*) of shown as red, resulting from stimulation in the reservoir (right). The size of the *SRV* is 2,641,600 m^3.

2.2.6 ANALYSIS OF RESULTS

The methods that were used to analyze the results are:

(1) Scatter plots

(2) Multivariate linear regression

(3) Total effect index

(4) Goodness-of-fit test for tendency to create extreme values

2.2.6.1 SCATTER PLOTS

The input parameter is plotted on the x axis and the result (*SRV*) is plotted on the y axis. The scatter plots were made for the 200 quasi randomly distributed points only, not the full set of 1000 simulations. The relationships between parameters are more complex and nonlinear than can be explained with the simple concept of correlation, and scatterplots offer some ability to visually identify these relationships.

2.2.6.2 MULTIVARIATE LINEAR REGRESSION

Linear regression function takes the form

$$Y_t = b_0 + b_1X_1 + b_2X_2 \dots \dots + b_kX_k\,, \tag{2.10}$$

where Y_t is the output variable, X_1, X_2, ... X_k are independent input variables and b_0, b_1 , b_2 ... b_k are scalar coefficients. For our model Y_t is *SRV* and $X_{1,\dots}$ X_k are eight input geomechanical properties that are varied. Both inputs and the output were normalized between 0 and 1 before calculating the coefficients. This allowed us to analyze the variables on the same scale. The scalar coefficient of each variable gives the first order linear effect that the variable has on the output (*SRV*).

2.2.6.3 TOTAL EFFECTS INDEX

Total effects index is the contribution of an particular input to total output variance (Saltelli et al., 2008 p. 31). Variance based analysis decomposes output variance into components caused by different variables. Total effects index is defined as:

$$S_{Ti} = \frac{E_{X\sim i}\left(Var_{Xi}(Y|X_{\sim i})\right)}{Var(Y)} = 1 - \frac{Var_{X\sim i}\left(E_{Xi}(Y|X_{\sim i})\right)}{Var(Y)}, \quad (2.11)$$

where S_{Ti} is the total effects index due to variable I, *E* is the expected value operator, *Var* is the variance operator, the subscript *Xi* represents holding *Xi* constant and varying over all the other parameters, and *X~i* represents varying all variables except variable *i*.

For our study, simulations were run on the settings generated from the parent matrices A and B and the all sister matrices C1 to C8. The *SRV* values obtained from settings generated from matrix A are stored in vector y_A. Similarly, simulations run on settings generated from matrix B are y_B, and values of *SRV* obtained from settings in sister matrices are stored in vectors y_{C1}- y_{C8}. The *Var(Y)* was computed as

$$Var(Y) = \left(\frac{\Sigma(y_A)^2}{N} - \frac{(\Sigma y_A)^2}{N}\right), \quad (2.12)$$

Computing the product y_B, y_{C1} gives the first order effect of all the factors except *X1* and computing the product y_B y_{C2} gives the first order effect of all factors except *X2*. Similarly, products were computed for all the other 6 parameters. The numerator of Equation 2.7 can be computed by

$$Var_{X\sim i}(E_{Xi}(Y|X_{\sim i})) = \left(\frac{\Sigma(y_B y_{Ci})}{N} - \frac{(\Sigma y_A)^2}{N}\right), \quad (2.13)$$

Combining equations 2.12 and 2.13 gives all the values needed to calculate total effects index for the parameters in our study. The greater the value of total effects index, the greater the influence of the parameter on the *SRV*.

2.2.6.4 GOODNESS-OF-FIT TEST TO DETERMINE THE TENDENCY TO PRODUCE EXTREME VALUES

We performed this test in order to identify the tendency of parameters to produce very large values of SRV. Of the two-hundred simulations that were performed from the Sobol sequence, the 10% with the largest values of SRV were selected. Then, a cumulative distribution function (CDF) was plotted for each of the sensitivity variables in this subset of the simulations. If a variable has no effect on producing high SRV values, then the variable values in the top 10% SRV simulations should be random and the observed values should be uniformly distributed. But if certain values of the variable tend to contribute to large SRV, these will be preferentially sampled in the top 10% SRV simulations, and the observed distribution will deviate from a uniform distribution.

To quantify the effect of each variable, we performed a modified goodness-of-fit test between the empirical CDF and the uniform distribution. Common goodness-of-fit tests using an empirical CDF are the Cramer-von Mises test (Anderson, 1962) and the Kolmogorov-Smirnov test (Smirnov, 1948). A variety of other goodness-of-fit tests are available (Stephens, 1974). Most test methods involve taking the integral of a function of the empirical CDF and the CDF of the distribution to be compared against.

Typical goodness-of-fit tests provide a non-negative number, so we chose to calculate an unconventional test statistic that would provide either a positive or negative number, quantifying whether large values of the parameter lead to more or fewer large values of SRV, and conversely, whether small values of the parameter lead to more or fewer large values of SRV. Therefore, for each parameter, we calculated the statistic:

$$A = \int \left(F_n(x) - F(x)\right).dx \tag{2.14}$$

where *A* is the statistic, *Fn(x)* is the empirical CDF and *F(x)* is the comparison CDF, which was the uniform distribution, equal to *x*. If the *A* term was squared, this would be the Cramer-von Mises test. The obvious disadvantage of our equation is that it would be unable to accurately capture cases where the true empirical CDF crosses the uniform distribution - such as if high and low values of the parameter caused large values of SRV, but not middle values. But visual inspection of the empirical CDFs from our case indicated that this did not occur for the cases that we considered. If this was a potential issue, the result from Equation 2.10 could be compared to the result from a Cramer-von Mises test or (to be consistent) Equation 2.10 could have been modified to use the absolute value of the difference.

2.3 RESULTS AND DISCUSSION

Figure 2.7 gives the scatter plots of all the variables with the *SRV*. We can see strong positive correlation between the *SRV* and maximum principal stress in y direction (σ_{yy}), dilation angle (ϕ_{edil}) and initial fracture aperture (e_0). There is a weak negative correlation between *SRV* and coefficient of friction (μ), and *SRV* and the fracture toughness (K_{Ic}). There appears to be no correlation among the *SRV* and other properties.

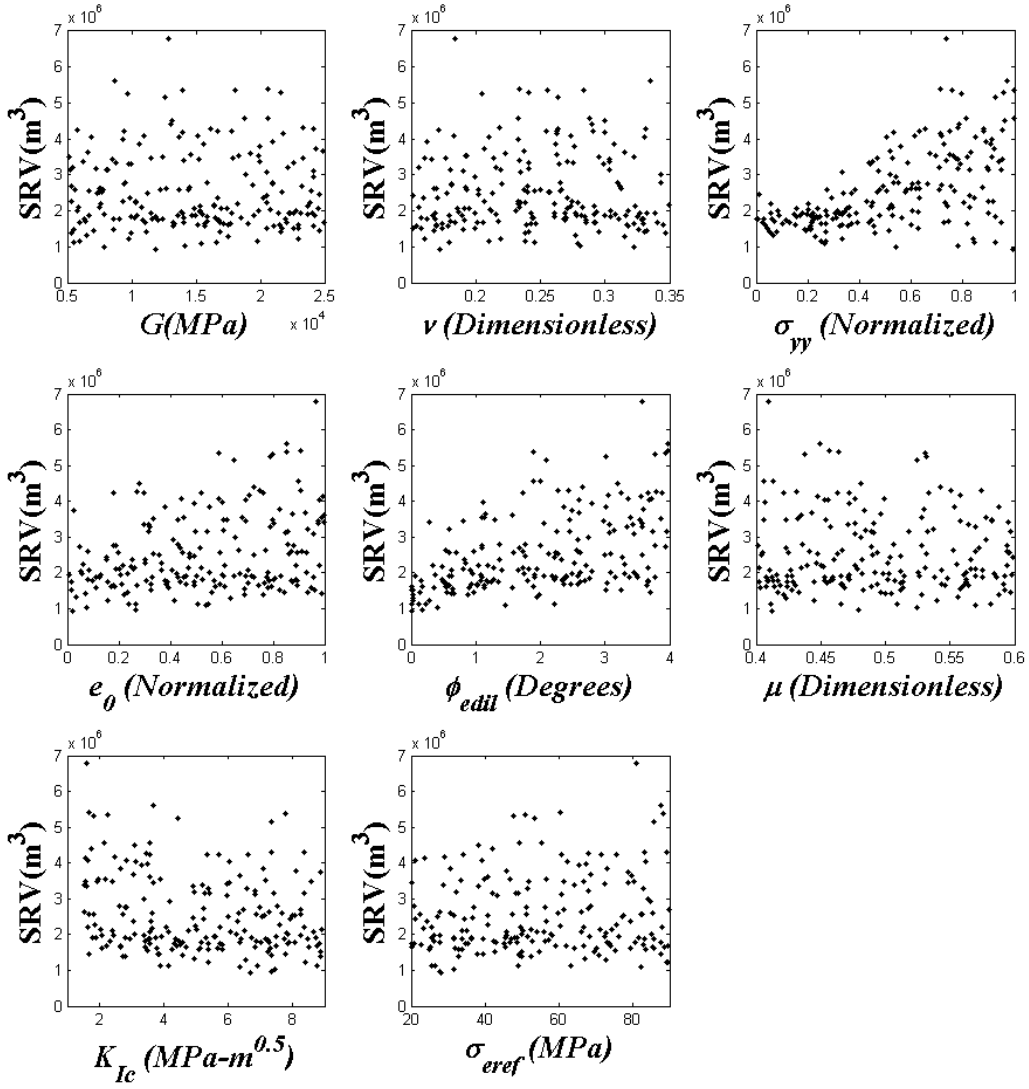

Figure 2.7: The scatter plots of the input parameters vs the *SRV*.

Figure 2.8 gives the normalized regression coefficients of the parameters. The maximum principal stress has the highest first order effect on the *SRV*, followed by the dilation angle, e_0, and $\sigma_{n,eref}$. The coefficient of friction and the fracture toughness have a negative correlation. Surprisingly, shear modulus and Poisson's ratio had minimal effect.

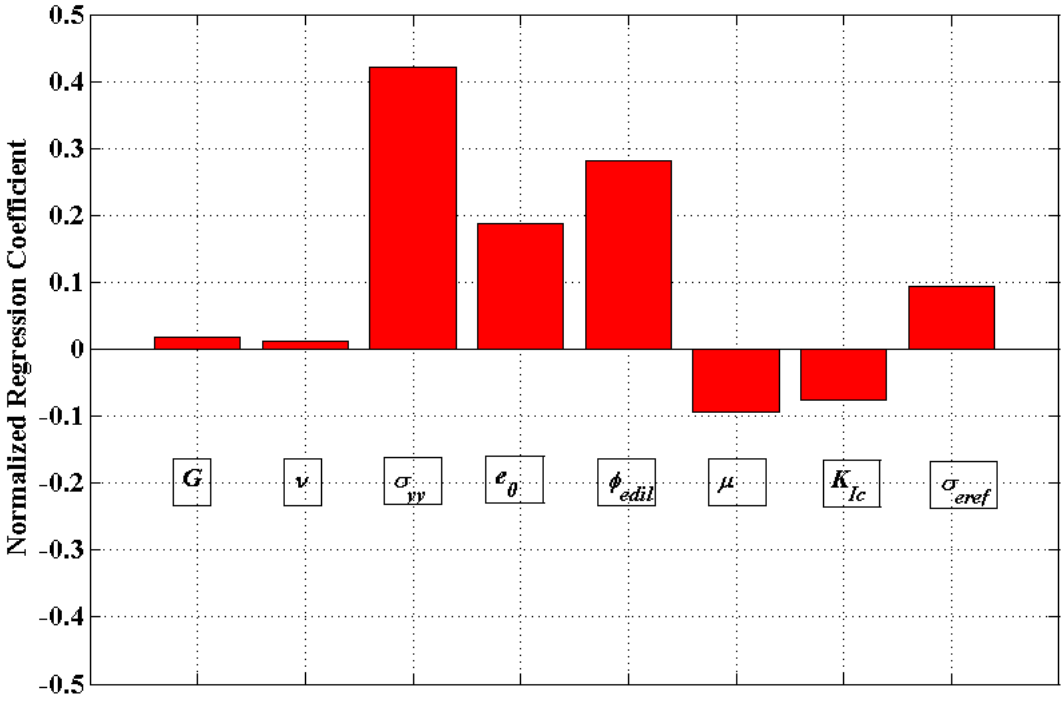

Figure 2.8: Normalized regression coefficients for all the input parameters.

Figure 2.9 shows the total effects index for all the input parameters. The maximum principal stress had the highest total effects index followed by dilation angle, reference hydraulic aperture, 90% closure stress, coefficient of friction, fracture toughness and finally the elasticity moduli. The total effects indices of some of the variables was exaggerated because of randomness created by using a different stochastically generated fracture network for every simulation. In a system with noisy response, the total effects index will tend to be elevated, even for variables that do not have a strong effect. This could have been reduced by running more simulations, but a significant investment of computational resources had already been expended to run the 1000 simulations used in the study.

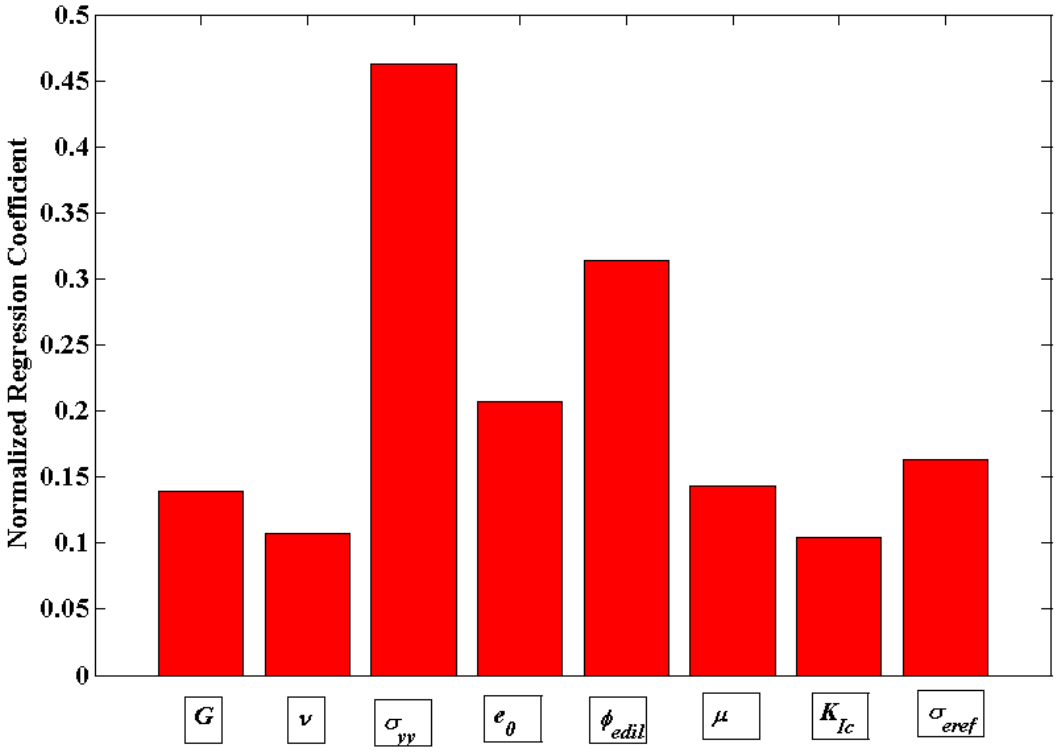

Figure 2.9: Total effects index for all the input parameters.

Figure 2.10 shows the CDF of the all the parameters for top 10% of *SRV* values. The CDF for dilation angle (middle) values lies below unit slope line showing a greatest positive effect (high values of the parameter causing high values of *SRV*). The CDF for fracture toughness (K_{Ic}) values lies above unit slope line, showing highest negative effect (low values of the parameter causing high values of *SRV*).

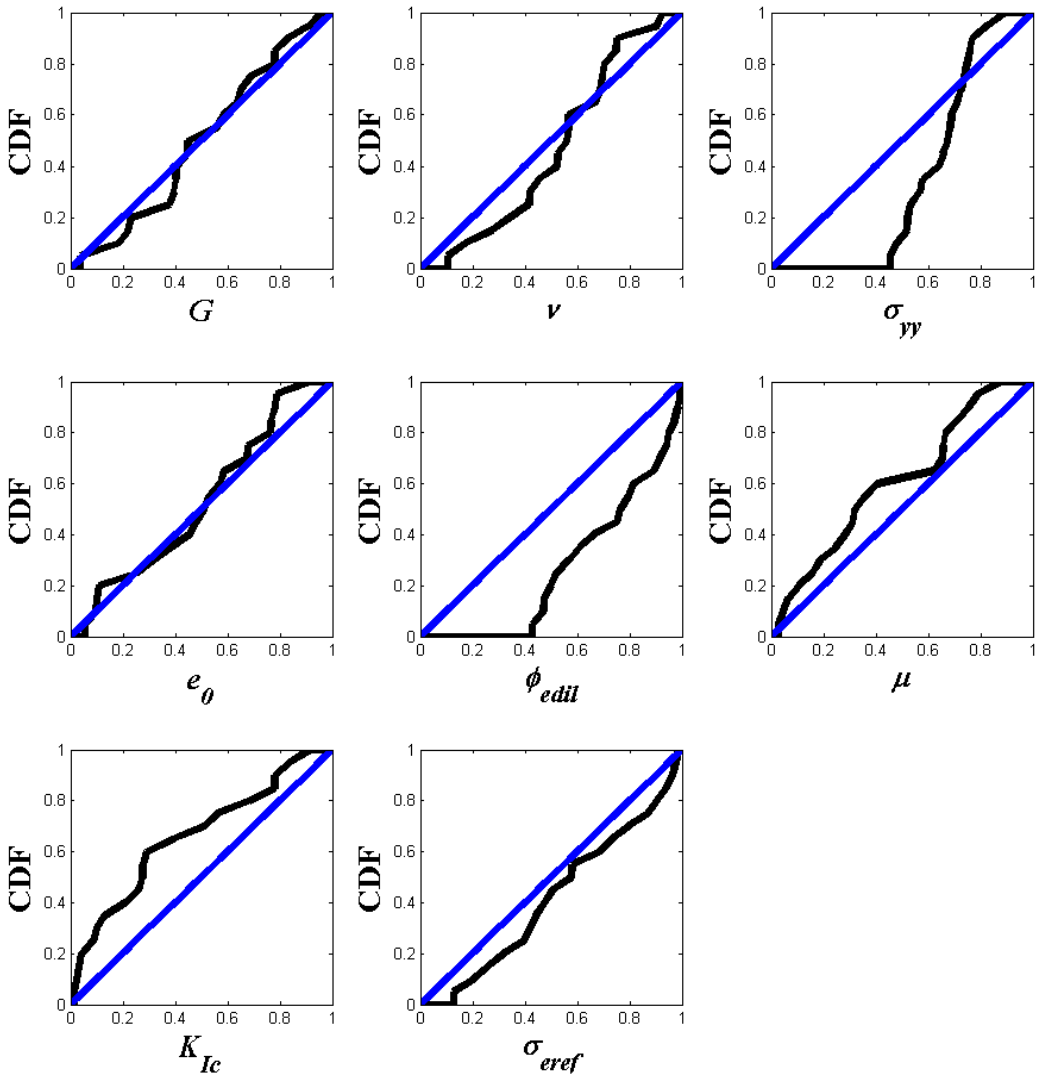

Figure 2.10: The empirical CDF plots of the input parameters vs the *SRV*.

Figure 2.11 shows the results obtained by applying the goodness-of-fit algorithm. The dilation angle had the largest positive area (showing a positive relationship), followed by maximum principal stress and the 90% closure stress. The coefficient of static friction and fracture toughness had a negative effect on the *SRV*.

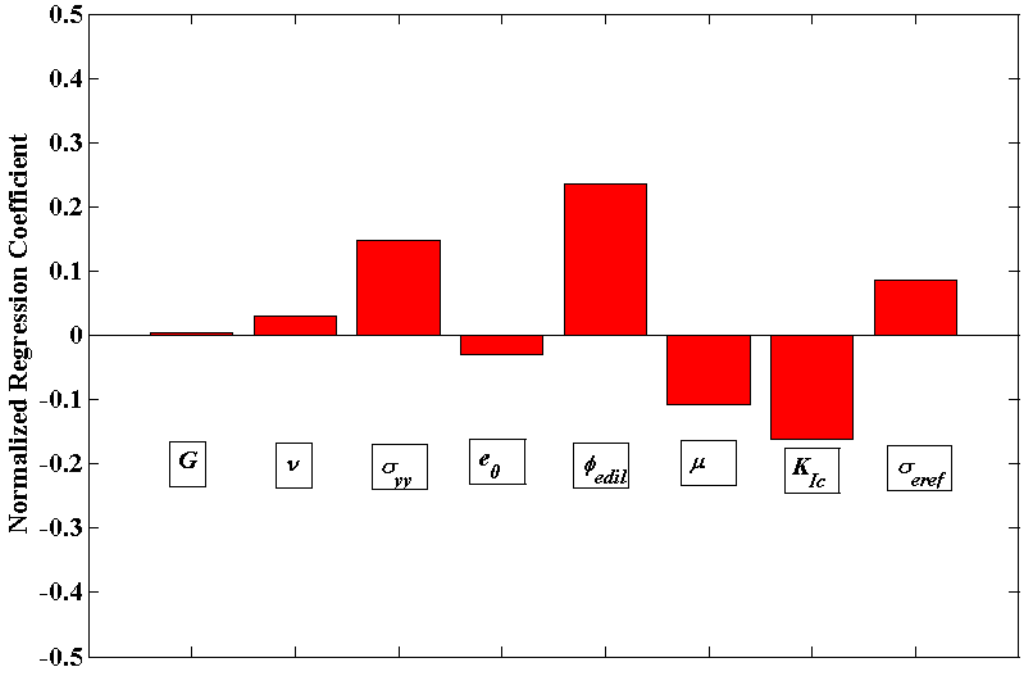

Figure 2.11: The area between the unit slope line and empirical CDF for all input parameters.

It can be observed from the scatter plots that the parameters that had a positive effect on the size of the *SRV* are the maximum principal stress, hydraulic aperture dilation angle, and initial fracture aperture. Fracture toughness and coefficient of static friction had a negative effect on *SRV*.

The maximum principal stress had the highest first order effect followed by dilation angle, initial fracture aperture. The 90% closure stress had a positive first order effect that was not apparent from the scatter plots.

The coefficient of static friction and the fracture toughness had a negative correlation with *SRV*. Surprisingly, the elasticity moduli (shear modulus and Poisson's

ratio) had no significant effect according to both the scatter plots and the normalized regression coefficients.

By definition, the total effects index must be a positive number. The magnitudes of total effects coefficient for inputs confirms the observation that the maximum principal stress and shear dilation angle were the parameters with the most significant overall contribution.

Finally, looking at the results from the goodness-of-fit tests, it can be inferred that high maximum principal stress with high dilation angle with low values of coefficient of static friction and fracture toughness were most conductive for high *SRV*.

It can be inferred from the results that shear stimulation of fractures is critical for developing a large *SRV*. Greater values of dilation angle cause existing fractures to open more upon shear displacement, increasing their hydraulic aperture. The reference hydraulic aperture, e_0, affects the initial transmissivity of the fractures, related to the rate at which fluid can seep into the fractures and cause stimulation. The 90% closure stress is related to both the initial and the stimulated transmissivity. Higher 90% closure stress results in higher fracture conductivity.

The coefficient of friction controls slip of hydraulic fractures (Equation 2.1). A lower coefficient of friction makes slip easier, increasing the amount of shear stimulation that can occur. Fracture toughness affects the ability for hydraulic fractures to propagate through the formation. Lower fracture toughness results in a larger *SRV*. However, these effects are relatively minor compared to the parameters that directly affect natural fracture transmissivity: the maximum principal stress, the reference aperture, and the dilation angle.

Increased value of maximum principal stress increases the anisotropy of stress in the reservoir. This increases the shear stress on the existing fractures, causing greater shear displacement and increase in hydraulic aperture of natural fractures.

The model did not take into account the fact that lower stress anisotropy can contribute to hydraulic fracture termination against natural fractures, which may contribute to fracture network complexity (Gu et al., 2011). Because of this, the results with respect to stress anisotropy may be misleading. There may be more than one way to generate complexity in a reservoir. With higher stress anisotropy, complexity could be generated from shear stimulation of the natural fractures. With low stress anisotropy, complexity could be generated from branching of the hydraulic fracture network due to termination against natural fractures and bedding planes.

To summarize, the parameters that affected unpropped fracture conductivity and the tendency for natural fractures to be shear stimulated were the most important for determining the size of the *SRV*.

2.4 CONCLUSIONS

Results suggest that the most important determinant for the size of the *SRV* was how readily fluid injection could stimulate natural fractures. The most important parameters were stress anisotropy, the hydraulic aperture shear dilation angle, and the reference hydraulic aperture (related to the initial fracture transmissivity).

Simulations did not take into account that hydraulic fracture termination and branching will be more likely in formations with low stress anisotropy. Therefore, the

relationship between stress anisotropy and the size of the *SRV* is in reality probably more complex than was observed in our study.

Simulations also did not take into account the potential for correlation between variables. For example, there may be a correlation between the elastic moduli of the rock and the shear dilation angle. So while our results suggested that the elastic moduli are not important by themselves, they may still be useful to measure because of their correlation with other parameters.

Overall, our results suggest that properties related to the unpropped fracture conductivity (both the initial conductivity and the conductivity after stimulation) are the most important for determining the size of the *SRV* created by injection. In the next phase of this study, we investigated whether this insight could be applied to predict well productivity at the field scale based on well logs.

2.5 Suggestions for Future Work

Our sensitivity study did not include any hydraulic fracturing design parameters, such as injection rate and fluid type. A more comprehensive study could be conducted that includes both the design and the geomechanical properties of the rock. More geomechanical parameters, like the cohesion of the rock, could be introduced into the study to make it more complete. More design parameters like the number of fracture stages, the time and pressure for fluid injection, could be added to make the study more detailed. More simulations could be conducted to better understand the total effects index of each parameter.

The CFRAC simulator uses some simplifying assumptions in natural fracture and hydraulic fracture interaction. These could be relaxed in future work. Research should be undertaken to understand the basic physics of interaction of hydraulic fracture with an existing natural fracture. More functions pertaining to proppant transport and viscous behavior of fracture fluid could be included in the simulator. Similar studies could be conducted with other codes to examine the validity of the results.

Chapter 3: Barnett Shale Case Study

3.1 INTRODUCTION

The sensitivity study described in Chapter 2 suggested that factors related to unpropped fracture conductivity are critical for determining the size of the *SRV*. If well log measurements could be used that predict the locations the regions along a well where unpropped fractures will have elevated conductivity, these regions could be preferentially stimulated to obtained more production. Unpropped fracture conductivity could also affect economic evaluation of prospective resources.

This chapter starts by reviewing core studies on the hydromechanical properties of fractures in shale. Next, mathematical models for unpropped fracture conductivity in simulators are discussed. Then, potential methods for predicting unpropped fracture conductivity from well logs are presented.

A comparative study was performed to see if well log observations could be used to predict well productivity, with a particular focus on log observations that may relate to fracture conductivity. The comparative study was performed with 15 wells from the Barnett Shale. Several approaches were tested, and ultimately a formula was identified that appeared to do a reasonable job of correlating the well productivity to the data obtained from the well logs.

3.1.1 HYDROMECHANICAL COUPLING IN SHALE

Many studies have documented hydromechanical properties of rocks with studies available for both igneous and sedimentary rocks (Ishibashi et al., 2012; Barton, 1976;

Makurat et al., 1996; Fredd et al., 2001; Unal et al., 2004). Zhang et al. (2013) discussed increase the fracture conductivity after shear displacement in the Barnett Shale core samples excavated from rock outcrops. In the experiment shown in Figure 4.1 (taken from Zhang et al. (2013)), the rock sample was artificially fractured. The sides of the fracture were offset by 0.1 inch, and fracture conductivity was measured. The study found a significant increase in fracture conductivity due to shear displacement.

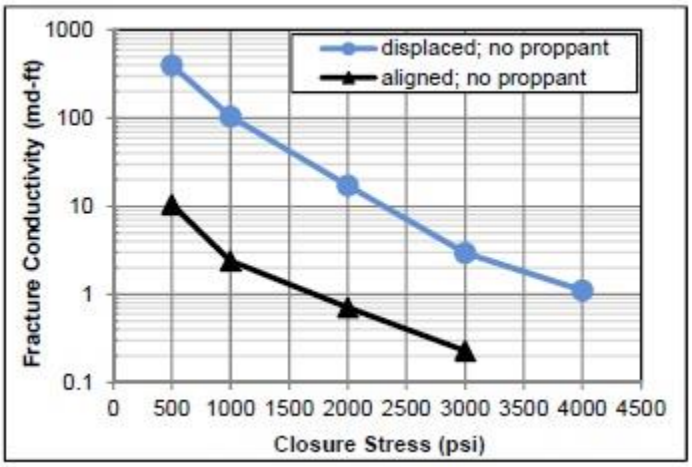

Figure 3.1: Increase of fracture conductivity due to offset of fracture faces. Figure reproduced from Zhang et al. (2013).

The change in hydraulic aperture due to shear is presented in Equation 3.1.

$$\Delta E_s = tan(D^0{}_n), \tag{3.1}$$

where ΔE_s is the increase in fracture aperture due to shear, $D^0{}_n$ is the dilation angle. The dilation angle can be modelled as a function of joint roughness coefficient (*JRC*) and the ratio of joint compressive strength (*JCS*) and the normal stress on the fracture face (Barton and Choubey, 1977).

$$D^0{}_n = \frac{1}{2} JRC * log\left(\frac{JCS}{\sigma_n{}'}\right), \quad (3.2)$$

where *JRC* is the joint roughness coefficient and *JCS* is the joint compressive strength (Barton and Choubey, 1977). The joint roughness coefficient *(JRC)* is an empirical measure of the roughness of the fracture. It depends on the behavior of asperities of the fracture (Barton and Choubey, 1977). Joint compressive strength *(JCS)* is the measure of the rock shear strength (Barton and Choubey, 1977). The relative performances of the Barton and Choubey (1977) model and other models were discussed by Co and Horne (2014).

JRC varies from 0-20, with 0 for smooth surfaces and 20 for very rough surfaces. The process of estimating *JRC* was given by Barton and Choubey (1977). The values can also be obtained from tilt tests or by comparing fracture profiles to predefined templates (Barton and Choubey, 1977).

JCS can be assumed to be equal to the unconfined compressive strength (*UCS*) for a completely unweathered rock (Barton and Choubey, 1977). The decrease in the value of *UCS* to *JCS* depends on weathering and rock permeability. An impermeable rock will weaken only near the fractured zone but a permeable rock will weaken throughout (Barton and Choubey, 1977).

For rocks in the subsurface this decrease in the value of *UCS* to *JCS* depends on the deposition environment and chemical action of interstitial fluid (Barton and Choubey, 1977). This effect was studied Chester and Logan (1986) for failure in the near-fault zones.

3.1.2 UNCONFINED COMPRESSIVE STRENGTH OF SHALE

The Barton and Choubey (1977) model demonstrates that *UCS* is related to the fracture dilation angle. It follows that fractures in rock with greater *UCS* should be more conducive to opening and dilation during hydraulic fracturing. Therefore, it may be possible to correlate well productivity to the rock mechanical properties using correlations for *UCS*. If we can predict the *UCS* using formation evaluation data, then we may be able to predict which zones will be more productive and conductive to successful hydraulic fracturing. It might also be possible to correlate *UCS* to other data obtained from field studies like the seismic data and identify regions in the reservoir that are more suitable for drilling.

The *UCS* has been shown to be a useful parameter used for calculating drilling penetration rates (Dupriest and Koederitz, 2005), in wellbore stability models (Zoback et al., 2003), and for determining in in-situ stresses (Nygaard and Hareland, 2007). Experimental studies on cores such as failure analysis give the most accurate estimates of *UCS* (Nabaei et al., 2010; Onyia 1988). Petro-physical studies have also correlated logging data to *UCS* (Nabaei et al., 2010; Onyia 1988). These correlations can be used to get a continuous reading of *UCS* along the wellbore where the log data is available.

3.1.3 UNCONFINED COMPRESSIVE STRENGTH FROM LOG DATA

The mechanical properties of the formation can be estimated from well log data. Wellbore breakouts can be detected from image logs or from the caliper reading (Sayers et al., 2005). Usually, breakouts are located in the direction of the minimum principal

stress (Sayers et al., 2005). Therefore, breakouts can help in determining the in-situ stress state and the direction and magnitude of stresses. For determining *UCS*, this method requires: a stability criterion, finding the magnitude and direction of maximum and minimum principal stresses using other studies such as leak-off tests and finding other rock properties such as angle of internal friction by experimental studies on cores. Different strength criteria, can give different values of *UCS*. Unfortunately, this method is imprecise and usually impractical because the magnitude of the maximum principal stress is not known with good precision.

There have been many studies correlating geomechanical formation properties directly to formation properties that are obtained from log data (Nabaei et al., 2010; Onyia 1988; Romana, 1999). The most common measurement that is used for determining *UCS* is the compressional sonic travel time (Δt_c) or the sonic velocity (Chang et al., 2006; Nabaei et al., 2010; Onyia, 1988). These are mostly empirical relationships that have been developed for specific rock formations and they should be used only after calibration for other formations (Chang et al., 2006; Nabaei et al., 2010).

Onyia (1988) presented a hyperbolic correlation between *UCS* and sonic log data:

$$UCS = K_1 + \frac{K_2}{\Delta t_c}, \tag{3.3}$$

where K_1 and K_2 are empirical constants for a particular formation type and Δt_c is the sonic travel time (Onyia, 1988). Another hyperbolic correlation presented in the work of Oynia (1988) is:

$$UCS = \frac{1}{K_3(\Delta t_c - K_4)^2} + 2, \tag{3.4}$$

where K_3 and K_4 are empirical constants that are calibrated for a particular formation type. Horsrud (2001) proposed the equation:

$$UCS = 0.77 * v_p^{2.93}, \tag{3.5}$$

where v_p is the compressional velocity in km/s obtained from compressional travel time measurement, and *UCS* is obtained in MPa (Horsrud, 2001). This relationship gave a good estimation when compared with *UCS* obtained from laboratory measurement for samples of North Sea shales, which demonstrates the importance of calibrating the empirical constants for specific formations (Horsrud, 2001).

Porosity measurement has also been used to correlate log data to *UCS* (Chang et al., 2006; Tokle et al., 1986). Density porosity, neutron porosity, and sonic porosity measurements have been correlated to *UCS* (Chang et al., 2006). Onyia (1988) used the density porosity measurements to find *UCS*, but the results did not correlate well with the actual *UCS* data. Horsrud (2001) used laboratory measured porosities to develop correlation for *UCS* data for shales in the North Sea.

The *UCS* of shale can also be correlated with the Young's modulus (Sayers et al., 2005). The Young's modulus can be directly estimated from sonic logs or from cores (Sayers et al., 2005). There are empirical correlations derived by Horsrud (2001) for shale in the North Sea that correlate *UCS* to Young's modulus measurement (Sayers et al., 2005).

Chang et al. (2006) provided a list of correlations that have been derived to obtain *UCS* in shale and discussed limits of their application. Chang et al. (2006) also compared the relative performance of different correlations and compared them with laboratory measured values of *UCS.* The correlations that use compressional travel time provide the most reasonable estimates of the *UCS* (Onyia, 1988).

3.1.4 Well Logs used for Analysis

The logs used in this study were the gamma ray log, neutron porosity log, and acoustic log.

Gamma ray tool detects the gamma rays coming from the naturally occurring radioactive elements in the formation (Ellis and Singer, 2007, p.268). The most common elements are potassium-40, uranium and thorium. Potassium-40 and thorium are usually associated with clays, and uranium is associated with organic carbon or kerogen present in the formation.

The neutron porosity tool detects hydrogen (Ellis and Singer, 2007, p.352). If fluid (water, oil or gas) in rock pores contains most of the hydrogen, then the tool will detect rock porosity. The tool measures the size of the static neutron cloud developed as a neutron source moves in the borehole. The size of this cloud depends on the collisions of neutrons with elements in the formation. Neutrons are mainly slowed down by hydrogen nuclei present in the formation. The neutron tool has to be calibrated to the type of fluid and type of matrix in the formation. Logs calibrated with formation brine show decreased values of neutron porosity in the presence of gas. This response is used to identify the presence of formation gas. In shale, the neutron response is complicated by the presence

of clays. Clays usually contain strong neutron absorbers that can influence the readings of the neutron logs. The neutron porosity should be corrected for the fraction of clay in the formation before it could be used to identify the presence of gas.

Sonic logs measure the travel time for propagation of sound waves through the formation (Ellis and Singer, 2007, p.480). In the log data that was available for this study, the compressional travel time measurement was used to evaluate formation *UCS*. The travel time of compressional waves in the formation is controlled by lithology, porosity, and the type of fluid present in the pores. The sonic travel time is used to calculate sonic porosity of the formation using Wyllie's correlation (Ellis and Singer, 2007, p.495):

$$\phi_s = \frac{\Delta t_c - \Delta t_m}{(\Delta t_f - \Delta t_m)}, \tag{3.6}$$

where Δt_c is the measured values of travel time, Δt_m is the matrix travel time, and Δt_f is fluid travel time. The sonic porosity is proportional to Δt_c. Change in formation fluid from water to gas increases the sonic travel time and consequently the sonic porosity. This increase may be interpreted as an indicator of presence of gas in the formation. We used travel time to interpret the *UCS* of the formation using Equation 3.7 (Chang et al., 2006). This response is complicated by the presence of clays in the matrix. Increased fraction of clays usually decreases the matrix travel time and causes erroneous interpretation. It is important to correct for clays before sonic porosity results are used.

3.1.5 BARNETT SHALE

The Barnett Shale is one of the highest producing gas shale plays in the world (Pollastro, 2007). Figure 3.2 shows the location of the Barnett Shale in Texas. The shale is situated in the Fort Worth Basin in the northern part of Texas (Hill et al., 2006). Fort Worth basin has an area of more than 15,000 mi^2 (Pollastro, 2007). The Barnett Shale outcrops near the Llano uplift and goes deeper in the northeast near the Texas-Oklahoma border (Hill et al., 2007). The thickness of the Barnett Shale ranges from about 50 ft in the south to more than 1000 ft. in the northern part (Hill et al., 2007). The Barnett overlies the Viola-Simpson in the north and the Ellenberger in the south (Pollastro, 2007). It is overlain by Marble Falls Limestone in the entire region. A layer of limestone, called the Forestburg Limestone, passes thought the Barnett in the northern part of the shale (Pollastro, 2007).

Gas is mainly produced from the northeastern part of the Barnett known as the Newark East field (Jarvie et al., 2007; Pollastro, 2007). It has an area of more than 6000 mi^2 (Zhao et al., 2006). This region is considered to be the productive zone of the Barnett (Hill et al., 2007). It covers about 15 counties in Texas and with depths ranging from 6500'-9000' (Aguilar and Verma, 2014; Pollastro, 2007). This region has unproven reserves of 26 Tcf of gas (Pollastro, 2007).

The Barnett Shale hale is heterogeneous at all scales but contains on average 30-60% clays, 25-35% quartz, 7%-25% carbonates, and 4%-15% organics (Kinley et al., 2008). The dominant clay types in the formation are illite and kaolinite (Kinley et al., 2008). The porosity ranges from 3.8%-6% (Zhao et al., 2006; Kale et al., 2010). Fracturing is necessary in the Barnett in order to economically produce hydrocarbons

from the shale (Kale et al., 2010). The Viola Simpson, under the Barnett, contains dense limestone and dolomite and forms a good fracture barrier (Jarvie et al., 2007). The wells can be drilled deeper and fractured with low risk of job failure. The Ellenberger made of chert, dolomite, and limestone, is a water bearing and does not form a good fracture barrier (Jarvie et al., 2007; Pollastro et al., 2007). The wells are usually drilled high in the southern part of the Barnett to prevent their interaction of hydraulic fractures with the Ellenberger (Jarvie et al., 2007). The Marble Falls Limestone serves as a good barrier for fracture containment (Jarvie et al., 2007).

The Barnett Shale contains the Type II kerogen (Kinley et al., 2008). Initially the kerogen in the shale produced oil. The oil later cracked to produce gas. Most of the gas is associated with the organic matter in the shale. The shale has total organic carbon (TOC) in the range of 4%-13% by weight (Kinley et al., 2008). Organic rich regions are found to have TOC of 4.5% (Kinley et al., 2008). The vitrinite reflectance of Barnett is greater than 1.0 in most of the region. Hence the Barnett mainly produces condensate and dry gas (Kinley et al., 2008).

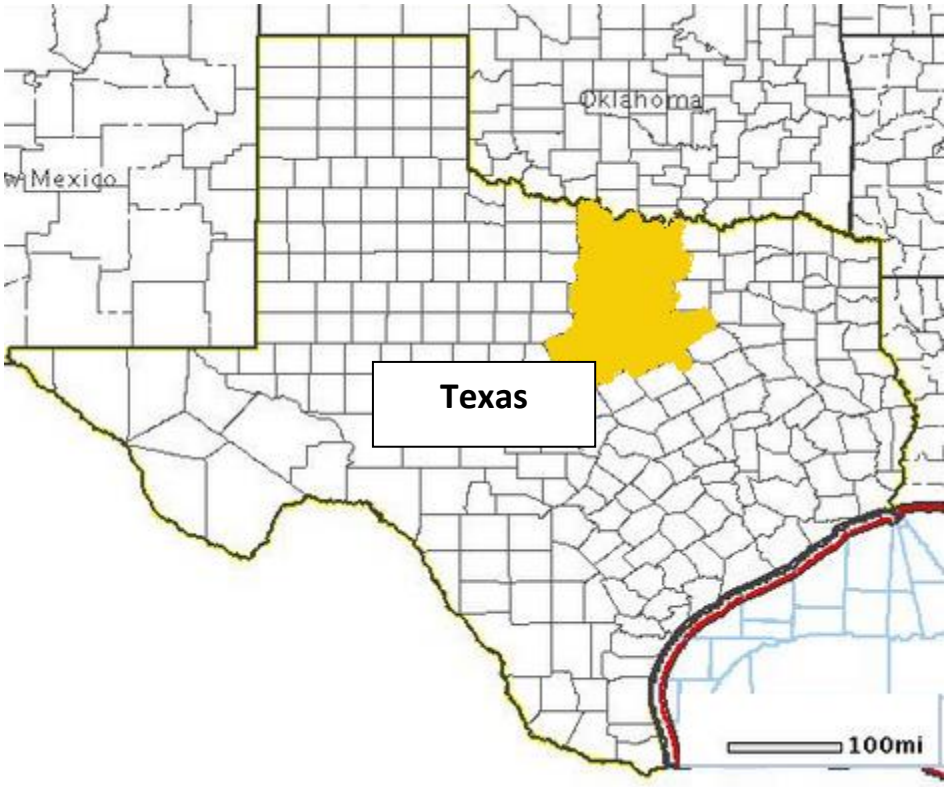

Figure 3.2: Location of the Barnett Shale in Texas. The shale is located in the northern of Texas and covers 28,000 mi^2.

3.2 METHODOLOGY

Our hypothesis is that regions or zones that have higher *UCS* will have higher unpropped fracture conductivity and will have higher long term production.

This hypothesis was tested by doing a comparative study with 15 wells from the Barnett Shale. The wells chosen for the study lie in the Newark East field of the Barnett. Figure 3.3 shows the region where the wells are situated in the Barnett. The well data was taken from publically available databases, such as Drillinginfo and Texas Railroad Commission database.

The wells were chosen because they were all vertical and had gamma ray, sonic and neutron logs available. An exhaustive search of the database was performed, and these were the only 15 wells that met those criterion. Because they were vertical wells, they tended to be wells drilled and fractured in the early 2000s.

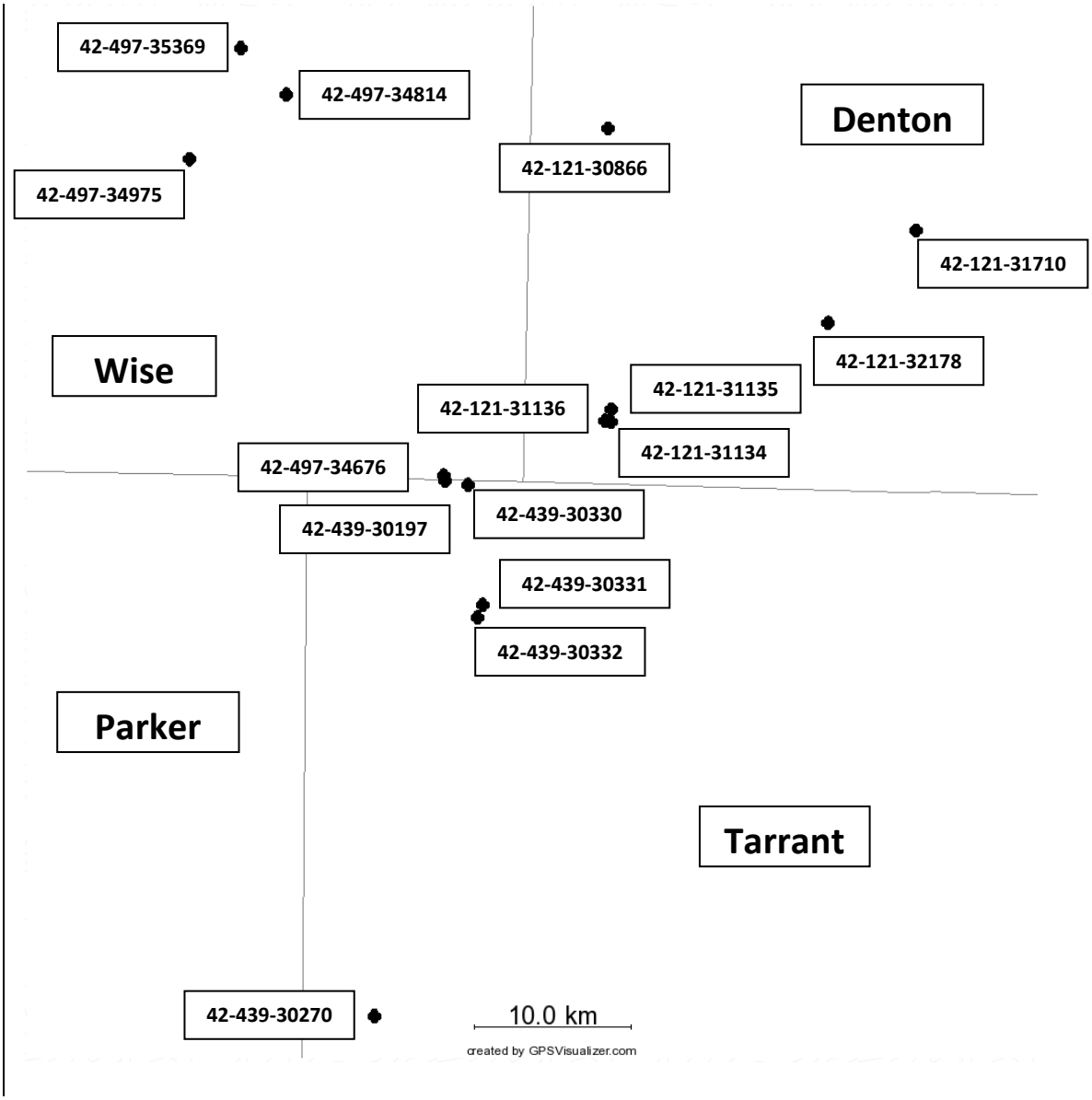

Figure 3.3: Location of wells in the Barnett Shale in Texas. The wells are located in the Newark East field in the northwestern part of the Barnett Shale.

First, we visually compared the logs to the 15 month production from each well. Based on the visual inspection and our prior hypotheses about the importance of *UCS*, we developed hypotheses about the optimal well log conditions for productivity. We developed mathematical relations that give preferential weights to the zones in well logs that show suitable gamma ray, sonic and mechanical properties. These equations were used to calculate a single number for each well, which we hoped would correlate with production. To test the relations, the values were cross-plotted against the cumulative production after 15 months.

Sonic porosity was calculated using Equation 3.6. Δt_f was taken as 189 μs/ft for water and Δt_m was taken as 47.6 μs/ft for limestone in accordance with the values used in the log. The correlation to compute *UCS* was taken from the work of Chang et al. (2006)

$$UCS = 1.35 * \left(\frac{304.8}{\Delta t_c}\right)^{2.6}, \tag{3.7}$$

where Δt_c is in μs/ft and the *UCS* is computed in MPa. This type of inverse relationship of *UCS* with sonic travel time was used in Lawrence Berkeley National Laboratory (2013) study to evaluate the *UCS* of different shale formations in the United States. These correlations were found to give reasonable estimates of the *UCS* even without calibration. Using this correlation with the sonic log data can provide a continuous measurement of *UCS* along the wellbore. Because the *UCS* correlation could not be calibrated with core, the absolute value of the estimates may be inaccurate. However, the relative value of *UCS* between wells will hopefully be accurate, permitting a reasonable comparison.

3.3 RESULTS

The depth to the top and bottom of the Barnett in each well is given in Table 3.1. The location of the bottom of the Barnett is not known for some of the wells because the well was not logged to that depth. The wells are situated between the depths of 6500'-9000'. The cumulative water used and the cumulative proppant injected during fracking is presented in Table 3.2. The proppant used in the treatment was mostly 20/40 and 40/70 mesh. The water and the proppant volumes used in each fracture shows no real correlation with cumulative production of 15 months from the wells (Figure 3.4 and Figure 3.5).

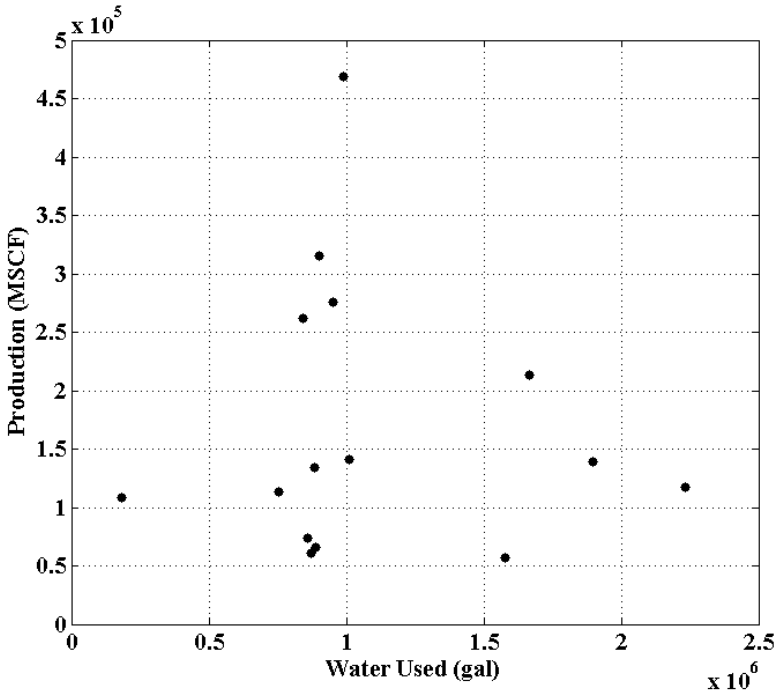

Figure 3.4: Water used in the fracture treatment vs cumulative 15 gas production.

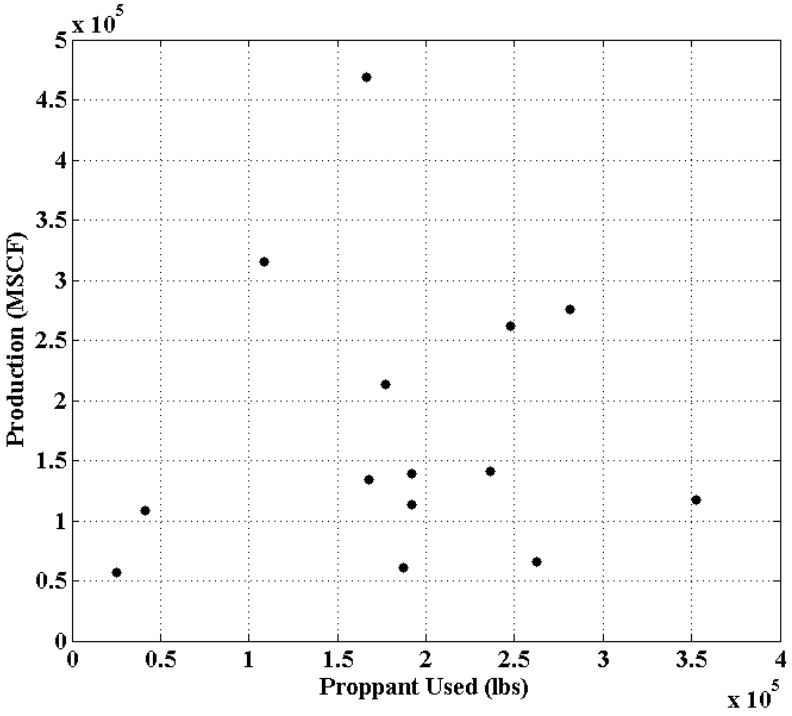

Figure 3.5: Proppant used in the fracture treatment vs cumulative 15 month gas production.

Table 3.1: Top and bottom reported perforation depths and log depths.

	WELL	BARNETT SHALE		LOG DEPTH		PERFORATION DEPTHS	
	API NUMBER	TOP (ft.)	BOTTOM (ft.)	TOP (ft.)	BOTTOM (ft.)	TOP (ft.)	BOTTOM (ft.)
1	42-121-30866	7682	8466	7200	8600	7752	8440
2	42-121-31134	7199	-	7000	8000	7566	7906
3	42-121-31135	7215	-	7100	7950	7523	7894
4	42-121-31136	7202	-	7000	7800	7372	7762
5	42-121-32178	7717	-	7600	8200	7888	8420
6	42-439-30197	6788	7141	6700	7150	6788	7065
7	42-497-34676	6850	7210	6800	7250	6854	7160
8	42-497-34814	7339	7976	7000	8050	7360	7944
9	42-497-34975	7065	7616	7000	7700	7070	7510
10	42-497-35369	-	-	7000	7900	7282	7850
11	42-121-31710	8190	-	8100	8800	8204	8644
12	42-439-30330	7002	-	7050	7370	7006	7330
13	42-439-30331	7278	7630	7200	7600	7304	7538
14	42-439-30332	7131	7472	7100	7500	7154	7402
15	42-439-30270	6640	-	6600	6890	6652	6856

Table 3.2: Water and proppant volumes used for hydraulic fracturing of the wells. 15 month and 10 year cumulative gas production.

	WELL	WATER	PROPPANTS	PRODUCTION	PRODUCTION
				(15 months)	(10 years)
	API NUMBER	(GAL)	(lb.)	(MSCF)	(MSCF)
1	42-121-30866	1665000	177250	213053	607590
2	42-121-31134	754152	192000	113346	409892
3	42-121-31135	182322	41050	108341	238621
4	42-121-31136	1011738	236000	141043	453240
5	42-121-32178	1577177	25000	57067	168602
6	42-439-30197	900144	108900	315189	1016022
7	42-497-34676	988554	166500	468861	2056895
8	42-497-34814	1898568	192000	139181	397443
9	42-497-34975	882798	167864	134315	281209
10	42-497-35369	860916	242500	73626	214710
11	42-121-31710	2231374	352400	117649	391351
12	42-439-30330	843738	248000	262074	981310
13	42-439-30331	950922	281600	276015	805501
14	42-439-30332	889350	262500	65775	444091
15	42-439-30270	870660	187300	60868	132882

The wells produced primarily gas and a small amount of liquids. To summarize production with a single number, we used 15 month gas production.

Figure 3.6 show that cumulative 15 month production exhibits a good correlation with cumulative 10 year production of the wells. The production data shows wide variation between wells.

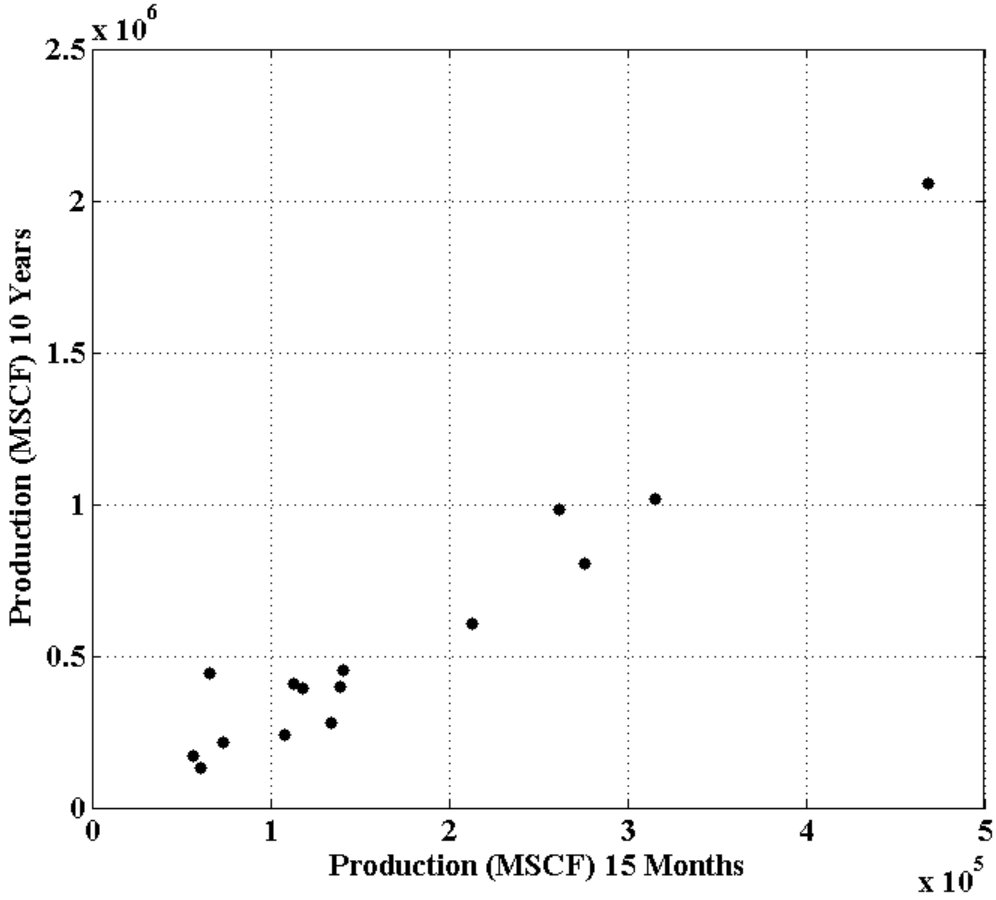

Figure 3.6: Cumulative 15 month and cumulative 10 year production of the wells in MSCF in scatter plot.

Figure 3.7 and Figure 3.8 show monthly production for two wells, 42-497-34676 and 42-121-31136. The production for all the wells used in analysis is given in Appendix D. Most wells how production trend similar to well 42-121-31136, with a high initial production and a rapid decline. But different trends can also be seen in the trends from production of the well 42-497-34676. Some wells were shut-in at different points in time and/or have unusually fluctuating production that must be due to operational issues. However, as Figure 3.6 shows that there is a good correlation for 15 month production and 10 year production, and so these operational issues are secondary effects.

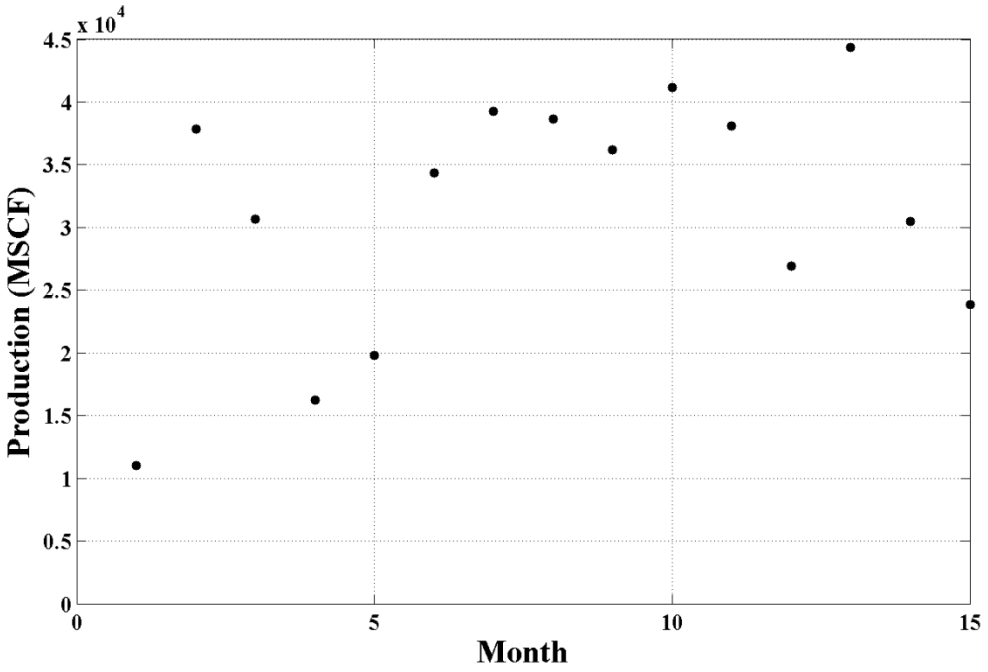

Figure 3.7: Production trends for well 42-497-34676.

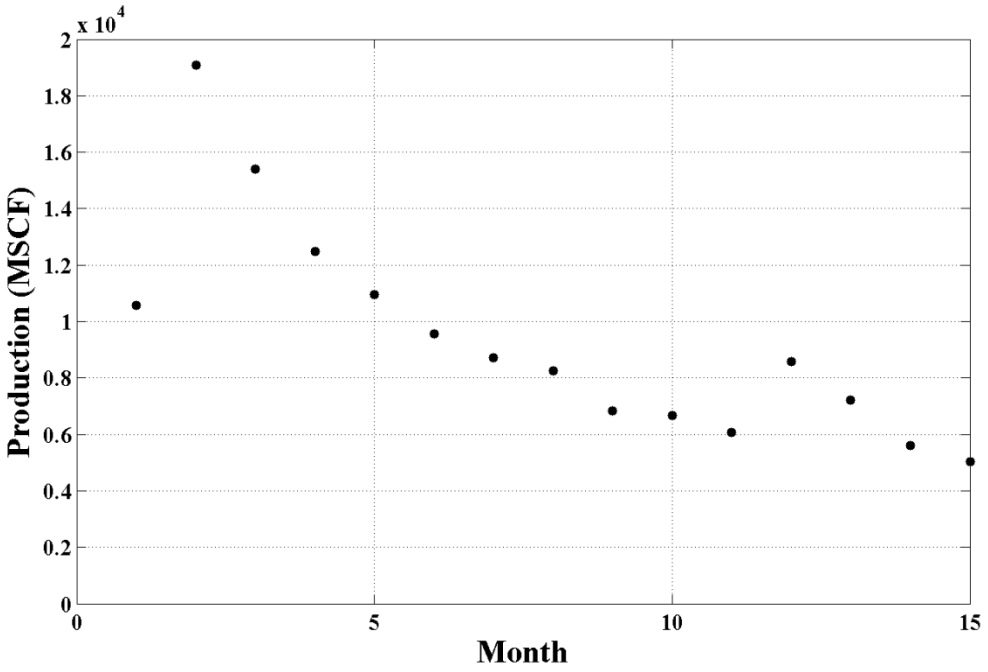

Figure 3.8: Production trends for well 42-121-31136.

3.3.1 ANALYSIS OF WELL LOGS

Figure 3.9 and Figure 3.10 shows the well logs for wells 42-439-30330 and 42-121-30866 respectively. The logs for all the other wells are presented in Appendix E. The Barnett shows a characteristic increase in gamma ray reading, as observed in track 3 of Figure 3.9 and Figure 3.10. The Barnett also shows a characteristic increase in sonic porosity and decrease in neutron porosity. This can be observed at depths between 7060' and 7100' in Figure 3.9 and between 7920' and 8010' in Figure 3.10 and in logs in Appendix E. These trends are similar for all the wells in this study. The Barnett Shale shows higher gamma ray reading than Marble Falls and Viola Simpson, so a bed boundary can be detected in the gamma ray log as can be observed in Track 3 of Figure 3.9 between the depths of 7000 ft. to 7370 ft. and in track 2 of Figure 3.10 between 7680 ft. and 8466 ft. The layer of Forestburg Limestone can also be identified from a sudden decrease in gamma ray readings from 7060' and 7100' in Figure 3.9 and between 7920' and 8010' in Figure 3.10. This can also be observed in other logs in Appendix E.

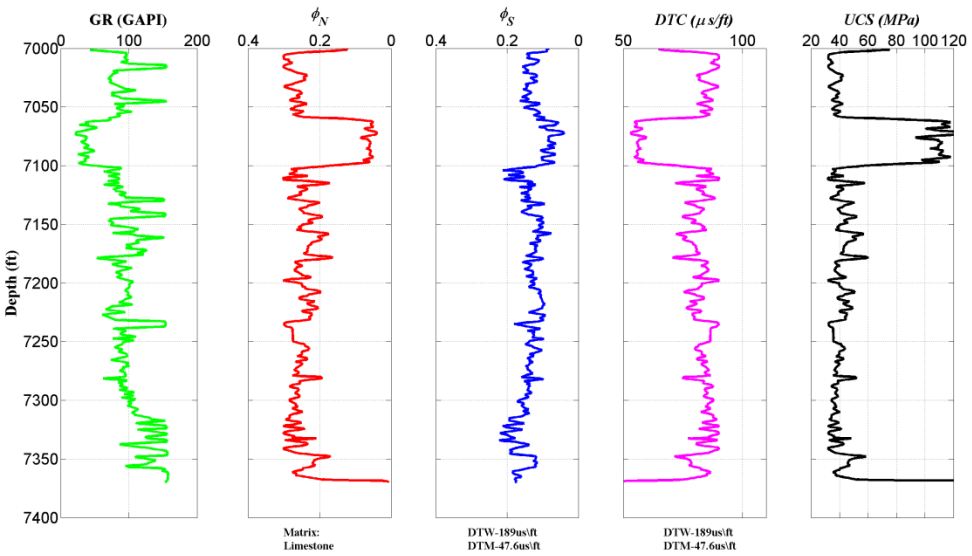

Figure 3.9: Well logs for the well 42-439-30330.

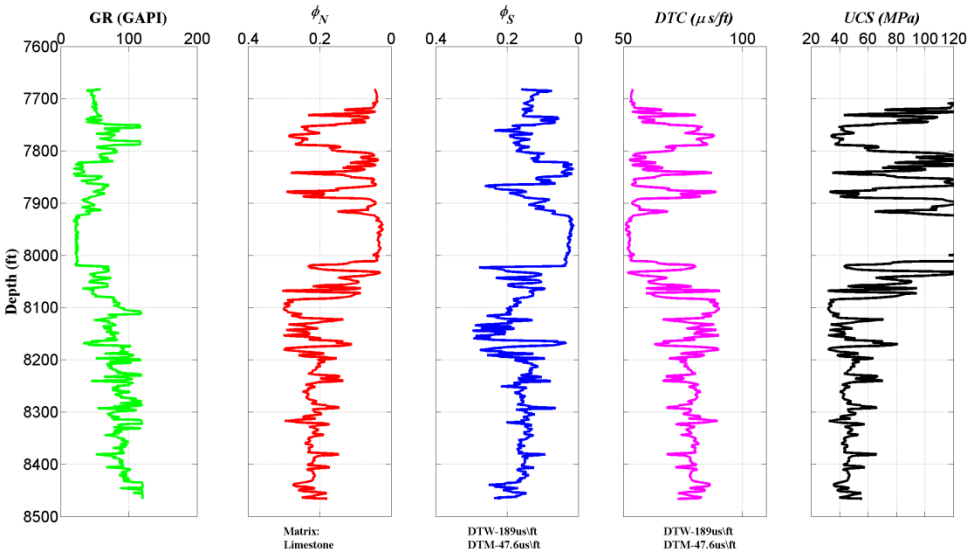

Figure 3.10: Well logs for the well 42-121-30866.

The increase in gamma ray reading in the Barnett could be due to an increase in organic content or due to an increase in the clay content. The amount of organics present

is important because in the Barnett, gas in place is closely correlated with the fraction of organic content in the formation (Kinley et al., 2008). Clay content is detrimental to production because it reduces matrix permeability (and also probably reduces unpropped fracture conductivity). Ideally, a spectral gamma ray low would be run that can distinguish between gamma ray from clay and organic content. But in this study, spectral gamma ray logs were not available.

Based on our visual inspection of the logs, we hypothesize that the optimal gamma ray reading is between 80 GAPI and 110 GAPI. Gamma ray readings less than 80 GAPI may indicate an organic poor rock that does not have sufficient hydrocarbons in place. Gamma ray readings greater than 110 GAPI may indicate a clay rich rock where production will be challenging due to low permeability.

The Barnett shows a crossover between sonic porosity (*sphi*) and neutron porosity (*nphi*). To test whether the sonic and neutron porosity could be used to identify productive zones, we experimented with giving more weight to zones that show significant separation of *sphi* and *nphi*. We defined a significant separation to be 0.05 porosity units between *sphi* and *nphi.* However, this measurement was complicated because the responses of neutron and sonic porosity logs are affected by the presence of clays in shale.

Finally, we considered the *UCS* of the shale. The Barnett has a lower *UCS* than the surrounding Marble Falls and the Viola Simpson. This contrast is clearly noticeable in Figure 3.9 and to a lesser extent in Figure 3.10. The Forestberg Limestone has a higher *UCS* than the surrounding Barnett. According to our hypothesis, higher *UCS* should be beneficial for gas production. But conversely, high *UCS* could mean that porosity and

permeability are too low for rock to effectively conduct hydrocarbons. Based on inspection of the well logs, we estimated the optimal *UCS* range to be from 40 MPa and 65 MPa.

3.3.2 LOG ANALYSIS RESULTS

The effect of perforations was modelled by using a step function, assigning a weight of 1 to a perforated depth and 0 to a non-perforated depth.

$$g = 1 \; if \; perforated \; , \qquad (3.8)$$
$$g = \; 0 \; if \; not \; perforated,$$

where *g* is the weight decided by the model.

Depths with our hypothesized optimum reading of gamma ray were given higher weights according assigned according to a Gaussian like distribution with mean of 95 GAPI and standard deviation of 15 GAPI:

$$f = e^{\frac{-(GR_h - 95)^2}{15^2}} \; , \qquad (3.9)$$

where GR_h is the gamma ray reading at a particular depth in the well and where *f* is the weight decided by the model.

The product *f***g* was defined as objective function 1. The integral of the objective function was calculated along the borehole for all the wells and is plotted against 15 month gas production for all the wells in Figure 3.11.

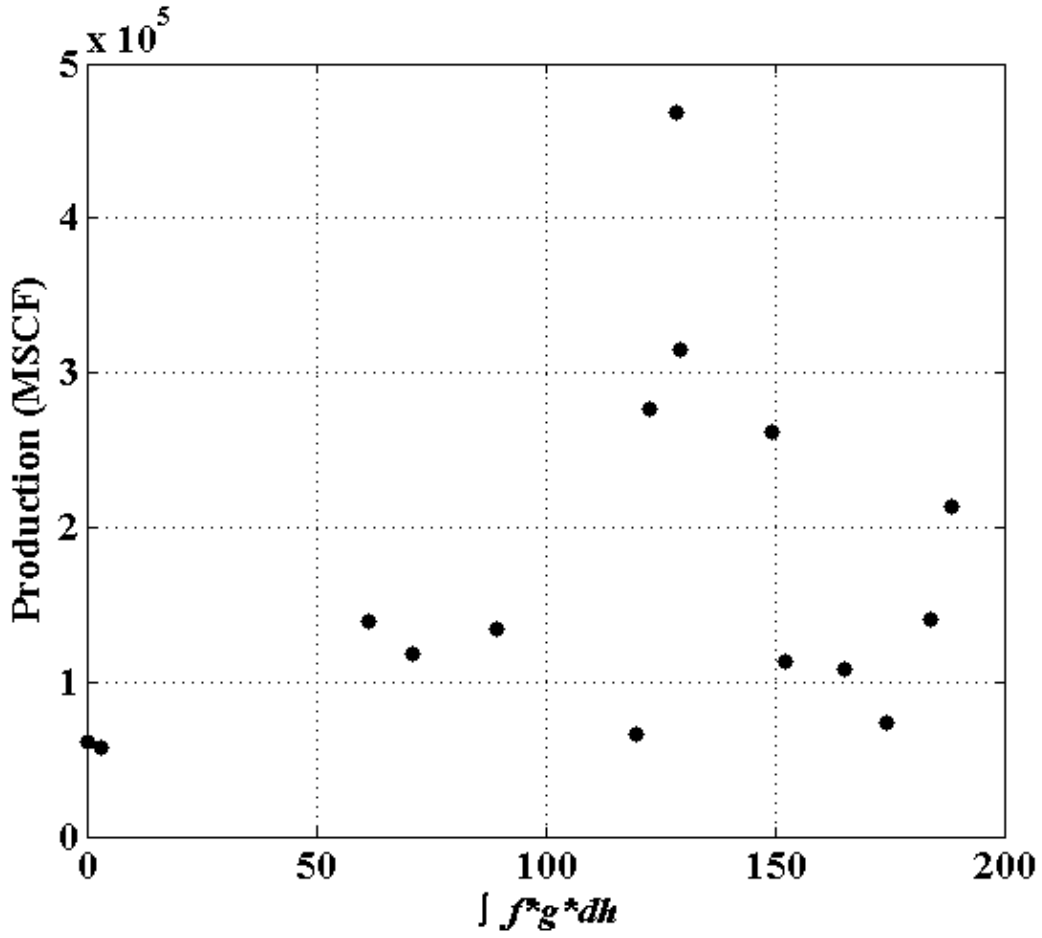

Figure 3.11: Integral of *f**g* along the depth of the well vs production for 15 wells. *g* is the step function used for giving preferential weights for perforated zones and *f* is the function used for defining the weights for zones with optimum gamma ray reading.

Next, a step function was used to model the effect of sonic and neutron porosity:

$$I = 1 \; if \; sphi - nphi \geq 0.05, \tag{3.10}$$

$$I = \; 0 \; if \; sphi - nphi < 0.05,$$

where *I* is the weight decided by the model. The product *f*g*I* was defined as objective function 2. The integral of the objective function was carried out along the borehole for all the wells and is plotted against gas production for 15 months for all the wells in Figure 3.12.

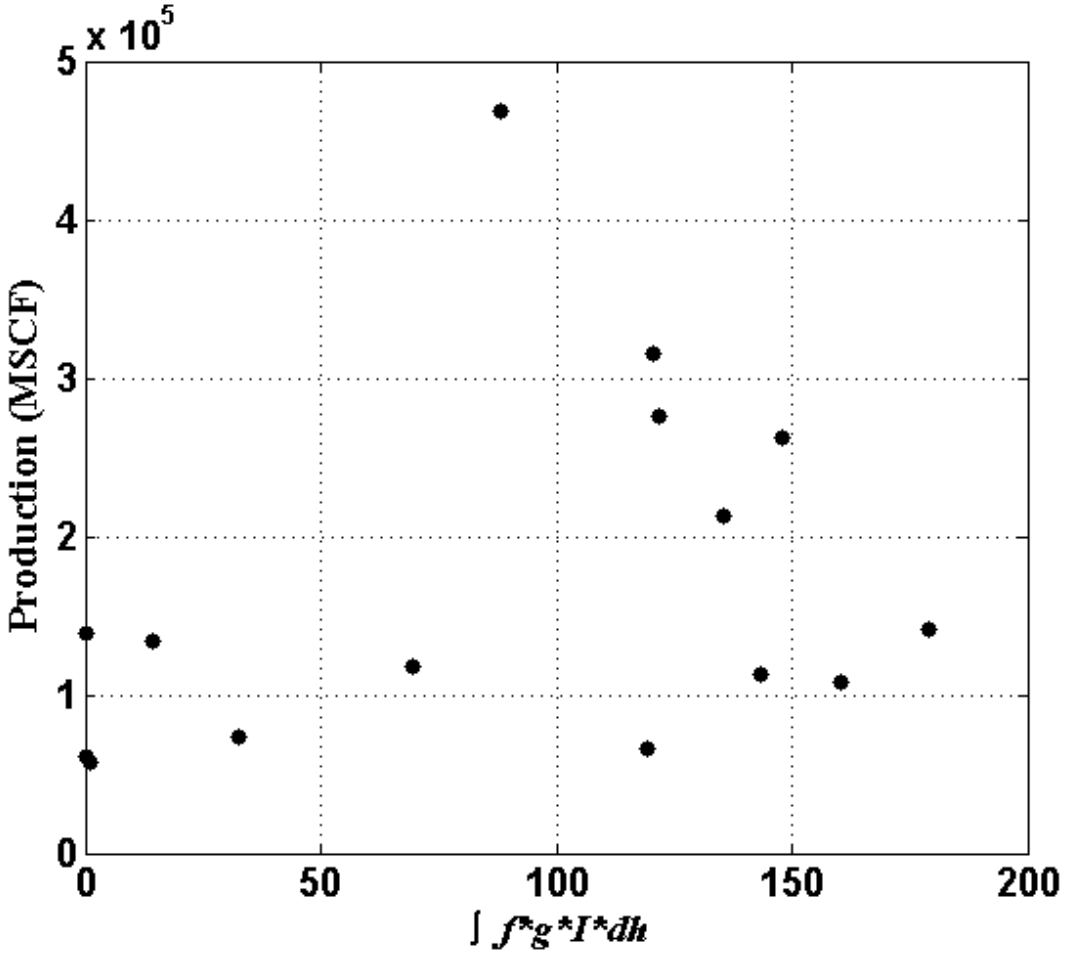

Figure 3.12: Integral of *f*g*I* along the depth of the well vs production for 15 wells. *g* is the step function used for giving preferential weights for perforated zones, *f* is the function used for defining the weights for zones with optimum gamma ray reading and *I* is the step function used for giving preferential weights to zones shoeing sonic neutron crossover.

Including the neutron porosity did not appear to improve the predictive power of the model, and so this effect was not included in further analysis.

Next, we tested including *UCS* in the analysis:

$$h = e^{\frac{-(UCS_h - 50)^2}{10^2}}, \tag{3.11}$$

where UCS_h is the *UCS* reading at particular depth.

The product *f*g*h* was defined as objective function 3. The integral of the objective function was calculated along the borehole for all the wells and is plotted against gas production for 15 months for all the wells in Figure 3.13.

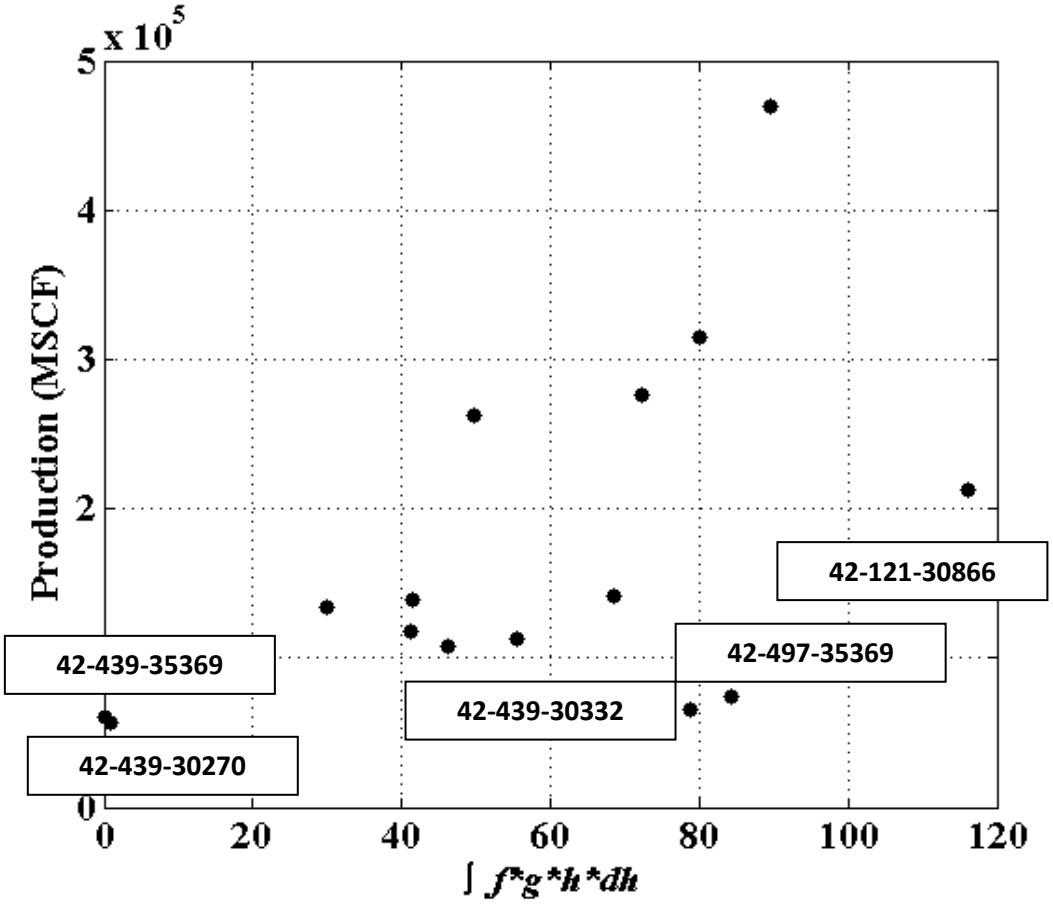

Figure 3.13: Integral of *f*g*h* along the depth of the well vs production for 15 wells. *g* is the step function used for giving preferential weights for perforated zones, *f* is the function used for defining the weights for zones with optimum gamma ray reading and *h* the function used for defining the weights for zones with optimum *UCS* reading.

As an alternative to using the Gaussian equation, we tested using step functions. This function was defined as:

$$X = 1 \; if \; depth \; is \; perforated, \tag{3.12}$$

$$X = \; 0 \; if \; depth \; is \; not \; perforated,$$

$$Y = 1 \; if \; 80 < GR < 110, \tag{3.13}$$

$$Y = 0 \; if \; GR < 80 \; or \; GR > 110,$$

$$Z = 1 \; if \; 45 < UCS < 55 \, , \tag{3.14}$$

$$Z = 0.5 \; if \; 40 < UCS < 45,$$

$$Z = 0.5 \; if \; 55 < UCS < 65,$$

$$Z = 0 \; if \; UCS < 40 \; or \; GR > 65,$$

where *X, Y, Z* is the weights decided by the model based on the perforations, gamma ray reading and *UCS* respectively.

The product *X*Y*Z* was defined as objective function 4. The integral of the objective function was calculated along the borehole for all the wells and is plotted against gas production for 15 months for all the wells in Figure 3.14.

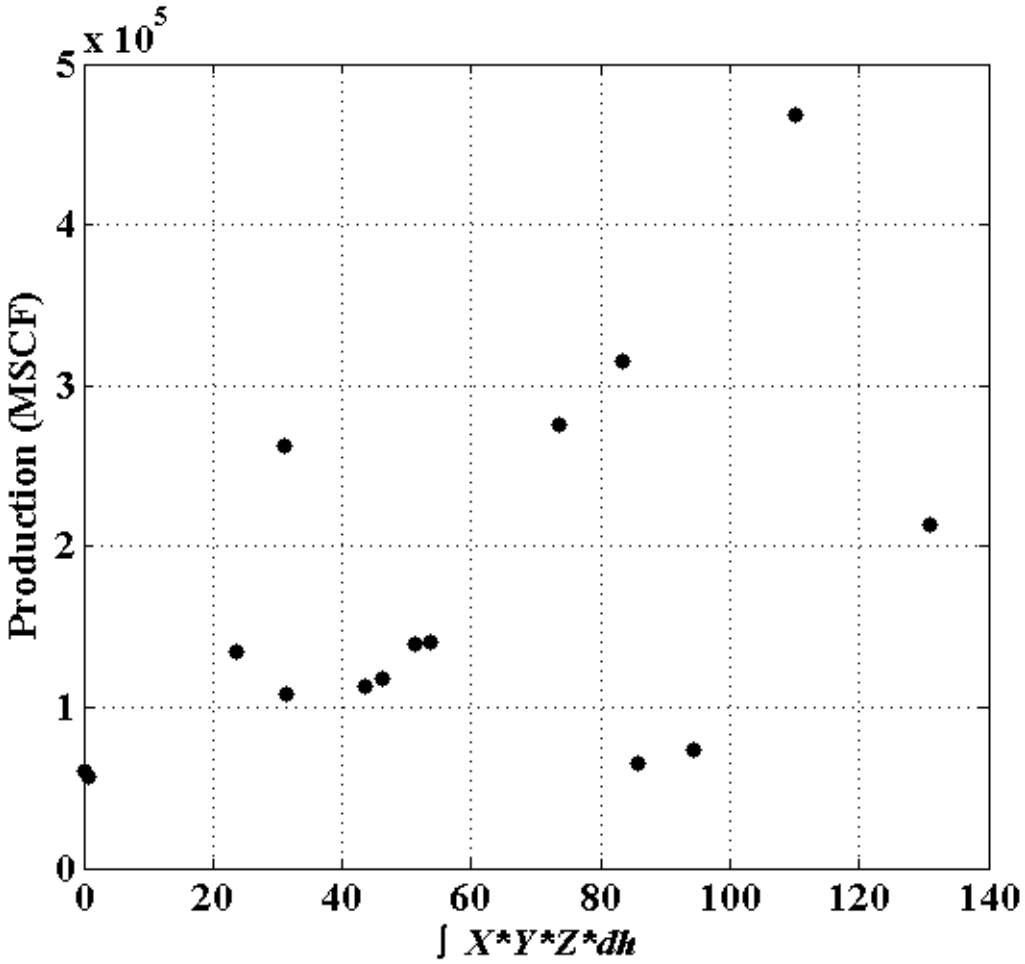

Figure 3.14: Integral of *X*Y*Z* along the depth of the well vs production for 15 wells. *X* - is the step function used for giving preferential weights for perforated zones, *Y* is the step function used for defining the weights for zones with optimum gamma ray reading and *Z* the step function used for defining the weights for zones with optimum *UCS* reading.

3.4 DISCUSSION

The plot in Figure 3.11 is attempt at locating the productive zones in a well based only on the gamma ray reading and the perforation depths. The plot shows a weak correlation between the gas production and objective function 1. Wells 42-121-32178 and

Well 42-439-30270 had the lowest objective function values and were also the lowest producing wells in the data set.

The plot in Figure 3.12 is an attempt at locating the productive zones in wells based on the gamma ray reading and the crossover of sonic and neutron porosity. The plot shows a poor correlation between the productions of gas and objective function 2. We conclude that including crossover did not improve the understanding of productive zones in wells. This was apparently because the presence of clays confounded the neutron porosity measurements.

The plot in Figure 3.13 shows that including *UCS* for the perforated zones improved the correlation with production. Figure 3.13 shows a few outliers. A closer look at the well logs for these wells allows us to hypothesize about why they did not fit the trend.

42-121-30866: Inspecting the log in Figure 3.10 there are streaks of intervals with increased *UCS* values that coincide with low values of gamma ray and high travel times. These streaks have very high *UCS* and contain no organic content. This heterogeneity could vertically segment the stimulated region and decrease production.

42-497-35369: Analysis of Figure E.13 in Appendix E reveals that the well has very high *UCS* in the perforated zone. A significant part of the wells is perforated in the Forestberg Limestone. This could be interpreted from the low values of gamma ray reading and no cross-over between sonic and neutron porosity. This in a nonproductive zone in the well and might have decreased the effectiveness of the fracture treatment.

42-439-30332: The poor performance of the well is inexplicable from our available data. The well log in this well is nearly identical to the nearby 42-439-30331, which was a much better producer.

Figure 3.14 shows production data for wells plotted against a function similar to that used in Figure 3.13 but the transitions are sharper instead of using a continuous expression to decide the weights for zones with optimum readings of the both *UCS* and gamma ray. Figure 3.14 shows the same outliers as Figure 3.13 but does not show any better correlation between production data and the objective function.

3.4.1 Remarks on the Wells Used for the Study

All the wells were vertical. Vertical wells were chosen for the study because logs are not typically available for the horizontal wells or the horizontal laterals of the wells. Most of the wells were drilled from 2001-2004. The wells are drilled by different operators. It was a time when not a lot of operators had experimented with horizontal drilling and slickwater fracturing in the Barnett. The wells may not have been drilled through the entire height of the formation to prevent fractures from migrating into the water bearing Ellenberger formation. The fracture treatments might have been carried out in stages but that information is also not available.

Also there is also no information available about how the operators managed these wells. It is possible that size of choke in the production line might have been changed to manage production or the head pressure might have changed by increasing the pressure downstream. These effects could not be accounted for our study. In general, however, we have to assume that operators did their best to maximize production from

each well. Because the 15 month production correlates well with the 10 year production, we assume that any temporary operational difficulties that affected production must be fairly minimal.

3.5 CONCLUSIONS

The hypothesis generated from the sensitivity study, that shear stimulation plays an important role in fracturing, was studied using field data from the Barnett Shale.

Dependence of fracture shear dilation angle on rock mechanical properties can estimated from the model developed by Barton and Choubey (1977). The fracture dilation angle can be correlated to the formation *UCS*. *UCS* cannot be directly measured from log data, but it can be empirically correlated to other log measurements. The most commonly used property is sonic travel time.

Our results suggest that gamma ray and *UCS* readings may be useful for identifying well productivity in the Barnett Shale. In our study, the thickness of zones with gamma ray reading between 80 GAPI and 110 GAPI and *UCS* between 40 MPa and 60 MPa was correlated with the 15 month production. These specific ranges of optimal properties cannot be directly applied to other unconventional formation, but similar studies could be conducted to find zones with optimal properties. Sonic and neutron porosity crossover did not appear to help predict productive intervals. This was apparently because of the confounding effect of clay on the neutron porosity measurements. Because only 15 wells were used in the study, we cannot rule out that the relationships identified in the study were coincidental.

3.6 SUGGESTIONS FOR FUTURE WORK

A more comprehensive analysis would improve the results by using more wells, more data about the fracture treatment, and more log data.

More wells could be included in the data set to improve the statistics of the study. Wells from different shale formations could also help in better predicting the trends of Figures 3.11 to 3.14. Similar analysis could be conducted on the lateral section of horizontal wells if LWD data is available for these sections. Operational information could be used to identify the effect of operational practices on long term production in wells and correct for anomalies in production data.

The results could be validated by including additional logs in the analysis. Availability of more logs for wells would help in better identifying productive zones. Particularly, the spectral gamma ray data could help in quantifying the uranium content in the formation and correlate it to the kerogen content of the formation. Resistivity logs could be used in conjunction with sonic logs using a modified Passey et al. (1990) $\Delta \log R$ method to do a better analysis for organic content in the wells. Resistivity logs could also be calibrated using core studies to better quantity the water saturation in shale that can give a better idea of the gas content in a particular zone (Kale et al., 2010). Finally, flow meter logs could be used to establish if the zones selected for analysis do actually show greater production than the other zones in the well.

Chapter 4: Conclusions

The sensitivity study carried out in our research shows that that geomechanical properties related to unpropped fracture conductivity play a critical role in defining the success of fracture stimulation. The unpropped fracture conductivity cannot be directly measured in the field, but it can be correlated to the *UCS* of the rock, which can be measured with well logs.

To test the practical usefulness of this concept, we performed a comparative study using production data and gamma ray, sonic, and neutron logs from 15 vertical wells in the Barnett Shale. The study found that production could be correlated to gamma ray and *UCS* values (estimated from the sonic log) within a certain range, neither too high, nor too low.

A more comprehensive sensitivity study could be carried out using both the formation geomechanical properties and the design parameters of the fracture treatment. Research should also focus on understanding the basic physics of interaction of hydraulic fractures with existing natural fractures. The comparative field analysis could be improved by using more wells, more data about the fracture treatment, and more log data.

Appendix A: Simulation settings used in the study

Table A.1: Settings in Matrix A.

G (GPa)	v	σ_{yy} (MPa)	$\log(e_0^3/12)$	φ_{edil}	μ	K_{Ic} (MPa.m$^{0.5}$)	$\sigma_{n,eref}$ (MPa)
14371.72	0.250315	29.48638	-13.1873	2.587642	0.569639	6.322528	30.70621
18030.71	0.283895	34.01739	-14.1501	3.940012	0.531189	2.242009	50.86862
7818.948	0.292047	26.52191	-13.5994	2.404343	0.53802	7.732501	33.69292
24148.68	0.198888	31.97788	-14.6886	2.57178	0.577405	4.177487	84.65407
10314.12	0.279387	31.54302	-15.2713	1.035763	0.439225	4.07713	87.92867
16652.1	0.27125	33.813	-15.461	0.828202	0.481809	3.039587	56.66705
6872.978	0.210594	33.13317	-13.8486	2.604559	0.453215	3.138665	62.37316
20543.58	0.234787	27.73473	-13.0462	3.446038	0.476633	5.971991	43.42925
13103.84	0.299898	35.18354	-15.0834	3.189956	0.481358	3.074931	38.14359
19259.65	0.222524	30.82097	-12.9321	1.560746	0.435157	3.566086	40.64456
9088.537	0.267963	24.12416	-15	0.152679	0.412886	4.572386	48.53408
22915.73	0.344909	24.16565	-14.1915	1.891632	0.407576	2.078559	79.29973
11583.35	0.162396	23.93669	-15.8671	2.609473	0.402129	4.317265	45.26869
15423.12	0.278546	27.75841	-14.3087	1.4484	0.57009	6.358596	82.17847
5603.617	0.193073	26.61208	-13.247	1.591903	0.424552	6.888378	82.31573
21776.16	0.263023	31.51231	-12.9374	3.551632	0.447884	1.558749	23.68325
14951.71	0.281908	24.71392	-14.6383	1.908033	0.412566	4.354229	36.43278
18184.44	0.260646	24.45787	-15.177	0.483993	0.452133	3.635128	23.26682
8476.812	0.165666	35.79145	-12.9976	0.7976	0.582632	6.040016	78.8919
24501.86	0.185351	27.39063	-14.6989	1.648223	0.575446	3.54612	45.7195
10983.5	0.273697	31.44914	-14.5898	3.713021	0.498935	2.851771	21.07593
17128.43	0.173846	27.47895	-15.3818	1.124996	0.56078	6.836544	88.55317
7455.742	0.312078	33.23018	-13.3131	0.97595	0.594237	7.668344	59.63327
20930.07	0.342893	29.0199	-15.3835	3.780808	0.401237	2.807106	56.21751
13684.66	0.236913	32.99303	-14.1501	2.618512	0.59586	2.722125	22.37997
19415.21	0.181153	32.49324	-15.7718	3.932728	0.489229	5.22802	68.11645
9746.649	0.298673	30.38629	-13.5514	3.347881	0.569752	6.573129	51.55403
23267.56	0.311262	31.41169	-14.3795	1.66737	0.423097	8.270966	89.89326
12253.41	0.202111	29.67495	-13.1334	0.59094	0.493435	1.822209	51.23699
15895.82	0.180197	24.76368	-13.6309	3.033267	0.511341	4.49585	82.75808
6186.16	0.271092	34.78941	-13.0004	2.05346	0.476555	5.189096	28.59427
22147.89	0.215814	32.26842	-14.0969	3.14688	0.484531	4.935174	32.34705
13854.12	0.293488	31.58179	-13.9148	0.947098	0.498634	2.438221	26.06359
17524.73	0.239374	29.70251	-14.0839	0.172516	0.414235	5.131607	70.19293
7516.059	0.256839	29.29923	-14.8523	3.569038	0.404023	5.988696	27.16385
23830.64	0.234216	32.53205	-13.2606	1.181664	0.450017	8.368584	25.44477

10206.77	0.244903	26.51127	-13.2538	0.485902	0.458842	6.855002	52.82369
16537.18	0.158138	30.00809	-15.6291	2.349278	0.452569	8.079128	87.73793
6432.341	0.217026	32.00663	-13.8166	0.538627	0.454525	5.804547	22.53424
20269.51	0.170585	28.10843	-15.0184	2.318779	0.566181	6.294861	79.24792
12585.92	0.263236	36.05283	-13.9787	2.083007	0.524486	7.36079	85.72569
18755.02	0.233247	31.55909	-13.2268	1.896585	0.40554	2.141989	55.44679
8788.362	0.241349	28.87995	-14.9742	3.432437	0.470689	1.60475	38.29093
22597.78	0.173865	31.87194	-14.9489	0.016342	0.511721	8.865814	69.61466
11476.3	0.332025	36.83042	-15.5276	0.376949	0.561056	3.943588	68.24932
15302.88	0.212075	25.13648	-15.2194	2.479714	0.584379	8.253545	45.95305
5216.057	0.303621	36.89981	-14.9742	2.456955	0.596613	7.400927	48.89063
21530.67	0.169564	27.63558	-15.5835	0.900698	0.468034	5.829848	83.59318
14512.51	0.191652	36.27301	-13.6083	2.567974	0.552156	7.282855	27.7031
18501.9	0.270005	26.34789	-13.5643	1.794291	0.457887	7.03066	43.03361
8176.231	0.21885	36.16914	-14.2859	2.247471	0.518525	5.403837	42.11183
24923.61	0.340806	28.31144	-14.7625	2.4746	0.466606	2.65562	61.96763
10797.97	0.282496	29.19684	-15.3204	1.822542	0.570121	6.502253	33.91622
17400.87	0.190869	28.72895	-13.8114	0.624189	0.543424	4.1513	54.08161
7089.975	0.332329	26.24822	-13.3903	0.553217	0.496826	3.807174	39.5348
21049.22	0.169179	28.14086	-14.7409	1.131636	0.402734	5.395711	24.84327
13245.52	0.15383	28.02947	-13.0786	0.350784	0.513405	5.088444	33.85589
19732.4	0.210087	26.67266	-14.2709	2.208157	0.465237	8.747491	25.56927
9446.565	0.220144	32.68367	-15.361	1.996006	0.528179	2.827851	51.05528
23693.01	0.308107	25.76614	-13.8378	2.586808	0.51474	1.777123	48.56221
12067.37	0.268564	25.00264	-13.2954	1.241521	0.423724	5.38849	73.57163
16104.82	0.263326	30.574	-15.1044	3.79695	0.431626	3.451517	68.05155
5782.471	0.17093	33.3386	-13.64	1.726019	0.421096	5.348205	75.56621
22340.2	0.260607	29.94584	-15.9057	3.482291	0.597548	5.574903	76.15889
14174.3	0.280356	34.15487	-15.6941	0.41175	0.524542	7.455634	31.41893
17832.15	0.160586	29.61577	-14.0647	3.529851	0.453441	1.93118	61.23645
8015.041	0.180538	34.6765	-13.3457	3.743476	0.489576	5.257014	48.38043
24341.05	0.206692	34.782	-15.8445	2.488335	0.4839	8.86406	78.87332
10553.51	0.261549	37.89351	-14.7844	2.358004	0.587885	7.09406	73.0087
16731.08	0.328657	26.11077	-14.7625	1.192336	0.428922	3.55187	34.84529
6637.164	0.189119	25.88232	-13.0491	3.499965	0.407566	3.533646	31.66047
20466.62	0.238572	29.09197	-14.0839	0.328008	0.476547	1.624339	66.71988
12900.93	0.18421	30.92891	-13.026	3.574867	0.409213	1.611849	80.84896
19062.75	0.243071	24.86199	-13.5471	0.542587	0.424289	5.680895	85.58819
9286.792	0.232479	32.56537	-14.1166	1.116233	0.406514	3.47326	67.34974
23110.88	0.327199	27.54559	-15.2973	1.906773	0.471804	7.491532	51.52584
11840.8	0.171752	33.4908	-15.857	0.005426	0.412394	6.689161	27.94213

15533.85	0.215254	27.22052	-13.4288	0.628477	0.427292	3.762576	45.50887
5342.902	0.240305	31.1537	-14.5994	1.103627	0.572032	6.456729	61.39048
21656.71	0.239709	30.04311	-14.498	2.129148	0.447311	7.125184	77.56897
14842.34	0.270728	25.41755	-15.6699	1.404108	0.426338	8.637793	65.94849
18308.47	0.192638	34.30931	-12.959	1.13023	0.577542	3.889894	46.70792
8595.23	0.190606	27.17323	-13.1241	0.971703	0.597015	7.785487	49.19565
24570.94	0.167963	28.90299	-15.221	0.127636	0.416369	1.665436	37.89731
11211.73	0.17741	28.57843	-14.4459	1.756094	0.511666	4.926611	36.77336
16885.39	0.205473	26.46159	-14.9489	2.368358	0.493708	2.211772	66.7329
7217.781	0.241328	34.34507	-14.429	3.955288	0.532203	8.379227	48.23457
20741.05	0.210806	26.52219	-13.1272	2.614552	0.525337	3.080155	85.12629
13569.95	0.315663	25.79131	-14.9241	3.769143	0.471315	2.928814	47.04785
19538.99	0.166991	29.58987	-14.5616	3.38184	0.452801	8.471019	36.37782
9866.7	0.159572	30.88205	-15.1695	1.367414	0.460296	3.604052	24.29831
23287.71	0.218345	34.89296	-13.6773	2.272799	0.551123	8.355392	89.05348
12446.02	0.328589	24.76565	-14.4459	1.355883	0.562156	8.82525	20.78999
15680.1	0.317508	28.96571	-13.8539	0.638019	0.557479	3.486372	75.23887
5985.851	0.238595	27.24998	-14.3958	0.226069	0.508938	6.897831	63.32859
22023.29	0.183596	34.46311	-13.6963	0.59098	0.563957	2.641204	20.16294
14047.73	0.201547	25.31229	-15.2826	2.582301	0.465596	8.766639	74.10603
17718.03	0.330036	33.67547	-15.4047	0.561044	0.48892	3.782165	31.82833
7751.666	0.266483	30.57803	-15.3304	0.689387	0.40531	1.66622	82.68594
23912.88	0.26564	34.14975	-14.9118	2.26464	0.531596	8.084534	40.63253

Appendix B: Simulation Settings used in the study

Table B.1: Settings in Matrix B.

G (GPa)	v	σ_{yy} (MPa)	$Log(e_0^3/12)$	φ_{edil}	μ	K_{Ic} ($MPa.m^{0.5}$)	$\sigma_{n,eref}$ (MPa)
7313.035	0.212617	31.85593934	-14.8203	3.00359	0.490392	7.050322	77.3084
12402.11	0.294809	43.38890894	-15.9956	3.864013	0.432142	7.161038	33.5217
8602.768	0.329569	25.31075958	-15.2892	1.16517	0.416485	5.163438	27.64468
24850.22	0.237606	36.19459402	-14.226	2.593895	0.442918	3.05965	68.58646
9275.832	0.206784	45.2446443	-15.8996	0.846692	0.4467	1.869719	75.66655
9484.031	0.265274	38.77553022	-15.7169	1.763922	0.4354	2.60561	20.82799
19866.59	0.317856	38.27509058	-16.8246	1.752642	0.502807	2.083415	58.30378
7647.138	0.255997	35.00674778	-14.4104	3.089244	0.463044	8.012052	31.66485
18893.35	0.343446	36.2043289	-15.0393	2.741499	0.48081	3.38327	84.24646
5428.756	0.155631	45.1602992	-14.1965	0.579289	0.53681	6.843665	67.99636
24182.59	0.278351	30.3604184	-16.6278	2.230845	0.586211	7.175518	85.69173
16399.04	0.32317	41.46290588	-16.2347	0.806739	0.478559	2.393032	35.17647
15880.72	0.284637	45.9074751	-16.7645	2.224076	0.562854	2.325515	26.32215
16653.95	0.190793	34.45608284	-15.6852	0.494781	0.444982	7.843664	35.42324
13976.24	0.300138	36.57695052	-14.8734	3.055075	0.557703	2.478585	29.03393
22581.07	0.275077	37.80714826	-16.1067	3.061974	0.564009	4.920581	38.35812
20979.49	0.18154	38.26001106	-14.3569	1.092417	0.594435	6.989691	36.95292
14558.42	0.262404	41.70778106	-14.9574	1.086064	0.528085	2.163736	39.87752
16984.16	0.194372	36.07324206	-16.8392	2.803812	0.511501	7.801622	72.7372
22957.84	0.160071	43.92659404	-16.5251	0.275314	0.539802	8.405905	89.40308
24559.89	0.202212	24.1028948	-15.5748	3.267915	0.503846	5.222101	21.23393
13204.34	0.292039	46.4749852	-15.6216	1.025362	0.591237	4.410797	59.07134
7575.78	0.232953	28.62104826	-14.0677	2.702556	0.59382	5.729972	49.67635
11045.33	0.292861	24.40801648	-15.2158	0.92822	0.543836	7.503648	89.47958
17770.08	0.254558	38.9627835	-16.1041	3.254512	0.533206	5.723173	71.35433
20598.14	0.233679	40.87072454	-14.2848	3.967126	0.456447	1.678072	60.53232
7859.889	0.322024	36.8110887	-16.1998	0.173268	0.478937	7.349731	27.74646
20510.62	0.151236	43.5252927	-16.5395	2.225622	0.598311	7.929484	34.45772
15554.38	0.306588	41.15881018	-15.34	3.01464	0.553484	2.666488	30.5611
17514.59	0.315183	29.35953912	-15.0971	0.025518	0.422999	6.55231	72.77871
9675.273	0.204686	42.85277474	-14.6357	3.016575	0.531629	4.451654	53.3191
9410.847	0.290553	41.69270154	-16.463	3.656925	0.462658	3.568286	60.5757
16619.24	0.245225	45.9116506	-16.2881	0.007924	0.41111	4.158813	49.13452
19958.64	0.303562	34.5829226	-14.5972	3.576872	0.49081	1.517652	64.23979
20468.85	0.151306	28.85303904	-14.5273	0.021019	0.482727	8.873868	54.55345
13957.85	0.338289	31.82050724	-15.1783	2.17578	0.52624	1.89874	36.18316

12645.92	0.1698	38.55730666	-16.7611	1.72875	0.441044	3.633259	85.24937
13937.1	0.255136	47.65226146	-14.4497	1.88855	0.463876	7.787322	88.27953
9976.516	0.346708	25.227178	-14.7137	0.886788	0.421429	8.884445	52.43297
16695.62	0.262257	44.8489262	-15.4419	3.887441	0.471616	6.636226	34.2508
19856.97	0.191797	42.00650826	-15.6384	3.391807	0.43279	1.958161	56.62222
20935.86	0.161818	45.07127754	-15.5229	2.802612	0.472076	3.313843	65.31679
5540.719	0.17978	43.96221702	-16.2059	0.110905	0.581812	3.879401	26.51817
21574.83	0.240518	46.65066638	-14.6039	3.770374	0.437673	1.825388	47.86235
14000.92	0.243445	31.22145422	-15.8674	1.080454	0.409396	7.875983	80.58461
22566.77	0.168481	31.61273436	-15.1963	1.083442	0.415786	5.602056	72.4271
23358.76	0.176517	42.26861036	-15.7167	2.451386	0.405465	8.578953	51.73033
5907.152	0.234154	43.59975976	-15.8968	0.914374	0.410006	6.066704	56.0498
5784.733	0.303978	30.30472916	-14.6555	3.443128	0.491969	7.865996	57.7668
13047.78	0.28945	42.6076371	-14.8255	2.650041	0.542666	1.745688	42.1437
21611.67	0.240534	25.71640344	-16.3409	1.974916	0.528158	2.785308	32.96245
5320.892	0.238446	34.83753266	-14.9348	0.035051	0.587435	2.733259	49.91664
14023.26	0.233648	41.3619065	-14.0074	0.275299	0.594847	5.974907	72.39152
6335.383	0.168771	30.93904726	-14.3217	2.696162	0.40885	6.366031	73.04959
21674.42	0.199759	24.8542462	-14.1136	3.256395	0.592461	7.247241	49.86132
22805.66	0.231202	31.35852992	-15.345	3.09449	0.562654	6.246997	49.87789
22974.98	0.157634	28.7665704	-16.9568	3.009612	0.427761	7.234867	42.56071
9957.448	0.26462	42.68706704	-16.0401	3.573045	0.457464	5.399891	82.78786
5976.786	0.285026	34.29288044	-14.3173	0.583947	0.429988	4.702236	85.41584
15169.22	0.182659	40.95745564	-15.2293	3.361338	0.476757	1.634931	39.17591
24164.6	0.190559	35.18374126	-14.463	3.07037	0.491171	6.839038	60.69483
5107.776	0.321998	45.60972616	-15.1756	1.290216	0.423513	2.393354	80.42292
24097.26	0.178233	28.85124954	-14.6618	1.570385	0.55846	4.260911	32.67109
20596.26	0.287682	47.65889454	-14.3114	1.99855	0.413383	3.564734	49.39019
7603.628	0.167457	38.9640958	-15.0052	0.529868	0.46644	1.519579	66.19169
9940.73	0.261119	29.75069996	-14.5852	2.751244	0.547597	7.242377	57.07287
15832.34	0.309907	36.59577606	-14.4233	1.374029	0.506279	7.534246	68.53488
23654.39	0.29165	34.46412366	-15.4364	3.665506	0.402243	2.033987	52.47217
21363.89	0.199652	31.1891955	-15.4998	0.592067	0.423625	2.799384	81.53552
5290.072	0.233054	34.06988488	-16.8161	3.30766	0.555265	4.970637	60.25589
15359.21	0.186795	31.9842107	-15.7318	3.304682	0.481559	3.379106	27.70172
17743.09	0.277513	29.11280286	-14.859	2.046453	0.569893	5.321458	25.46432
10342.22	0.273996	45.74634852	-16.0912	2.522876	0.501637	7.602943	40.63539
24029.01	0.269374	28.13998294	-15.6223	0.058194	0.592698	8.723433	31.63008
15249.32	0.303367	46.60041722	-14.9158	2.97465	0.558285	3.689733	20.01512
11501.55	0.213834	35.0659683	-14.6026	1.295948	0.582362	1.574369	66.56451
24159.38	0.331464	44.88285512	-14.2776	2.437518	0.57436	7.363512	83.21983

5462.67	0.325982	28.28803424	-15.3213	3.707993	0.433157	3.841509	87.54201
7541.069	0.155608	36.45643366	-16.4274	1.946725	0.565671	4.772132	50.39675
11170.69	0.33098	30.32763476	-16.7891	0.661228	0.504514	7.36016	49.14701
15690.77	0.322828	32.61826634	-16.1921	3.649359	0.41818	3.409286	25.32949
11908.54	0.32494	29.43660692	-14.5981	2.341086	0.472379	3.402098	42.27074
16387.2	0.349958	36.28099108	-15.5952	1.729588	0.435166	5.022214	74.18472
15899.18	0.304036	27.60222626	-15.419	1.284829	0.502014	4.466189	56.12537
16896.82	0.295603	25.07958004	-14.0387	0.616073	0.4997	4.591148	70.81755
19956.29	0.27607	37.23982904	-14.522	3.595731	0.530153	8.124979	45.77537
6556.467	0.314821	43.71774746	-14.3775	1.154228	0.496098	6.364127	79.83645
13698.03	0.330324	35.9102544	-14.0588	3.67491	0.455699	6.030912	83.39866
15097.69	0.31707	27.46061716	-16.4517	0.001932	0.467062	7.313339	64.30971
15310.65	0.273818	34.4834264	-16.2173	1.273458	0.531168	8.893597	71.05786
9809.382	0.21897	31.7811621	-15.7498	0.031248	0.445213	5.396786	89.25855
8720.068	0.33525	46.98981242	-14.4447	3.965967	0.449213	3.687798	87.57033
14717.02	0.299884	32.40684288	-16.6629	3.151976	0.459204	3.561203	83.12083
13300.24	0.246407	30.25887024	-15.5242	1.031422	0.546129	8.518364	45.38469
22249.36	0.242683	25.20090814	-15.0576	2.38967	0.465635	6.725557	47.91296
6525.342	0.277298	25.38861476	-16.9023	1.939551	0.555862	4.941991	66.97523
21962.99	0.310601	23.90385468	-14.3922	3.665541	0.507403	7.275641	46.90159
10843.71	0.285662	26.62606594	-16.5336	3.670472	0.513512	5.733648	20.07769
10390.31	0.179054	35.26035572	-14.8286	1.095179	0.575098	6.407979	39.42983
6655.556	0.24521	35.93932	-15.6622	2.232865	0.594595	8.259002	47.49684

Appendix C: Stimulated Reservoir Volume

Table C.1: SRV/100 (m^3) values obtained from all simulations settings.

Results from setting in Mat A	Results from setting in Mat B	Results from setting in Mat C1	Results from setting in Mat C2	Results from setting in Mat C3	Results from setting in Mat C4	Results from setting in Mat C5	Results from setting in Mat C6	Results from setting in Mat C7	Results from setting in Mat C8
25996	24956	23675	23375	27293	27964	29043	26962	29238	21459
53576	35127	32430	36067	35876	35353	33924	32768	41239	33727
18937	17758	15388	17389	15623	16122	15703	16552	14838	19165
29339	36713	31343	39279	38598	25326	36367	37372	37749	28726
22198	22635	31611	33084	27934	24684	31078	38271	33462	30109
23593	27976	21844	22006	27462	19182	15668	28137	21444	40569
40511	19918	24285	28001	26449	27100	30551	22472	26165	24134
30853	25234	19835	29256	25195	29075	35432	30192	30403	31109
44994	29970	33335	38839	52066	25624	32482	31022	31650	23339
36014	32106	29237	23805	34872	55343	30217	23823	27966	27239
17681	18833	18611	17830	19301	16306	16350	22191	19613	14899
16034	21167	15732	14923	17556	19293	28745	17266	23943	22945
17593	18263	24792	24746	23510	23041	21564	32809	28524	30315
10844	17544	12570	16037	16583	12659	17672	13948	16893	17914
25812	41708	25366	32358	24832	38014	28070	33588	34763	43077
41473	33439	26983	29890	31586	33431	32421	25514	32893	21716
18770	27612	20502	26182	11945	16252	31595	23756	28666	22809
21903	35554	23980	30432	21460	26230	19350	28088	24581	25370
34372	20571	27640	25368	34967	36334	10694	31546	25280	30191
20743	12351	16115	14658	15050	17103	29819	16700	15208	16978
40773	24507	18923	22038	30746	16020	21697	20656	18888	22349
16471	16861	26342	23107	14774	22925	31536	23813	25486	22633
26167	21924	21630	23560	41766	21588	17828	24647	23171	16787
27705	16720	16188	15543	27373	18973	15414	15511	16325	13420
25811	42237	37918	34198	39314	31425	32351	30071	44268	31146
27208	53990	55046	44165	57612	40370	49461	52296	49286	45974
33015	9782	13170	12466	9309	12348	27767	10789	10735	10020
27003	24416	23892	25062	23992	29957	24068	28801	15859	29791
25809	38533	30669	33645	31868	35887	16376	38282	31610	34020
17159	12909	16548	15178	18070	12560	15698	13381	16471	17920
33800	52429	34626	42721	51501	38746	37056	45349	40230	34997

32053	42315	40910	39533	44071	40652	41201	45704	30562	28250
19736	11134	12314	10223	17704	15974	26307	13346	11821	9941
16176	33779	41816	26715	32194	32595	18065	30993	31762	38160
25085	15196	14431	13488	17165	17254	18779	18694	12402	15611
22203	19246	16114	20696	39198	20257	15768	22682	18737	20096
18001	26058	21781	29526	15191	42162	15466	28630	22003	27448
17918	53706	45713	61582	35061	33277	44477	63069	50680	52799
17169	13887	11207	13949	25089	15933	14808	15761	15151	12589
23620	42231	36463	37309	22854	36290	30296	34557	38921	48884
51521	35340	36667	41214	49321	41305	36534	54079	39800	54073
45777	39327	51325	43966	35206	59352	37131	42945	35321	42900
33433	11311	10938	8740	9725	9891	18916	11724	8388	9888
15096	53017	55766	51215	44290	53823	18818	55700	46810	59859
19372	17965	17729	17178	31744	13844	16789	15251	17282	15410
19893	19427	15237	16196	17387	18531	15773	15974	20914	18268
31578	34690	27402	28499	31119	32945	30278	26404	34034	33499
16005	20844	22036	21906	12140	26739	26666	24742	22107	28440
26416	20104	26896	18427	47894	21925	17253	23581	17372	22528
17931	44060	42670	35510	18710	42567	44361	57539	41797	39057
31549	14048	14841	16195	31079	22196	19093	16850	20179	19137
16824	13981	12918	11544	14687	8298	33199	12891	11185	12256
21032	34096	26805	26451	22236	14207	45102	26850	30889	16370
20826	17705	24455	28895	22829	18742	16688	29345	26722	22292
14648	15295	12348	13563	19418	15026	18628	18785	15446	19807
15900	20013	22154	18152	22735	23558	17089	19238	15631	22626
15795	15233	13071	16360	18786	14711	13906	19381	21632	22839
11445	32909	38039	24104	20287	29858	28142	49341	26689	32859
27494	16619	19318	27343	27162	11778	33344	23398	18654	21082
19183	40813	39920	46274	18933	41282	30385	43369	34409	44426
17465	31090	30883	28074	14567	41052	31297	28103	24315	36931
42683	34996	30934	42587	36178	32858	43737	44331	37734	45305
42343	15900	15263	20926	34819	21645	18129	19882	17327	15836
19472	45661	43773	48477	26358	36665	67550	50513	42175	51143
10378	26342	19638	18685	28599	24541	23024	27928	23681	21855
34673	18409	17334	16984	29552	13904	17243	21259	25531	18500
31423	27842	30679	32537	36086	29252	29733	31012	33407	27115
37436	21341	23489	32087	38433	16138	17308	26322	28276	27999
38576	19289	16740	19148	24780	16796	19749	14236	13065	11345
17482	22487	30768	27316	20522	17882	20498	17370	30328	18906
18690	19847	31466	27344	21265	28412	20077	17361	19046	20493
22199	19237	13573	17891	26210	20272	18515	17774	19543	18955

68025	22714	34185	33994	32192	41958	38051	29838	34839	33674
16323	19221	17373	14965	13522	13339	15387	16303	15696	16809
39729	34426	33731	36770	33664	35404	23241	34910	42961	49506
19534	34715	26564	31161	26193	20992	35712	31809	21737	26728
9425	42879	53111	39042	65509	35665	20477	44465	49402	36032
19026	14716	16198	16400	29538	14916	14133	10830	14569	14045
27021	20973	31960	21398	25084	26240	12817	29879	23482	22589
25199	14274	14145	15293	10198	16047	19250	10529	12007	16228
20628	16388	20378	21034	18075	16733	12497	26713	20327	28237
35379	18317	17122	16649	44630	23752	13438	19103	21473	23028
14662	21532	22913	27756	17613	29388	17904	18908	19116	24363
14622	18290	18552	14810	20229	20441	12410	18914	20706	16632
24840	14111	12372	14660	23979	20699	15262	15809	16286	16447
16796	37920	46600	29845	20676	30793	32021	24701	41169	38842
31617	36435	40218	42302	44001	33323	48298	31465	43198	36364
20220	40517	43498	37392	17289	40583	42467	49431	45220	37371
18782	16068	14664	15227	17095	15715	13853	19732	18954	16238
18737	21456	17537	16285	22859	18956	25838	22124	23656	19067
23719	12123	12761	11762	15688	14049	17057	15031	12930	13933
43076	56099	76328	64586	56029	50292	62921	62076	60639	68147
17622	18864	19592	19393	17304	25922	15495	21908	17465	20558
15648	16505	14013	15587	17366	17249	16220	19608	16995	15021
11419	19293	13155	15450	22491	18947	17998	18097	18661	18631
16632	13339	20612	10932	28347	13781	17712	15325	14738	15234
16825	17782	18962	17121	17338	21713	18996	15634	17241	19108
16297	17506	22906	25400	34212	17953	18515	17911	19385	15691
25829	18878	22062	23314	21056	18212	20895	18661	26845	28329
25398	25570	21090	21698	22536	20522	27168	31508	30080	21155

Appendix D: Monthly production for the 15 wells used in the analysis.

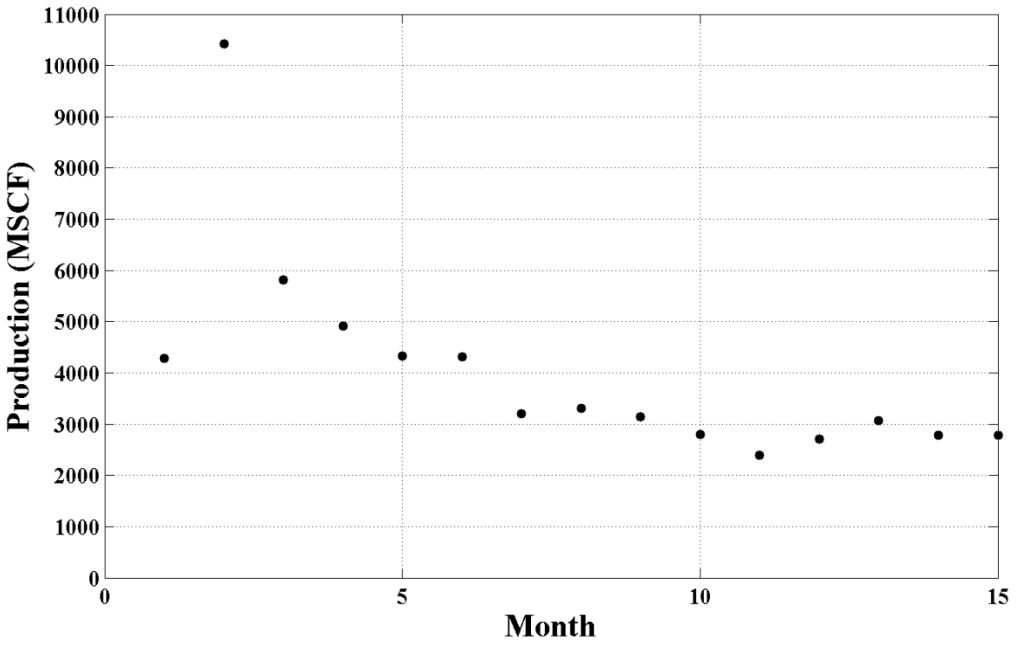

Figure D.1: Production data for well 42-439-30270.

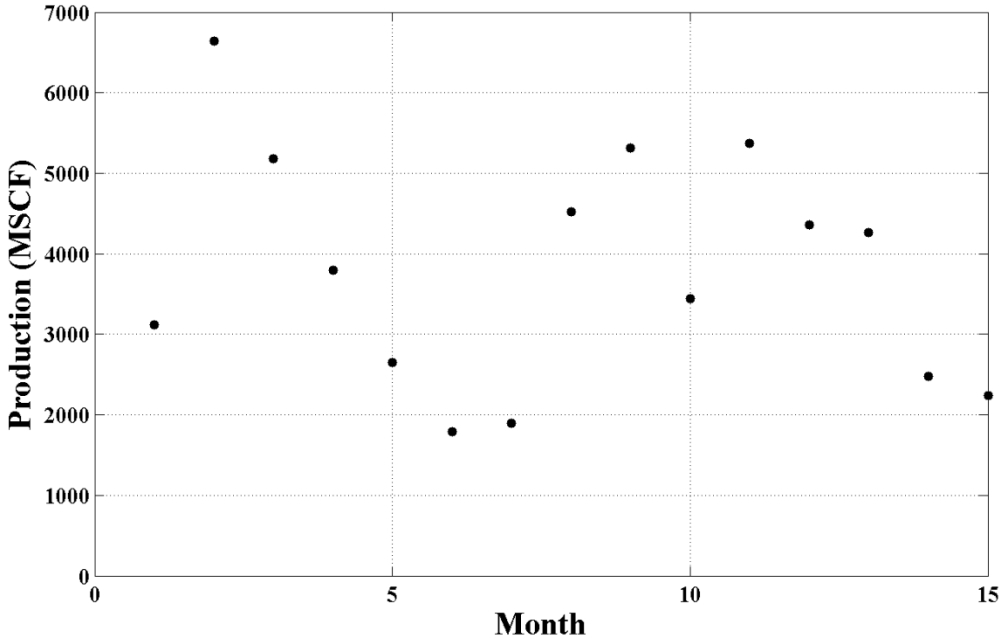

Figure D.2: Production data for well 42-121-32178.

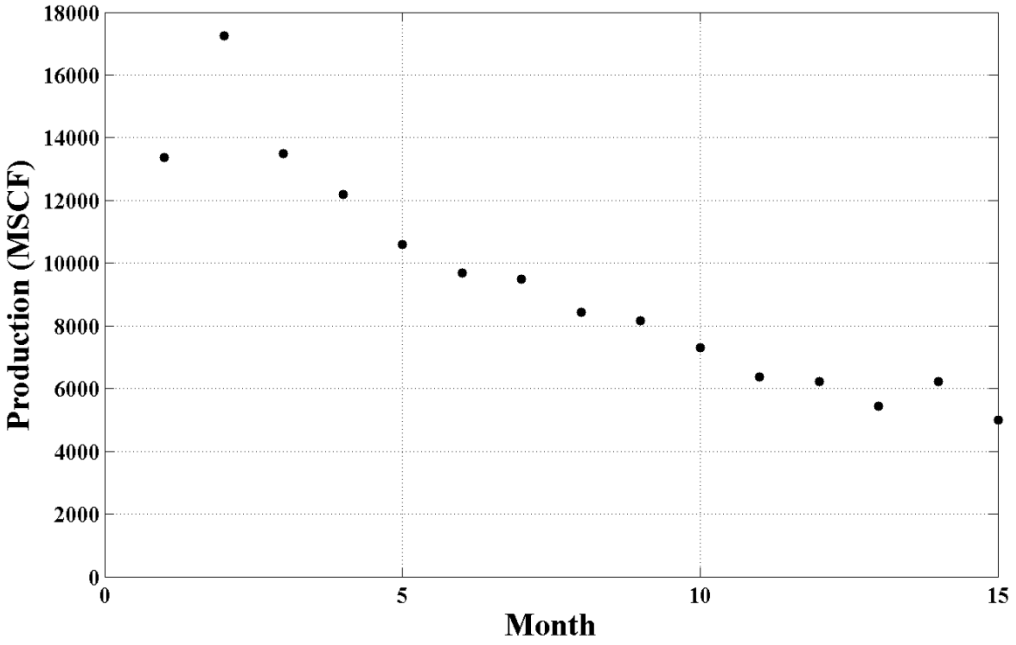

Figure D. 3: Production data for well 42-497-34814.

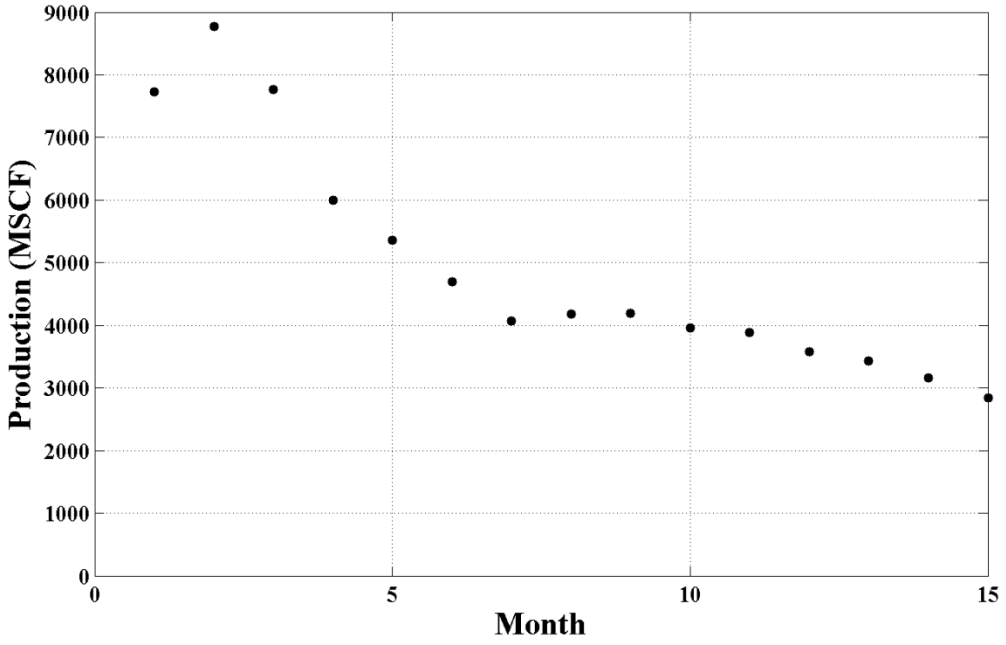

Figure D.4: Production data for well 42-497-35369.

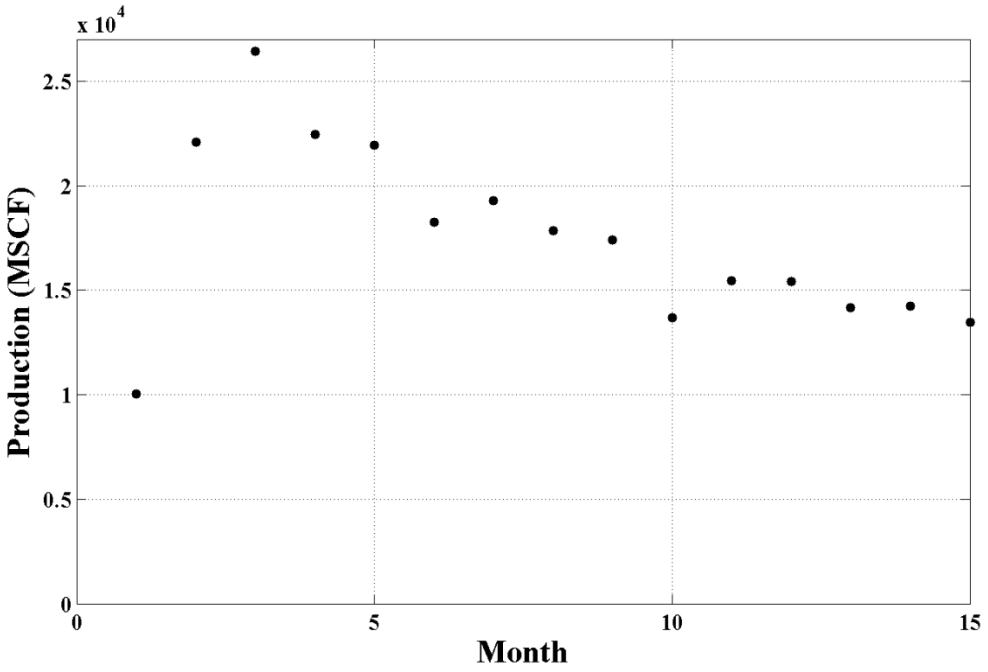

Figure D.5: Production data for well 42-439-30330.

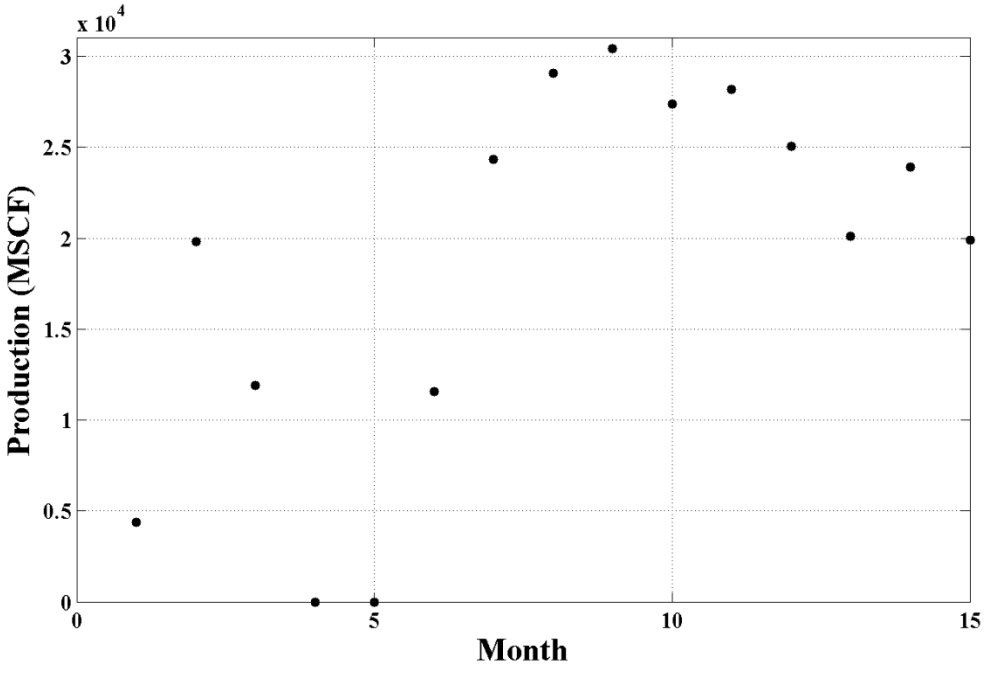

Figure D.6: Production data for well 42-439-30331.

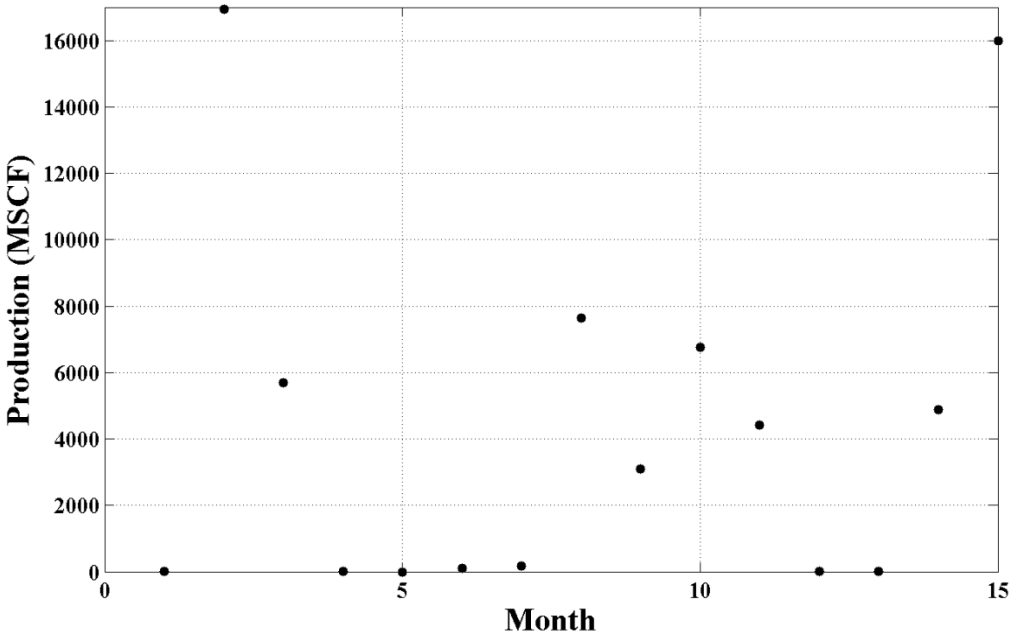

Figure D.7: Production data for well 42-439-30332.

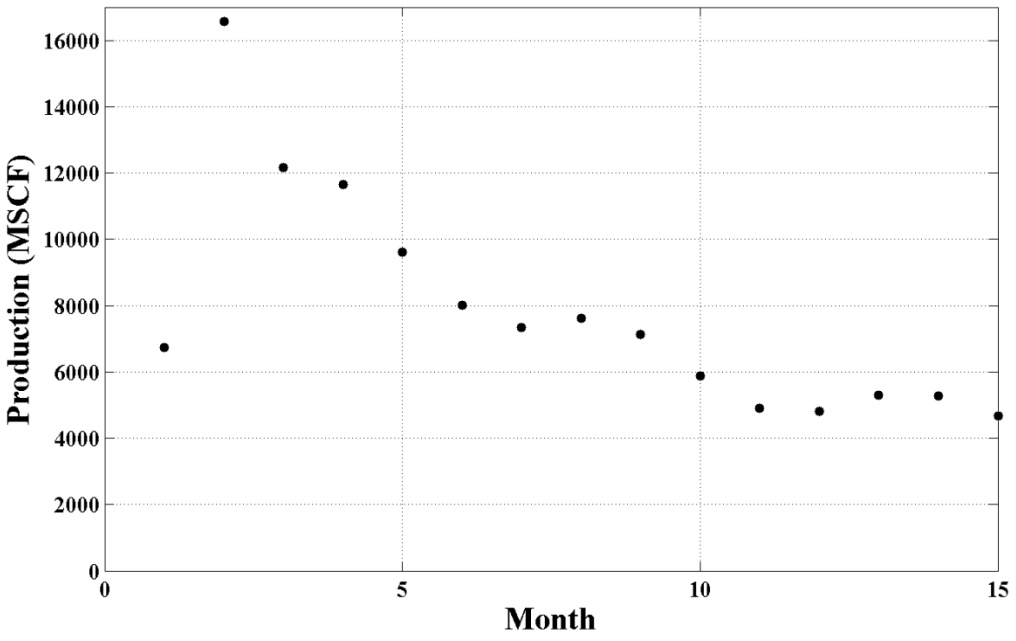

Figure D.8: Production data for well 42-121-31710.

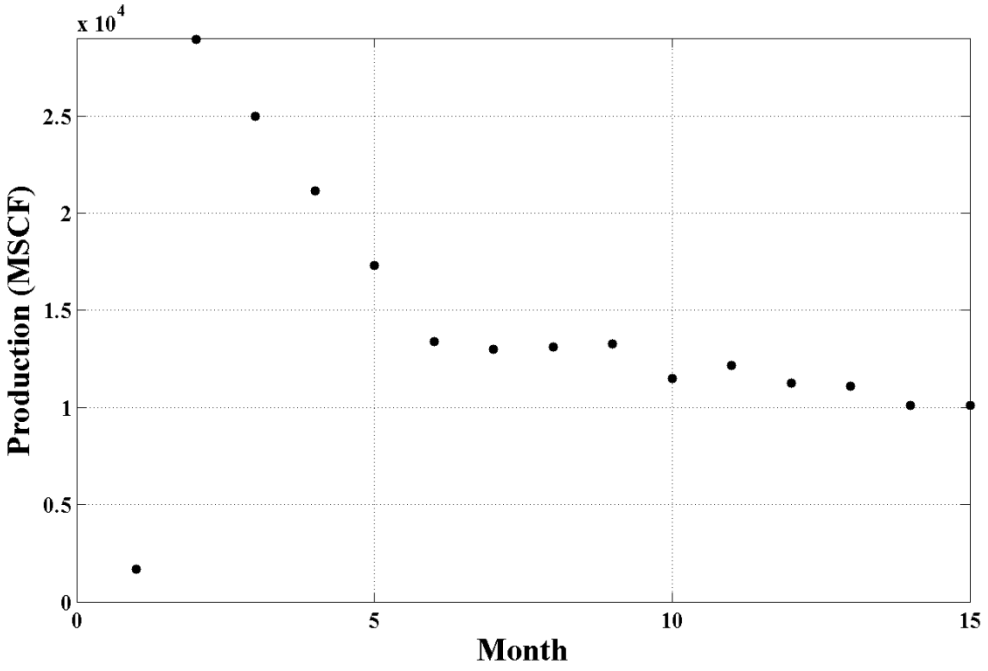

Figure D.9: Production data for well 42-121-30866.

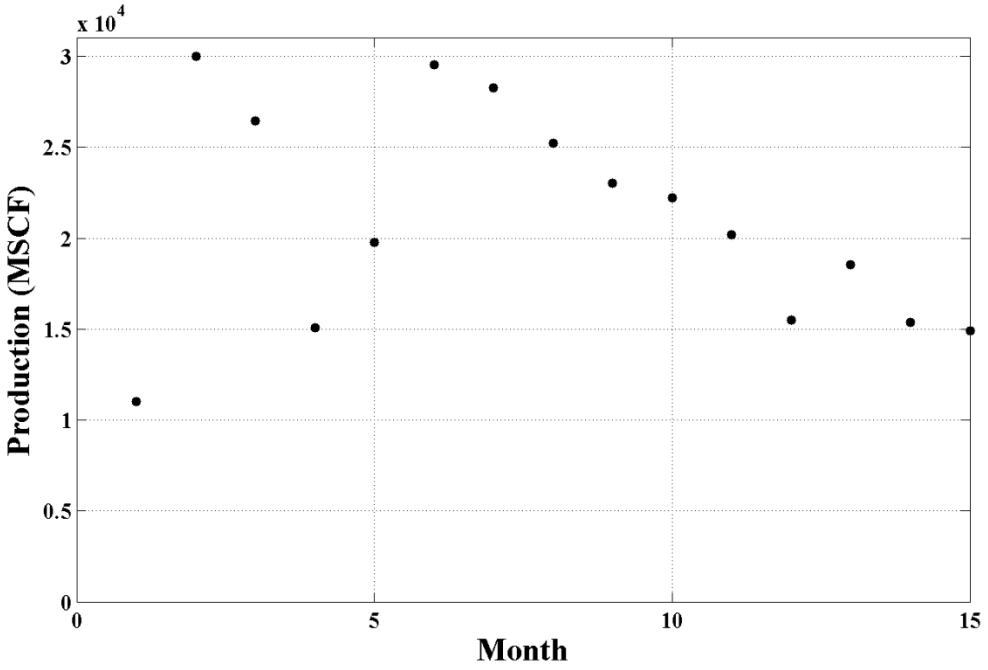

Figure D.10: Production data for well 42-439-30197.

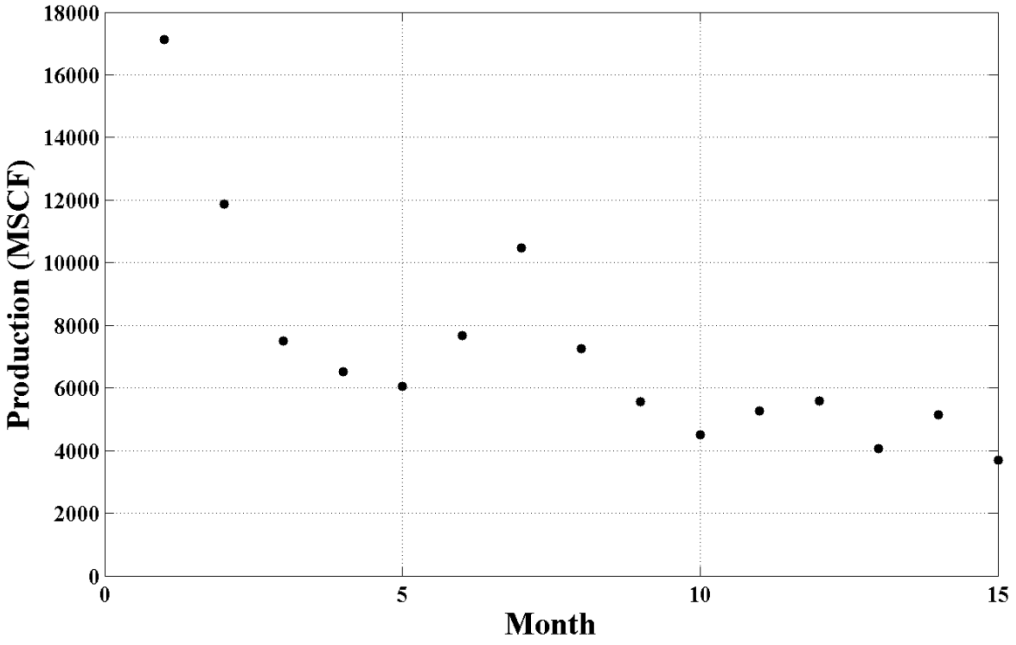

Figure D.11: Production data for well 42-121-31135.

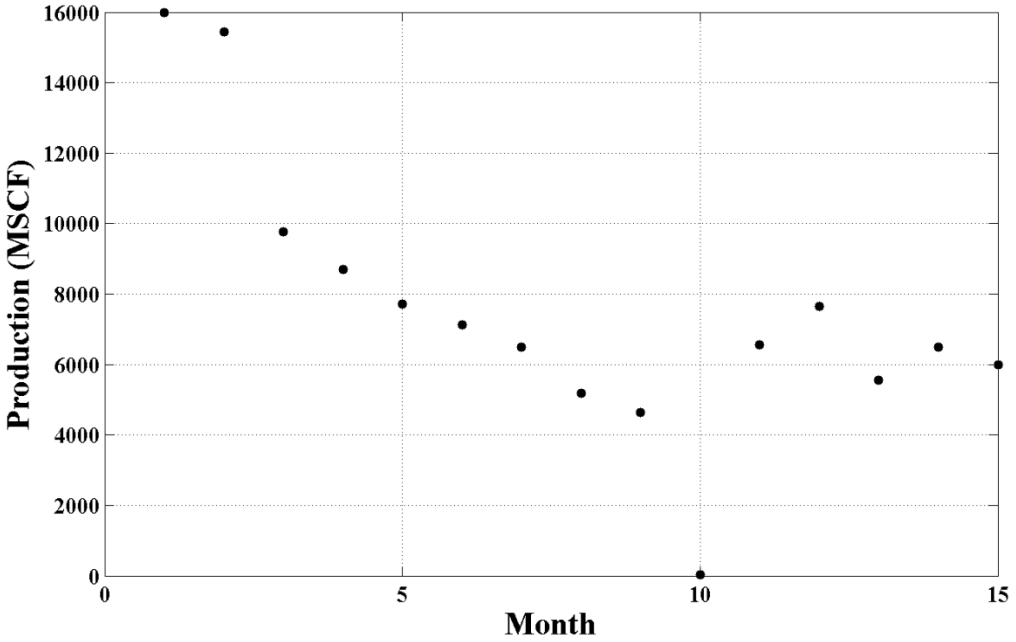

Figure D.12: Production data for well 42-121-31134.

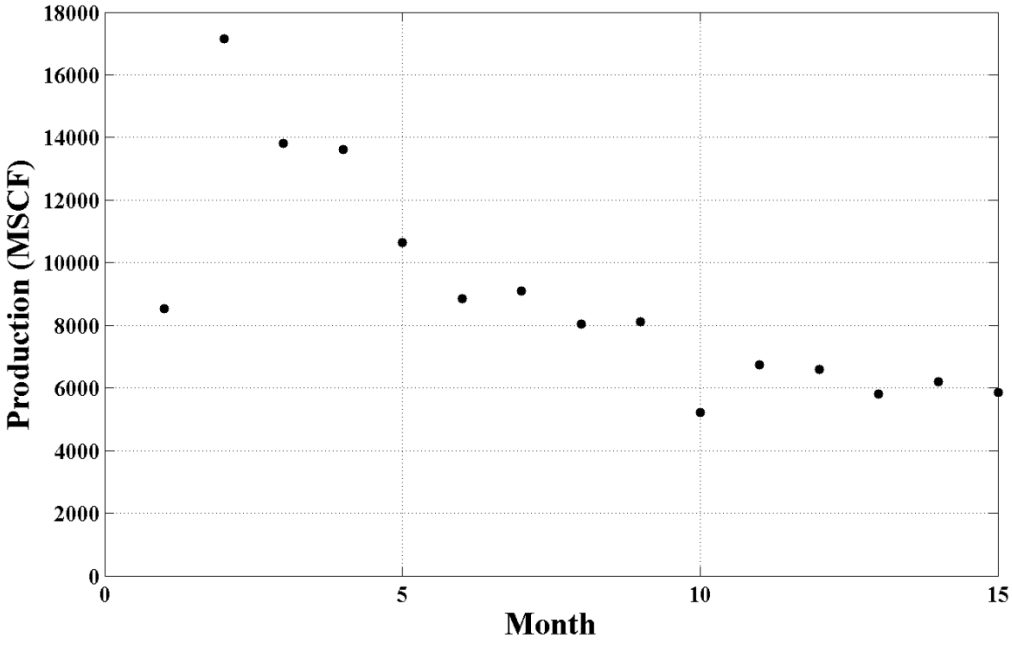

Figure D.13: Production data for well 42-497-34975.

Appendix E: Well logs used for the 15 wells in the analysis

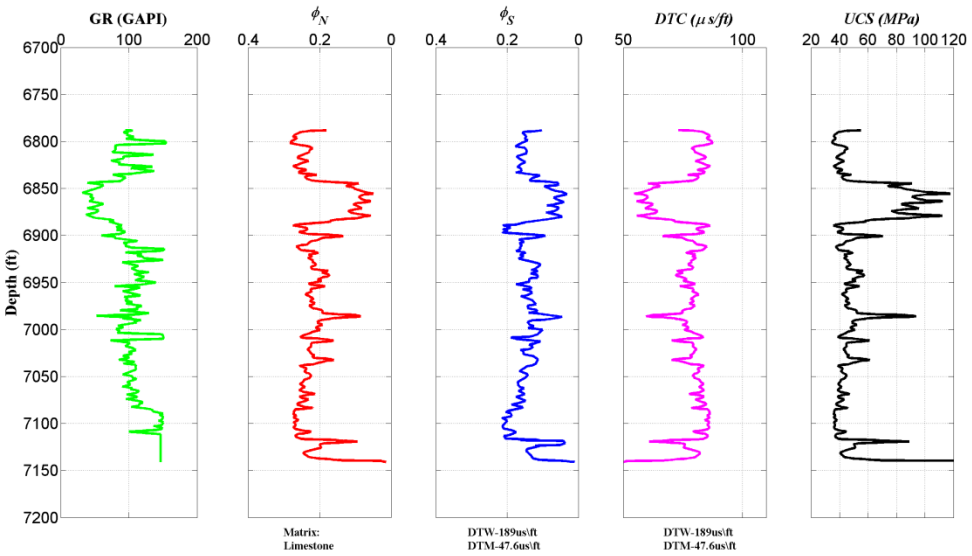

Figure E.1: Well logs for the well 42-439-30197.

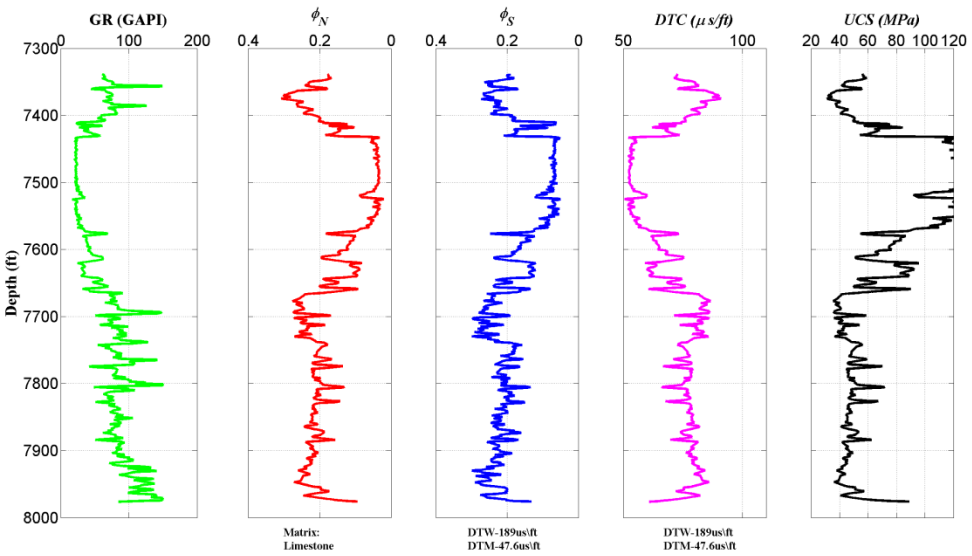

Figure E.2: Well logs for the well 42-497-34814.

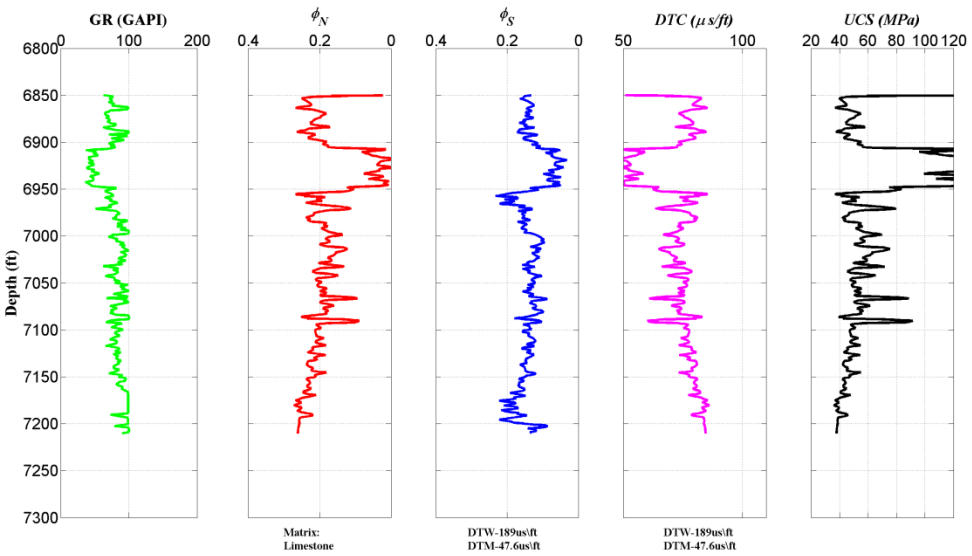

Figure E.3: Well logs for the well 42-497-34676.

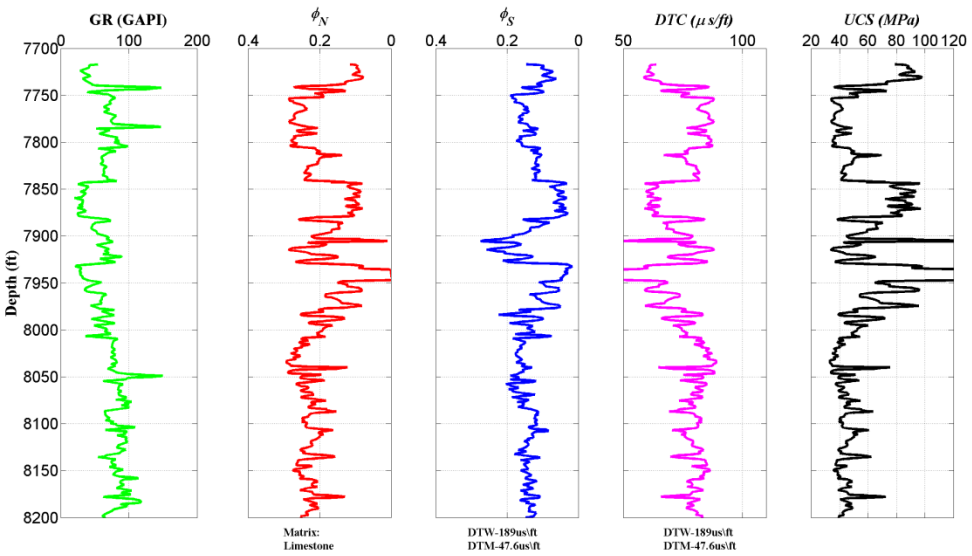

Figure E.4: Well logs for the well 42-121-32178.

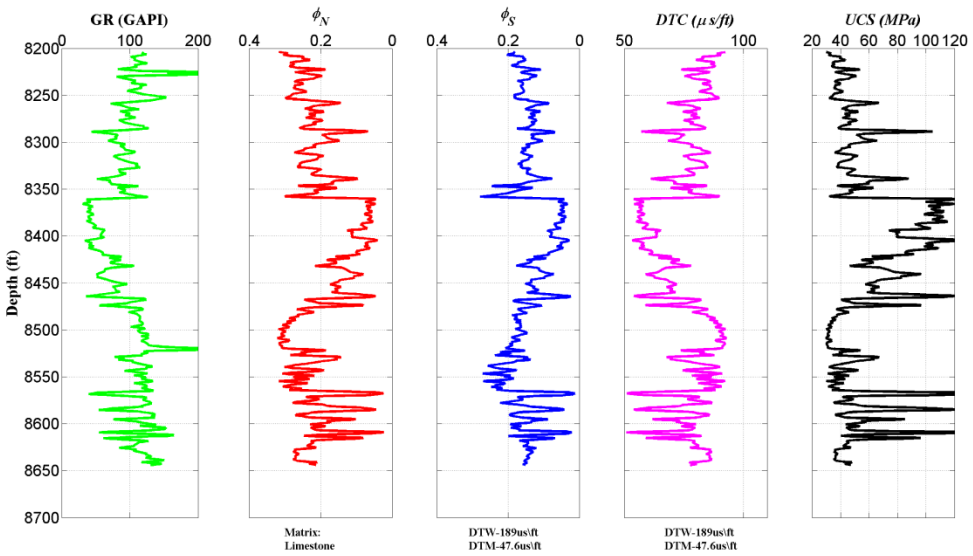

Figure E.5: Well logs for the well 42-121-31710.

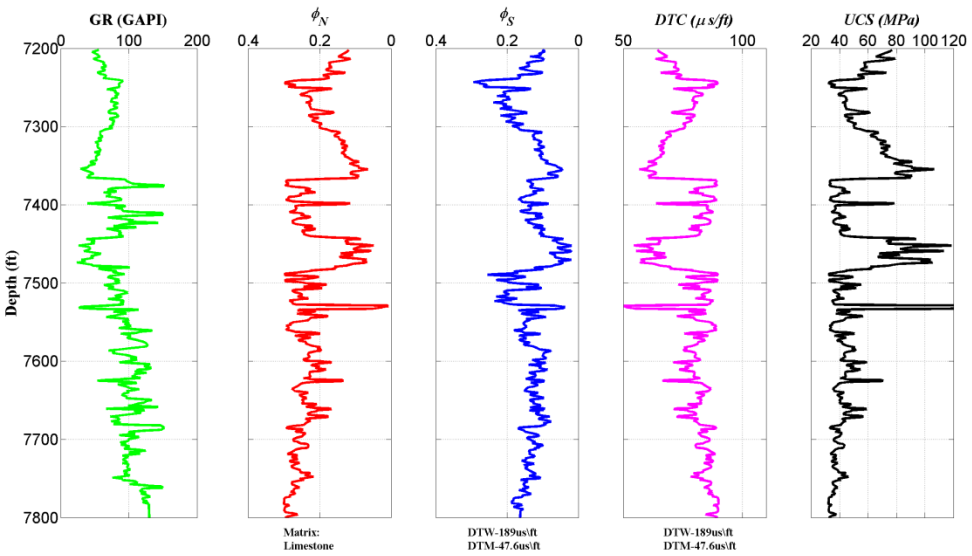

Figure E.6: Well logs for the well 42-439-31136.

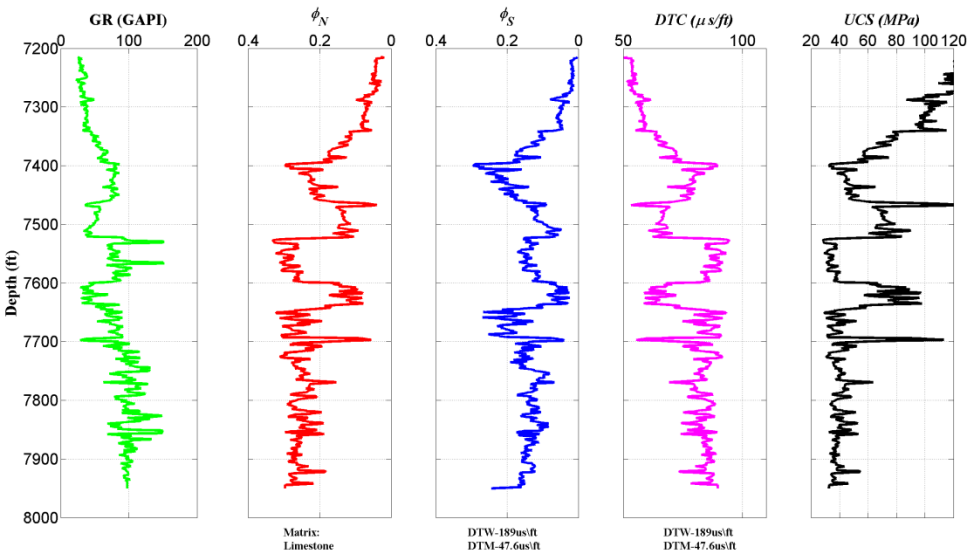

Figure E.7: Well logs for the well 42-439-31135.

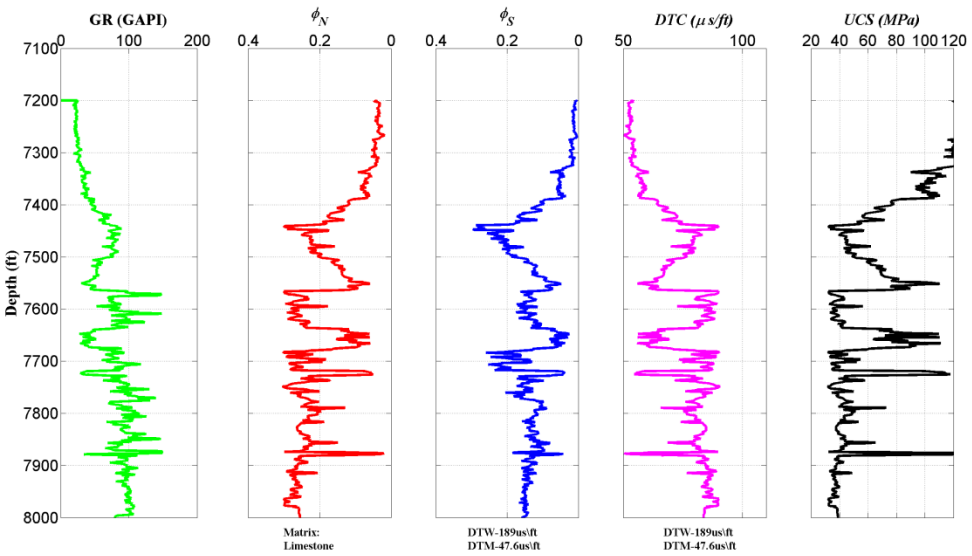

Figure E.8: Well logs for the well 42-121-31134.

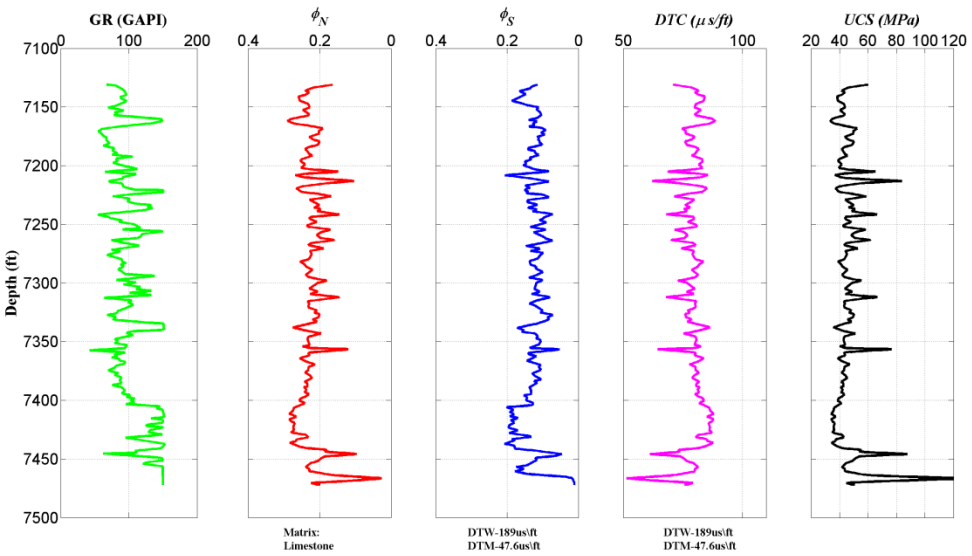

Figure E.9: Well logs for the well 42-439-30332.

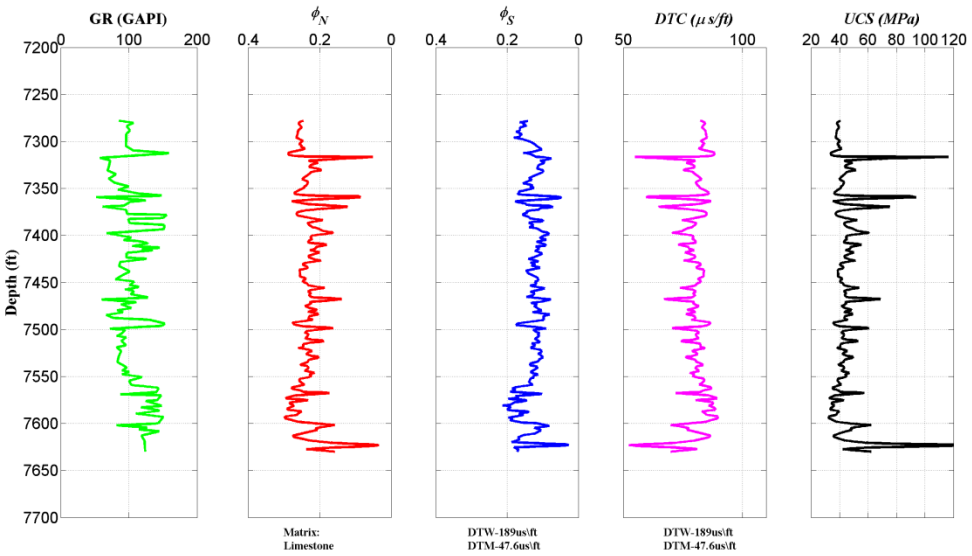

Figure E.10: Well logs for the well 42-439-30331.

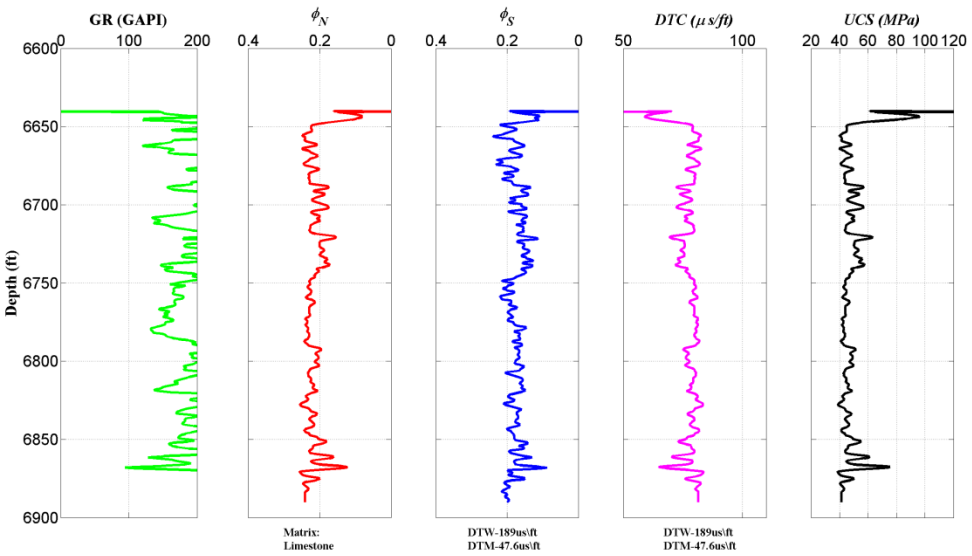

Figure E.11: Well logs for the well 42-439-30270.

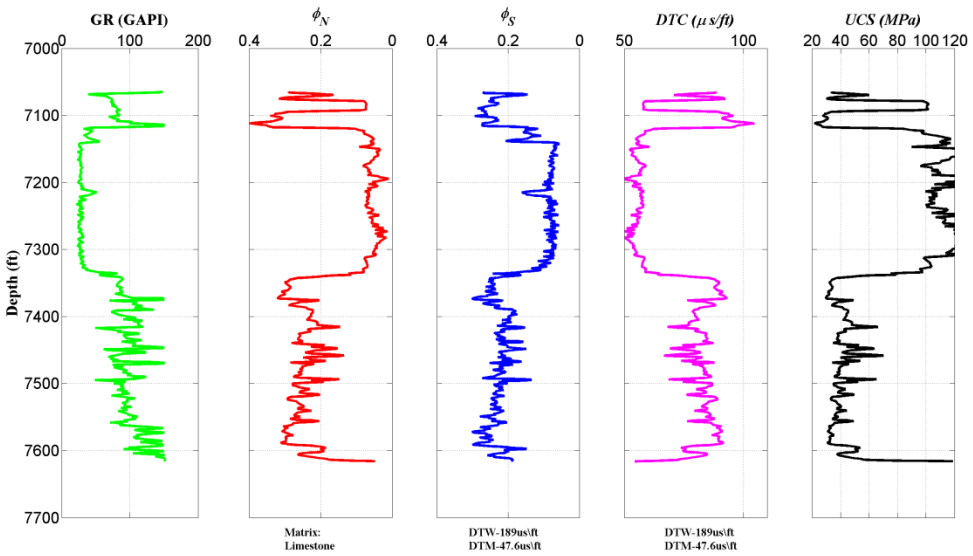

Figure E.12: Well logs for the well 42-497-34975

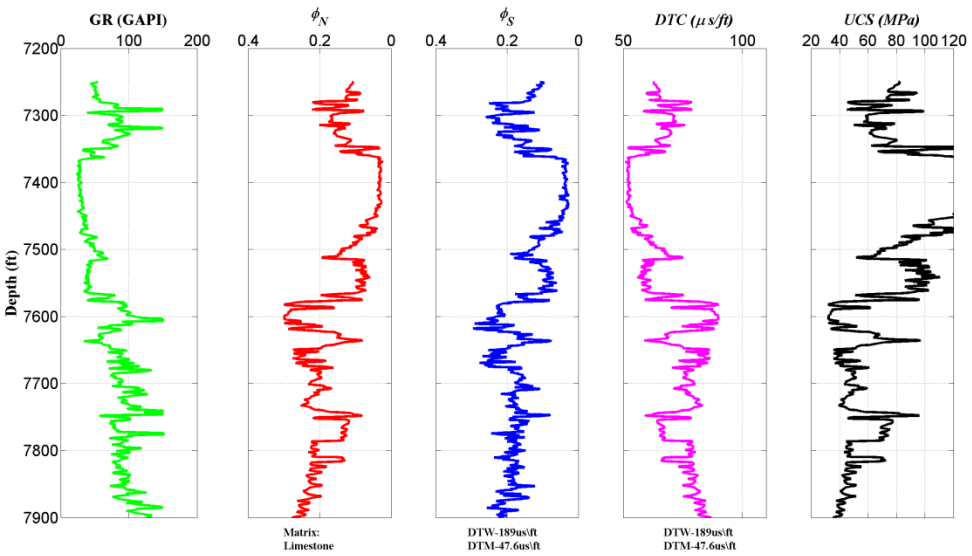

Figure E.13: Well logs for the well 42-497-35369.

Nomenclature

$D^0_{n,}$ $\phi_{E,dil}$, $\phi_{e,dil}$: Aperture dilation angle, unitless

dt: Duration of a time step, s

e: Hydraulic aperture, mm

E: Void aperture, mm

e_0: Reference hydraulic aperture, mm

E_0: Reference void aperture, mm

G: Shear modulus, GPa

h: Out of plane fracture width, or height, m

k: Permeability, m^2

K_I: Stress intensity factor, MPa-$m^{1/2}$

K_{IC}: Critical stress intensity factor for propagation of opening on a preexisting fracture, MPa-$m^{1/2}$

P: Pressure, MPa

q_f: Mass flux, kg/(s-m2)

S_0: Cohesion, MPa

s_a: Mass source term per area, kg/(s-m^2)

T: Transmissivity, m^3

$T_{hf,res}$: Residual permeability of the newly formed fractures, m^2

Ts: Stress tensor, MPa

v_p : Compressional velocity, km/s

ΔE_s: Increase in aperture due to shear, mm

Δt_c: Sonic travel time, μ s/ft

Δt_f: Fluid travel time, μ s/ft

Δt_m: Matrix travel time, μ s/ft

η: Radiation damping coefficient, MPa/(m/s)

η_{targ}: Time stepping tolerance, MPa

μ: Coefficient of friction, dimensionless

μ_l: Fluid viscosity, Pa-s

v: Poisson's ratio, dimensionless

ρ_l: Density, kg/m^3

σ_{Eref} σ_{eref}: Stress that causes 90% decrease in the fracture aperture, MPa

σ'_n: Effective normal stress, MPa

σ_n: Normal stress, MPa

σ_{xx}: Remote compressive stress in the x direction, MPa

σ_{xy}: Remote shear stress, MPa

σ_{yy}: Remote compressive stress in the y direction, MPa

τ: Shear stress, MPa

ϕ_N: Neutron Porosity

ϕ_S: Sonic Porosity

$\boldsymbol{\varepsilon}$: Strain tensor, unitless

Acronyms

JRC: Joint roughness coefficient

JCS: Joint compressive strength

UCS: Unconfined compressive strength

GAPI: American Petroleum Institute Gamma-ray Units

GR : Natural Gamma-Ray Log

sphi: Sonic porosity units

Nphi: Neutron Porosity units

DTW: Slowness for water

DTM: slowness for matrix

References

Aguilar, M., and Verma, S. (2014, October 29). TOC and Fracture Characterization of the Barnett Shale with Predicted Gamma Ray and Density Porosity Volumes. Society of Exploration Geophysicists.

Alahamadi, H. A. (2010). *A Triple Porosity Model for Fractured Horizontal Wells*. Master's Thesis. Texas A and M University, College Station, Texas, USA.

Anderson, T. W., (1962). On the distribution of the two-sample Cramer-von Mises criterion. *Annals of Mathematical Statistics* 33 (3): 1148-1159.

Barton, N. (1976). The shear strength of rock and rock joints. *Int. J. Rock Mech. Min. Sci. and Geomech.*, 13, 255-279.

Barton, N., and Choubey, V. (1977). The shear strength of rock joints in theory and practice. *Rock mechanics,* 10(1/2), 1-54.

Chang, C., Zoback, M. D, and Khaksar, A. (2006). Empirical relations between rock strength and physical properties in sedimentary rocks, *Journal of Petroleum Science and Engineering*, 51, 223–237.

Chester, F.M., and Logan, J.M., (1986). Implications for mechanical properties of brittle faults from observations of the Punchbowl fault zone, California. *Pure and Applied Geophysics*, 124 (1/2), 79-106.

Cipolla, C. L., Mack, M. G., Maxwell, S. C., and Downie, R. C. (2011, January 1). A Practical Guide to Interpreting Microseismic Measurements. Society of Petroleum Engineers. doi:10.2118/144067-MS

Cipolla, C. L., Warpinski, N. R., and Mayerhofer, M. J. (2008, January 1). Hydraulic Fracture Complexity: Diagnosis, Remediation, and Exploitation. Society of Petroleum Engineers. doi:10.2118/115771-MS

Cipolla, C. L., Weng, X., Mack, M. G., Ganguly, U., Gu, H., Kresse, O., and Cohen, C. E. (2011, January 1). Integrating Microseismic Mapping and Complex Fracture Modeling to Characterize Hydraulic Fracture Complexity. Society of Petroleum Engineers. doi:10.2118/140185-MS

Cipolla, C., and Wallace, J. (2014, February 4). Stimulated Reservoir Volume: A Misapplied Concept? Society of Petroleum Engineers. doi:10.2118/168596-MS

Co, C. R., and Horne, R. (2014, 24-26 February). Stress-Permeability Relationships in Low Permeability Systems: Application to Shear Fractures. Thirty-Ninth Workshop on Geothermal Reservoir Engineering, Stanford University, Stanford, California.

Dake, L. P. (1998). *Fundamentals of Reservoir Engineering*. 17th ed., Elsevier Science B.V.

Dupriest, F. E., and Koederitz, W. L. (2005, January 1). Maximizing Drill Rates with Real-Time Surveillance of Mechanical Specific Energy. Society of Petroleum Engineers. doi:10.2118/92194-MS

EIA/ARI. (2014). *World Shale Gas and Shale Oil Resource Assessment: Technically Recoverable Shale Gas and Shale Oil Resources: An Assessment of 137 Shale Formations in 41 Countries Outside the United State.* Arlington, USA.

Ellis, D. V., and Singer J.M. *Well Logging for Earth Scientists*. 2nd ed., Springer.

Esaki, T., Du, S., Mitani, Y., Ikusada, K. and Jing, L. (1999, May 12) Development of a Shear-Flow Test Apparatus and Determination of Coupled Properties for a Single Rock Joint. *International Journal of Rock Mechanics & Mining Science*, 36, 641-650.

Fredd, C. N., McConnell, S. B., Boney, C. L., and England, K. W. (2001, September 1). Experimental Study of Fracture Conductivity for Water-Fracturing and Conventional Fracturing Applications. Society of Petroleum Engineers. doi:10.2118/74138-PA

Gale, J. F. W., Reed, R. M., and Holder, J. (2007). Natural Fractures in the Barnett Shale and Their Importance for Hydraulic Fracture Treatments. *AAPG Bulletin*, 91(4), 603-622.

Giles, M. R., and Tennant, S. H. (2014, February 25). Sweet Spots: What Are They, Where Are They, How Are They Created and Are They Important Anyway? Society of Petroleum Engineers. doi:10.2118/167760-MS

Gu, H., Weng, X., Lund, J. B., Mack, M. G., Ganguly, U., and Suarez-Rivera, R. (2011, January 1). Hydraulic Fracture Crossing Natural Fracture at Non-Orthogonal Angles, A Criterion, Its Validation and Applications. Society of Petroleum Engineers. doi:10.2118/139984-MS

Hashmy, K. H., David, T., Abueita, S., and Jonkers, J. (2012, January 1). Shale Reservoirs: Improved Production From Stimulation Of Sweet Spots. Society of Petroleum Engineers. doi:10.2118/158881-MS

Hill, R. J., Jarvie, D. M., Zumberge, J., Henry, M., and Pollastro, R. M. (2007). Oil and gas Geochemistry and Petroleum Systems of the Fort Worth Basin. *AAPG Bulletin*, 91(4), 445-473.

Horsrud, P. (2001, June 1). Estimating Mechanical Properties of Shale From Empirical Correlations. Society of Petroleum Engineers. doi:10.2118/56017-PA

Hucka, V., and Das, B. Brittleness Determination of Rocks by Different Methods. *International Journal of Rock Mechanics and Mining Sciences*, 11, 389–392,

Ishibashi, T., Watanabe, N., Hirano, N., Okamoto, A., and Tsuchiya N. (2012). A novel model simulator for prediction of the 3-D channeling flow in a rock fracture network. *Water Resources Research*, 48(7).

Jaeger, J.C., Cook, N.G.W., and Zimmerman, R.W. (2007). *Fundamentals of Rock Mechanics*. 4th ed., Blackwell Pub.

Jarvie, D. M, Hill, R. J., Ruble, T. E., and Pollastro R. M. Unconventional Shale-Gas Systems: The Mississippian Barnett Shale of North-Central Texas as one Model for Thermogenic Shale-Gas Assessment. *AAPG Bulletin*, 91(4), 551-578.

Jarvie, D. M., Hill, R. J., Ruble, T. E., and Pollastro, R. M. (2007). Unconventional Shale Gas Systems: The Mississippian Barnett Shale of North-Central Texas as One Model for Thermogenic Shale-Gas Assessment, *AAPG Bulletin*, 91(4), 475–499.

Jin, X., Shah, S. N., Truax, J. A., and Roegiers, J. C. (2014, October 27). A Practical Petrophysical Approach for Brittleness Prediction from Porosity and Sonic Logging in Shale Reservoirs. Society of Petroleum Engineers. doi:10.2118/170972-MS

Kale, S. V., Rai, C. S., and Sondergeld, C. H. (2010, January 1). Petrophysical Characterization of Barnett Shale. Society of Petroleum Engineers. doi:10.2118/131770-MS

Kim, J., Tchelepi, H. A., and Juanes, R. (2011, June 1). Stability, Accuracy, and Efficiency of Sequential Methods for Coupled Flow and Geomechanics. Society of Petroleum Engineers. doi:10.2118/119084-PA

King, G. E. (2010, January 1). Thirty Years of Gas Shale Fracturing: What Have We Learned? Society of Petroleum Engineers. doi:10.2118/133456-MS

Kinley, T. J., Cook L. W., Breyer J. A., Jarvie D. M., and Busbey A. B. (2008).Hydrocarbon potential of the Barnett Shale (Mississippian), Delaware Basin, west Texas and southeastern New Mexico. *AAPG Bulletin*, 92(8), 967-991.

Klett, T. R. (2005). *Petroleum Systems and Geologic Assessment of Oil and Gas in the Southwestern Wyoming Province, Wyoming, Colorado, and Utah*. Retrieved from http://pubs.usgs.gov/dds/dds-069/dds-069-d/reports.html

Lawrence Berkeley National Laboratory. (2013). *Inventory of Shale Formations in the US, Including Geologic, Hydrological, and Mechanical Characteristics.* Lawrence Berkeley National Laboratory, Berkeley, California.

Liu, Y (2013). Workflows for sweet spots identification in shale plays using seismic inversion and well logs, *AAPG,* 90187.

Loucks, R. G., and Ruppel, S. C. (2007). Mississippian Barnett Shale: Lithofacies and Depositional Setting of a Deep-Water Shale-Gas Succession in the Fort Worth Basin, Texas. *AAPG Bulletin*, 91(4), 579-601.

Makurat, A., and Gutierrez, M. (1996, January 1). Fracture Flow and Fracture Cross Flow Experiments. Society of Petroleum Engineers. doi:10.2118/36732-MS

Mayerhofer, M. J., Lolon, E., Warpinski, N. R., Cipolla, C. L., Walser, D. W., and Rightmire, C. M. (2008, January 1). What is Stimulated Rock Volume? Society of Petroleum Engineers. doi:10.2118/119890-MS

McClure, M. W. (2012). *Modeling and characterization of hydraulic stimulation and induced seismicity in geothermal and shale gas reservoirs*. PhD dissertation, Stanford University, Stanford, California.

McClure, M. W and Horne, R. N. (2013). *Discrete Fracture Network Modelling of Hydraulic Stimulation: Coupling Flow and Geomechanics.* Springer Briefs in Earth Sciences, Springer.

McGlade, C., Speirs, J., and Sorrell, S. (2013). Unconventional gas – A review of regional and global resource estimates. *Energy*, 55, 571-584.

Mitani, Y., Sharifzadeh, M., Esaki, T., & Urakawa, F. (2005, January 1). Development of Shear-flow Test Apparatus and Determination of Coupled Properties of Rock Joint. *International Society for Rock Mechanics.*

Nabaei, M., Shahbazi, K., Shadravan, A., and Amani, M. (2010, January 1). Uncertainty Analysis in Unconfined Rock Compressive Strength Prediction. Society of Petroleum Engineers. doi:10.2118/131719-MS

Nygaard, R., and Hareland, G. (2007, January 1). Application of Rock Strength in Drilling Evaluation. Society of Petroleum Engineers. doi:10.2118/106573-MS

Onyia, E. C. (1988, January 1). Relationships Between Formation Strength, Drilling Strength, and Electric Log Properties. Society of Petroleum Engineers. doi:10.2118/18166-MS

Passey, Q. R., Creaney, S., Kulla, J. B., Moretti, F. J., and Stroud J.D. (1990). A Practical Model for Organic Richness from Porosity and Resistivity Logs. *AAPG Bulletin*, 74(12), 1777-1794.

Pendrel, J., Debeye, H., Pedersen-Tatalovic, R., Goodway, B., Dufour, J., Bogaards, M., and Stewart, R. (2000). Estimation and Interpretation of P and S Impedance Volumes from the Simultaneous Inversion of P-Wave Offset Data. *CSEG Ann. Mtg. Abs. paper* AVO 2.5.

Pilcher, R. S., McDonough Ciosek, J., McArthur, K., Hohman, J. C., and Schmitz, P. (2011, January 1). Ranking Production Potential Based on Key Geological Drivers - Bakken Case Study. International Petroleum Technology Conference. doi:10.2523/IPTC-14733-MS

Pollastro R. M. (2007). Total Petroleum System Assessment of undiscovered Resources in the giant Barnett Shale Continuous (Unconventional) Gas Accumulation, Fort Worth Basin, Texas. *AAPG Bulletin*, Vol 91(4), 551-578.

Pollastro R. M., Jarvie D. M., Hill, R. J., and Adams, C. W. (2007). Geologic Framework of the Mississippian Barnett Shale, Barnett-Paleozoic Total Petroleum System, Bend arch–Fort Worth Basin, Texas. *AAPG Bulletin*, Vol 91(4), 405-436.

Rickman, R., Mullen, M. J., Petre, J. E., Grieser, W. V., and Kundert, D. (2008, January 1). A Practical Use of Shale Petrophysics for Stimulation Design Optimization: All Shale Plays Are Not Clones of the Barnett Shale. Society of Petroleum Engineers. doi:10.2118/115258-MS

Romana, M. (1999, January 1). Correlation Between Uniaxial Compressive And Point-load (Franklin Test) Strengths For Different Rock Classes. *International Society for Rock Mechanics*.

Saltelli, A., Ratto, M., Andres, T., Campolongo, F., Cariboni, J., Gatelli, D., Saisana, M., and Tarantola, S. *Global Sensitivity Analysis: The Primer*. Wiley Pub, West Sussex, England, 2008

Sayers, C. M., Russell, C. L., Pelorosso, M., Adachi, J., Pastor, J. A. A., Singh, V., Hooyman, P. J. (2009, January 1). Determination of Rock Strength Using Advanced Sonic Log Interpretation Techniques. Society of Petroleum Engineers. doi:10.2118/124161-MS

Sieminski, A. (2014, March 27). Outlook for U.S. Shale Oil and Gas. Washington DC, International Monetary Fund.

Smirnov, N., (1948). Table for estimating the goodness-of-fit of empirical distributions. *Annals of Mathematical Statistics* 19 (2): 279-281, doi: 10.1214/aoms/1177730256.

Sobol, I. M. (1967). On the distribution of points in a cube and the approximate evaluation of integral. *USSR Comp. Math, Phys.,* 7, 86–112.

Stephens, M. A., (1974). EDF statistics for goodness-of-fit and some comparisons. *Journal of the American Statistical Association* 69 (347): 730-737.

Tokle, K., Horsrud, P., and Bratli, R. K. (1986, January 1). Predicting Uniaxial Compressive Strength from Log Parameters. Society of Petroleum Engineers. doi:10.2118/15645-MS

Unal, M., and Unver, B. (2004). Characterization of Rock Joint Surface Degradation under Shear Loads. *International Journal of Rock Mechanics and Mining Sciences*, 41(3), 145–150.

Warpinski, N. R., Lorenz, J. C., Branagan, P. T., Myal, F. R., and Gall, B. L. (1993, August 1). Examination of a Cored Hydraulic Fracture in a Deep Gas Well (includes associated papers 26302 and 26946). Society of Petroleum Engineers. doi:10.2118/22876-PA

Warpinski, N.R, and Teufel L.W. (1987). Influence of Geologic Discontinuities on Hydraulic Fracture Propagation. *Journal of Petroleum Technology,* 39(2), 209-220.

Willis-Richard, J., Watanabe, N., and Takahash, H. (1996). Progress toward a stochastic rock mechanics model of engineered geothermal systems. *J. of Geophysical Research*, 101(B8), 17481-17496.

Yang, Y., Sone, H., Hows, A., and Zoback, M. D. (2013, January 1). Comparison of Brittleness Indices in Organic-rich Shale Formations. American Rock Mechanics Association.

Zhang, J., Kamenov, A., Zhu, D., and Hill, D. (2013, March 26). Laboratory Measurement of Hydraulic Fracture Conductivities in the Barnett Shale. International Petroleum Technology Conference. doi:10.2523/16444-MS

Zhao, H., Givens N. B., and Curtis, B. (2006). Thermal maturity of the Barnett Shale determined from well-log analysis. *AAPG Bulletin*, 91(3), 535-549.

Zoback, M. D., Barton, C. A., Brudy, M., Castillo, D. A., Finkbeiner, T., Grollimund, B. R., Moos, D. B., Peska, P., Ward, C. D., and Wiprut, D. J., (2003, December). Determination of stress orientation and magnitude in deep wells. *International Journal of Rock Mechanics and Mining Sciences,* 40(7/8).